Express Polymer Letters Vol.17, No.10 (2023) 991
Available online at www.expresspolymlett.com
https://doi.org/10.3144/expresspolymlett.2023.73

Editorial corner – a personal view

Development challenge for synthetic polymer fibers and tapes: improving toughness

László József Varga[1], *Tamás Bárány*[1,2*]

[1]Department of Polymer Engineering, Faculty of Mechanical Engineering, Budapest University of Technology and Economics, Műegyetem rkp. 3., H-1111 Budapest, Hungary
[2]MTA-BME Lendület Lightweight Polymer Composites Research Group, Műegyetem rkp. 3., H-1111 Budapest, Hungary

Polymer fibers are essential in the textile industry, as they can provide various properties such as strength, durability, elasticity, and resistance to heat, chemicals and abrasion. Synthetic polymer fibers can also be a sustainable way to produce clothes in large numbers, as they do not require a large land area and resources to breed the animals and to grow the plants that natural fibers are originally acquired from. Synthetic polymer fibers and tapes are also used in various industrial segments, such as aerospace, automotive, construction, medical, and packaging, including the strongest possible fibers and tapes, such as aramid and ultra-high molecular weight polyethylene (UHMWPE) fibers, and industrial fibers, such as nylon, polyester, polypropylene, and polyethylene fibers, which can offer good mechanical properties, low cost, and are easy to process.

Molecular orientation is one of the vital factors of the excellent performance of polymer fibers and tapes. Molecular orientation is usually achieved in the liquid state (polymer melt or solution), or by solid-state drawing, which involves stretching the polymer melt or solid polymer at a specific temperature and speed or by their combined application. Molecular orientation drastically increases the tensile strength and modulus of the polymer fibers and tapes.

However, molecular orientation reduces the strain at break of the polymer fibers and tapes, making them less tough and prone to fracture. Therefore, one of the most important challenges in developing these products is to increase their toughness and resistance to crack propagation while retaining their tensile strength and modulus.

One way to improve the toughness of polymer fibers and tapes is to use additives that can modify the structure or interactions of the polymer chains. For example, nano-size additives, such as carbon nanotubes (https://doi.org/10.3390/polym14020260) or montmorillonite (https://doi.org/10.1080/20550324.2019.1671038), can be incorporated into the polymer matrix to enhance its mechanical properties.

Blending is also a possible way to improve the toughness of the tapes. Some polymers can facilitate the movement of the molecules of the tape during the drawing process and, in some cases, even afterward; thus, blending can improve the toughness of the drawn tapes. In the case of polypropylene (PP) tapes, amorphous poly-alpha-olefins (APAOs) had this effect on drawn, highly oriented tapes (https://doi.org/10.1021/acsomega.3c01772).

The sustainability of production can be increased by using biodegradable polymers, which can degrade under certain industrial conditions. For example, poly(lactic acid) (PLA) is a polyester that can be derived from renewable sources such as corn starch or sugar cane (https://doi.org/10.3390/fib3040523) and can be composted. The molecular orientation of PLA is a heavily researched area, but PLA still has some limitations, such as low thermal stability and poor hydrolytic resistance. Therefore, optimizing PLA for industrial applications requires a lot of research.

The production of polymer fibers and tapes has a long history, but with new materials and additives, there is still room for improvement. Polymer fibers and tapes will continue to play a vital role in various fields that require high performance and sustainability.

*Corresponding author, e-mail: barany@pt.bme.hu
© BME-PT

Express Polymer Letters Vol.17, No.10 (2023) 992–1006
Available online at www.expresspolymlett.com
https://doi.org/10.3144/expresspolymlett.2023.74

Research article

Sustainable polymers and sisal fibers based green composites: A detailed characterization and analysis

Karri Santhosh Kumar[1], *Sandeep Gairola*[2], *Inderdeep Singh*[1,2*]

[1]Mechanical and Industrial Engineering Department, Indian Institute of Technology Roorkee, Uttarakhand, India
[2]Centre of Excellence in Disaster Mitigation and Management, Indian Institute of Technology Roorkee, Uttarakhand, India

Received 11 April 2023; accepted in revised form 22 June 2023

Abstract. In the global pursuit of using sustainable constituents for developing composite materials, the current investigation has paid particular attention to the most promising biopolymers, such as poly(lactic acid) (PLA) and bio-based poly(butylene succinate) (bio PBS). The research endeavor emphasizes a comparative assessment of short sisal fiber (SF) reinforced (10, 20, and 30 wt%) PLA and bio PBS biocomposites. The analysis and discussion have been reported for the thermal, mechanical, crystallinity, and dynamic mechanical behavior of developed composite materials. Based on mechanical properties, the optimal fiber loading for SF/PLA and SF/bio PBS biocomposites was 20 and 30 wt%, respectively. The developed composites have shown a considerable improvement in crystallinity of 17.88 and 41.13% at 20 and 30 wt% of fiber loading in SF/PLA and SF/bio PBS, respectively. The maximum storage modulus values of 14.23 GPa (20SF/PLA) and 11.74 GPa (30SF/bio PBS) were observed. The loss modulus of the SF/PLA and SF/bio PBS composites was around 74 and 89% higher than the loss modulus of the PLA and the bio PBS matrix, respectively. Overall, composites fabricated with bio PBS (SF/bio PBS) have shown better crystallinity, thermal stability, and ease of processing than SF/PLA composites.

Keywords: *biodegradable polymers, biocomposites, mechanical properties, thermal properties, degree of crystallinity*

1. Introduction

Polymers derived from renewable sources have recently drawn a lot of attention in replacing the traditional petrochemical-derived and non-degradable polymers due to problematic plastic pollution and the rising oil price [1]. Among the most promising biodegradable polymers is bio-based polybutylene succinate (bio PBS), which has high ductility and melt processing capabilities, making it appropriate for various industries, including flexible packaging, agriculture, and consumer goods. PBS is a polyester made of poly-condensing succinic acid and 1,4-butanediol. Until recently, both PBS monomers were typically produced by several processes that began with petrochemical compounds. These monomers can also be made by fermenting agricultural or industrial wastes or other renewable resources (bio-based) [2–4]; the Biomass content of PBS accounts for 80% of its total composition [5]. Similarly, lactic acid is converted into PLA through ring-opening or grafting polymerization in plants that contain starch, such as corn and cassava. It is also a thermoplastic polymer with superior strength and transparency [6]. However, drawbacks such as brittleness limit its processability, making it unsuitable for use in the packaging industries, especially where high ductility is required [7, 8].

The predominant disadvantages of biopolymers are high cost and limited performance. The high price is due to the low production volume of biopolymers and the lack of knowledge. Therefore, biopolymers are often reinforced with natural fibers to develop novel composite materials. Combining natural fibers addresses the properties and cost of the composites [9,

*Corresponding author, e-mail: inderdeep.singh@me.iitr.ac.in
© BME-PT

10]. The sisal fibers produced from the leaves of sisal plants have been investigated in the current study as a natural, cost-effective filler within bio PBS and PLA at various weight percentages. Sisal fiber (SF) is one of the most widely used natural fibers. Nearly 4.5 million tons of SFs are produced every year throughout the world. A sisal plant yields 200–250 leaves, each carrying more than a thousand fiber bundles with a fiber content of 4% [11]. It has a rough surface due to its coarse grain structure, high strength, and high water absorption capacity [12, 13]. SFs were chosen due to their yearly large quantity availability, compatibility with biopolymers (due to their coarse grain structure), and affordability. Due to their superior mechanical performance and relative stability, PLA and bio PBS may eventually replace conventional thermoplastic polymers. Interestingly, the melting temperatures of these two biodegradable polymers (bio PBS and PLA) are below 200 °C, enabling the production of biocomposites without damaging sisal fibers [14].

Ngaowthong *et al*. [15] used a co-rotated twin screw extruder to develop composites made of sisal fiber, polypropylene, and PLA. The incorporation of sisal fiber enhanced the tensile modulus and percentage crystallinity of composites. Zhu *et al*. [16] studied the effect of the chemical composition of fibers on the tensile strength of SF and the interfacial strength between SFs and PLA. The results showed that the optimal ratio of fiber constituents (cellulose, hemicellulose, and lignin) was suitable for the tensile strength of SF and the interfacial strength between SF and PLA. Feng *et al*. [17] established a technique to assess the rheological characteristics of SF/PBS composites and, after mixing, estimated the aspect ratio of SFs. The results indicate that shear thinning is more pronounced with increasing SF content, because of disentanglement, breakage, and orientation of SFs. During the extrusion process, when fiber content increases, the number of fibers within the given volume increases, which leads to increased friction and shearing action between the fibers, resulting in decreased fiber length due to fiber breakage and subsequently leading to decreased aspect ratio. Bajpai *et al*. [18] developed composites with natural fibers with polypropylene and PLA matrices and assessed their mechanical and morphological characteristics. PLA/sisal fiber composites showed superior mechanical properties.

Yan *et al*. [19] reported crystallization and dynamic mechanical analysis (DMA) behavior of coir fiber/ PBS biocomposites with 20 and 40 wt% fiber content. X-ray diffraction (XRD) shows identical crystal forms of pure PBS and coir fiber/ PBS composites. Storage modulus significantly increased in coir fiber/ PBS composites. Li *et al*. [20] evaluated the mechanical characteristics and crystallinity of PBS/basalt fiber biocomposites. Composites were made with different fiber content using a twin screw extruder and injection molding. Adding basalt fiber enhanced the mechanical properties and thermal stability of composites. Due to the negligible nucleation impact of basalt fiber, the crystallization of PBS in composites does not alter. Samouh *et al*. [21] evaluated the mechanical and thermal properties and DMA behavior of PLA/sisal fiber biocomposites with various fiber weight fractions. The mechanical and DMA behavior of biocomposites improves with an increase in the reinforcing rate. Increased sisal fiber content improved the crystallinity in the matrix because the fibers serve as PLA nucleating agents.

In the last two decades, there has been noteworthy research in the field of natural fiber-reinforced biodegradable composites. However, most literature focused on individual biopolymer-based composites or biopolymer blends. A considerable volume of research has focused on PLA-based composites despite their disadvantages as compared to other biodegradable polymers. There has been limited research on other biodegradable polymers, such as PBS, poly(3-hydroxybutyrate-*co*-3-hydroxyvalerate) (PHBV), and poly(butylene adipate-*co*-terephthalate) (PBAT). The present research investigation aims to develop and conduct a comparative assessment of untreated short sisal fiber-reinforced (10, 20, and 30 wt%) PLA/ bio PBS matrix sustainable composites. The mechanical, thermal, crystallinity and morphological characteristics of developed composites have been investigated in detail and reported.

2. Materials and methodology

2.1. Materials

Raw sisal fibers were procured from the Women's Development Organisation, Dehradun, India. SFs were shredded into short fibers with an average 3–6 mm length. The PLA (grade 3052D) was purchased from Nature Tech. India Pvt. Ltd. in Chennai, India, in pellets form (density, $\rho = 1.24$ g/cm^3, melt flow

rate, *MFR* = 14 g/10 min (210 °C, 2.16 kg)). Bio PBS (grade: FZ71PB) was procured from Tanhim Enterprises Pvt. Ltd., Greater Noida, India, in the form of pellets (ρ =1.26 g/cm^3, *MFR* = 22 g/10 min (190 °C, 2.16 kg)).

2.2. Fiber characterization

Single fiber strength tests were performed using Instron 5982 following ASTM D3822-14 with a fixed gauge length of 30 mm and a crosshead speed of 0.5 mm/min. The SF strands were fastened on cardboard paper with the help of an adhesive. The fiber diameter was obtained by averaging five observations along the fiber length using a stereo microscope with the help of VUE 2014 software (with a magnification factor of 50). The surface of an untreated sisal fiber was analyzed using a Field Emission Scanning Electron Microscope (FESEM) (Make: ZEISS, Model: Gemini 1). The weight percentage of organic elements in SF was determined using the energy dispersive spectroscope (EDS). The thermogravimetric analyzer (TGA) (EXSTAR 6300) was used to examine the thermal stability and degradation behavior of fibers. The maximum test temperature and the heating rate were 700 °C and 10 °C/min, respectively, and analysis was conducted in a nitrogen atmosphere (200 ml/min).

2.3. Fabrication of composite specimens

Before using sisal fibers for blending, fibers were drenched in tap water for 24 hours to get rid of dirt and pith from the fiber surface and, thereafter, dried under sunlight for 48 hours to remove moisture from the fibers. The fibers were heated to 80 °C in an air-circulated oven for 6 hours. PLA and bio PBS were dried in an oven at 50 °C for 8 hours and blended with SF (10, 20, 30 wt%) using a single screw extruder (Make: Sai Extrumech Model: SAI-25) at a temperature of 165 and 135 °C, respectively, and extruder speed of 45 rpm. The blended composite strands were passed through the water bath and pelletized into an average length of 4–5 mm.

The fabrication process of biocomposites using extrusion-injection molding is depicted in Figure 1 and the nomenclature for the same is shown in Table 1.

Extruded pellets were used in the injection molding machine (Make: Electronica Model: ENDURA-60) to make final specimens in accordance with ASTM standards. The processing temperature values for heaters along the barrel (from hopper to nozzle) were optimized from pilot experiments. The temperatures of respective zones are 165–170–175–180 °C (PLA/SF composites) and 155–155–160–155 °C (Bio PBS/SF composites).

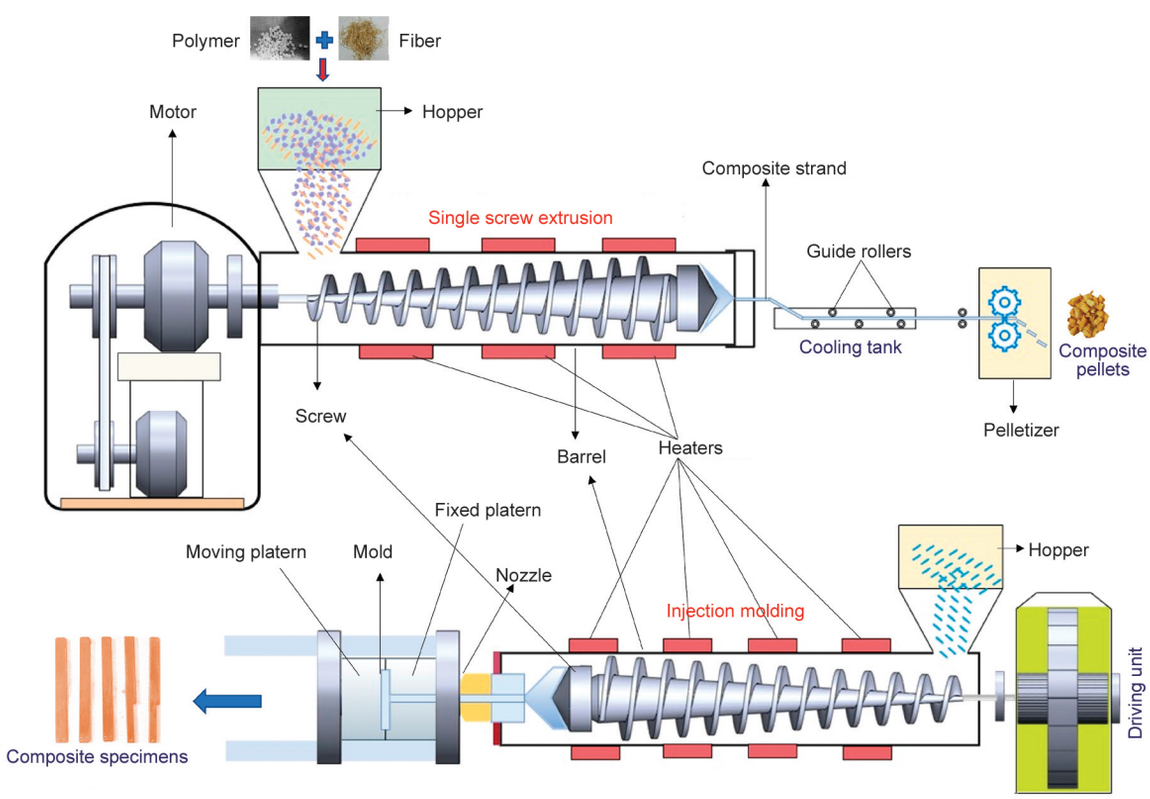

Figure 1. Schematic diagram showing processing of composite specimens.

Table 1. Nomenclature for specimens prepared by extrusion-injection molding.

Specimen name	Nomenclature
PLA	Poly(lactic acid)
Bio PBS	Bio based poly(butylene succinate)
SF	Sisal fiber
USF	Untreated sisal fiber
10SF	10 wt% sisal fiber loading
20SF	20 wt% sisal fiber loading
30SF	30 wt% sisal fiber loading
SF/PLA or SF_PLA	Sisal fiber-based PLA composite.
SF/bio PBS or SF_bio PBS	Sisal fiber-based bio PBS composite.
EIM	Extrusion-injection molding

2.4. Characterization of biocomposites

The optimum weight percentage of fibers in the developed biocomposites and mechanical behavior were evaluated and compared. The thermal and morphological properties and crystallinity of fabricated composites were assessed and compared. A universal testing machine (UTM) (Make: Instron, Type: 5982) with a 100 kN capacity was used to evaluate the tensile and flexural strength. According to the ASTM D3039M-14, tensile tests were carried out at a crosshead speed of 2 mm/min and a gauge length of 50 mm, respectively. According to ASTM D790-10, flexural tests were performed using a three-point bending fixture with a crosshead speed of 2 mm/min and 60 mm for the span length. The impact test employed a low-energy pendulum impact tester (Tinius Olsen-IT504) employing the ASTM D256-10 standard. The fractured surface of damaged samples after tensile testing was examined by SEM micrographs using the FESEM set-up. The thermal degradation characteristics of developed biodegradable polymer composites were measured by a thermogravimetric analyzer (Make: EXSTAR 6300). Under the nitrogen atmosphere, 10 mg samples were heated at 10 °C/min to 600 °C. The DMA (Make: NETZSCH, Model: DMA 242 C) was undertaken to understand the potential effects of SF loading on the visco-elastic response of composites and to examine the effectiveness of developed biocomposites under dynamic loading. In the three-point bending mode, samples with dimensions of 50×12×3 mm were tested as per ASTM D5023-15. DMA scans were performed at a ramping temperature of 2 °C/min, ranging from –45 to 90 °C, and a frequency of 1 Hz was used.

A thin film X-ray diffractometer (Make: Smart Lab Model: Rigaku) was used to analyze the amorphous and crystalline phases of fabricated samples. The sample's crystallinity was calculated using Equation (1) [22]:

$$\text{Crystallinity}\,[\%] = \frac{\text{Crystalline area}}{\text{Total area under the curve}} \cdot 100 \quad (1)$$

3. Results and discussion

3.1. Morphological examination of fibers

In scanning electron microscopy (SEM), an electron beam produces a magnified image of solid inorganic materials for microanalysis. Figure 2 portray the surface of SFs. Figure 2a shows the surface roughness of longitudinal SF, and Figure 2c reveals the presence of impurities and waxy cuticles [23, 24]. The parenchyma cells can be seen in Figure 2b [25].

3.2. Fiber strength test

The stress-strain behavior of untreated SF is shown in Figure 3. Stress-strain curves of fibers revealed minor extension after achieving peak strength value followed by brittle fracture. The extension after peak may be attributed to the load withstood by the intact fibrils that comprise the lignocellulosic fibers. The waviness in the curve may be attributed to surface roughness, waxy cuticles, and impurities on the surface of untreated SFs. Experimental outcomes established that the tensile behavior of fiber varied due to the variation in fiber diameter. The average tensile strength and modulus were determined as 235±54 MPa and 6.332±0.05 GPa, respectively.

3.3. Thermal analysis of fibers

Figure 4 depict the thermogravimetric (TG) and differential thermogravimetric (DTG) curves of SF, revealing the thermal degradation behavior of fibers. Thermogravimetric analysis (TGA) shows that the weight of the fibers decreases as the temperature increases. Initial degradation observed between 30 and 130 °C can be attributed to the moisture removal from the fibers. The second stage of degradation is due to the pyrolysis of cellulose and hemicellulosic content of fibers, which can be observed between 130 and 380 °C. Removal of lignin compounds from the surface of fibers due to pyrolysis was the reason

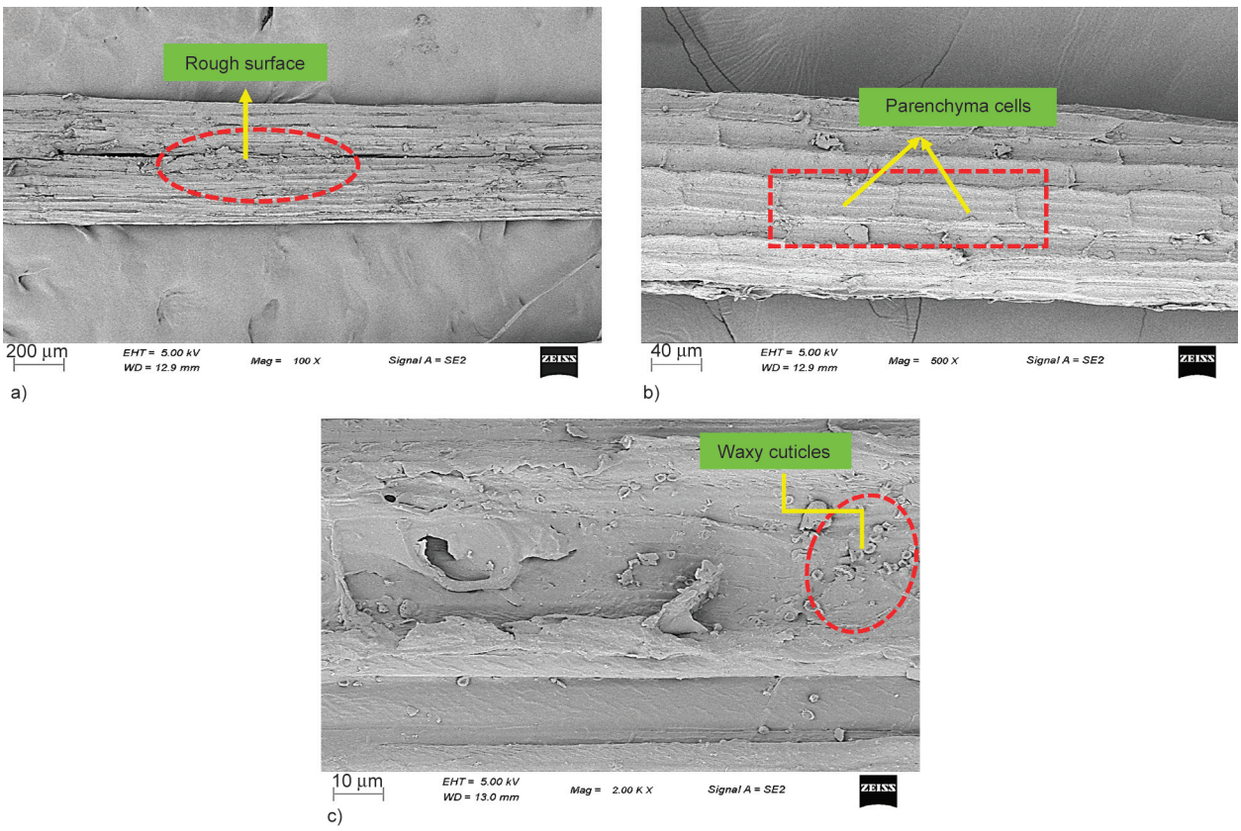

Figure 2. SEM images of untreated sisal fiber at different magnifications: a) 100×, b) 500×, c) 2000×.

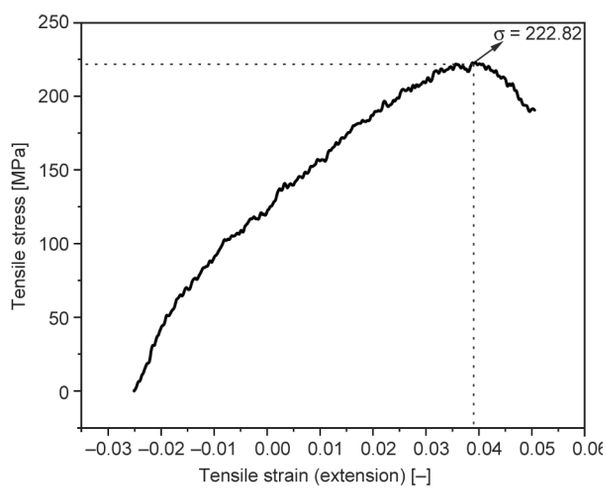

Figure 3. Typical stress-strain curve of USF.

for the third phase of thermal degradation of SFs, which was observed between 350 and 700 °C [25]. Figure 4b shows the DTG peaks for each step of degradation indicated by the TGA curves. The peaks of the DTG curve describe the weight loss rate [µg/min] against temperature. The degradation peak around 65 °C represented moisture evaporation from sisal fibers when heated. The degradation peak around 290 °C shows the thermal breakdown of hemicellulose. A maximum weight loss of 1.3 mg/min around 356 °C can be observed because of the pyrolysis of the cellulosic component of the fibers [25, 26].

3.4. Mechanical properties of biocomposites

3.4.1. Tensile properties

The effect of fiber content on the mechanical properties of developed biocomposites has been analyzed and summarized in Figure 5, and values are tabulated in Table 2. According to Figure 5a, the tensile strength of PLA/SF composites increased as the sisal fiber weight percentage increased to 20 wt% (45.12 MPa) and thereafter, reduced to 39.72 MPa at 30 wt% fiber concentration. The decrease in tensile strength after achieving the maximum value may be attributed to fiber agglomeration, which minimizes the fiber-matrix interfacial surface interaction in composites. Subsequently, the applied load is not effectively transferred from the matrix to the stiff fibers. Adding more fibers also causes non-uniform fiber dispersion in the PLA matrix [27, 28]. In the case of bio PBS/SF composites, the tensile strength decreased initially; thereafter, it was found to increase, with a maximum value of 29.12 MPa at 30 wt% of fiber loading. Adding SFs increased the strength of SF/bio PBS composites due to the uniform distribution of SFs that enable better

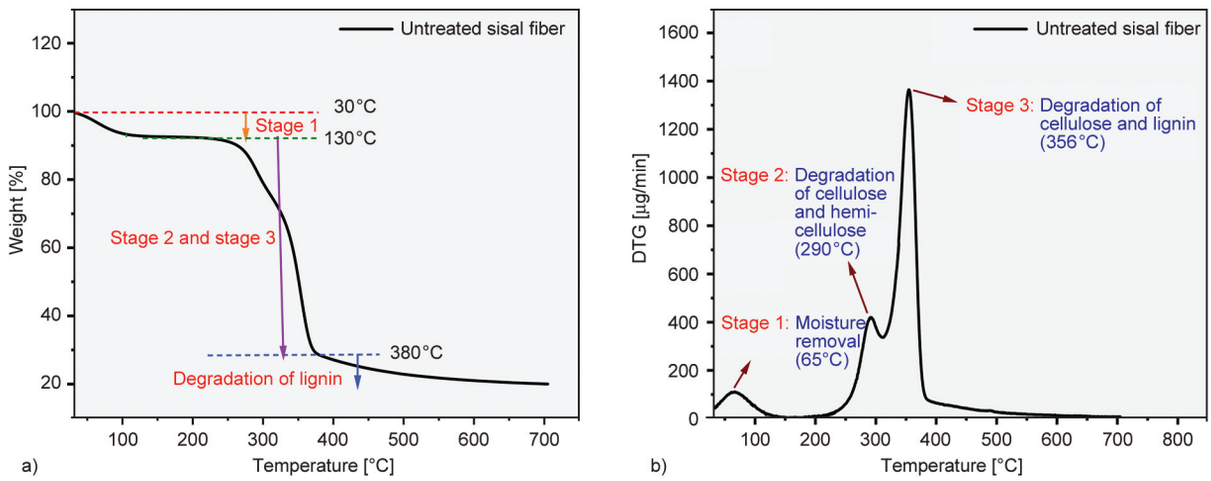

Figure 4. a) TGA and b) DTG curves of untreated sisal fiber.

load transmission. The existence of similar phenomena was observed in the study of bio PBS/PLA/Bamboo fibers based composite materials [29].

It is evident from Figure 5b that the tensile modulus of all PLA/SF and bio PBS/SF composites have a higher value than those of the respective pure matrix. The amount of fiber content in the matrix significantly impacts the increase in tensile modulus. The tensile modulus of PLA/SF composites increased by approximately 14.0, 33.5, and 68.1%, respectively, when 10, 20, and 30 wt% of SF were added to the PLA matrix. Similarly, the tensile modulus of bio PBS/SF composites increased by 8.8, 171.5, and 279.7%, respectively. The addition of stiff SFs improves the stiffness of the polymer composite. As developed composites are rigid, a given quantity of strain within

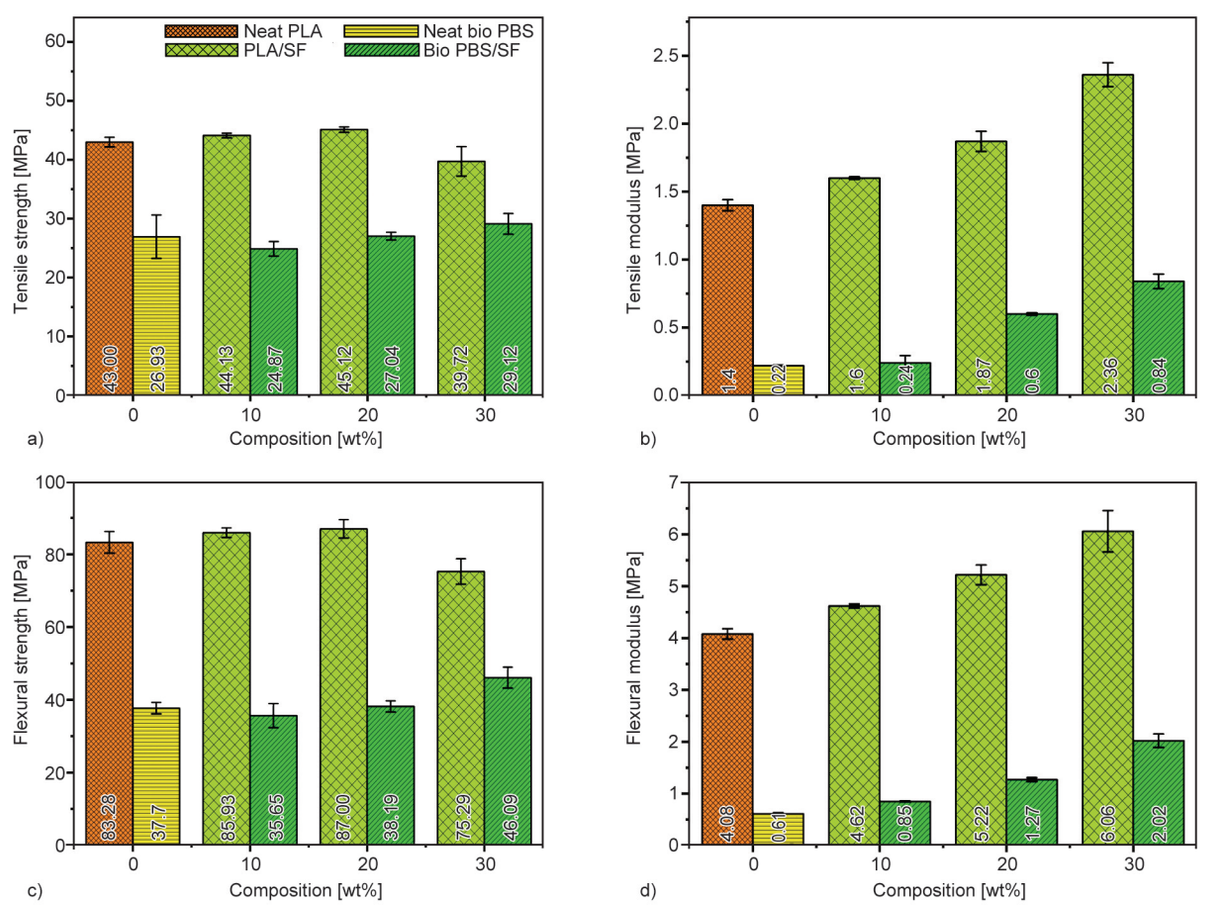

Figure 5. a), b) Tensile and c), d) flexural properties of biocomposites.

elastic limits necessitates higher tension. As a result, the tensile modulus of composites increased [30].

3.4.2. Flexural properties

The flexural properties of PLA/SF and bio PBS/SF composites were evaluated under a three-point bending load, and the results are shown in Figures 5c and 5d. The maximum flexural strength values of the PLA/SF and bio PBS/SF composites were 87.00 MPa (at 20SF/PLA) and 46.09 MPa (at 30SF/bio PBS), respectively, demonstrating good stiffness and higher rigidity. The flexural modulus significantly increased as the fiber content increased. An enhancement of 48.4% (with 30 wt% of SF) and 228.5% (with 30 wt% of SF) was found to be the maximum in SF/PLA and SF/bio PBS composites, respectively. Compared to bio PBS/SF biocomposites, PLA/SF biocomposites have less percentage change in tensile and flexural characteristics. This difference might be attributed to SF/bio PBS composites having better interfacial bonding and good processability with sisal fibers than SF/PLA composites.

3.4.3. Impact strength

As depicted in Table 2, the results reveal that fiber loading reduced the impact resistance of the developed biocomposites. The lower interfacial strength between matrix and sisal fibers may lead to the low-impact energy absorption of developed composites. The increased fiber loading creates stress concentration sites at the fiber-matrix interface, which leads to decreased impact strength of developed biocomposites [31]. The chemical constituents, matrix characteristics, interfacial bond strength between the matrix and fiber, and the void content significantly influence the impact strength of biocomposites.

3.5. Morphological analysis of developed composites

The SEM images of fractured surfaces after tensile testing of the SF/bio PBS and SF/PLA composites are depicted in Figure 6. In Figure 6, the first three images (Figures 6a–6c) describe the morphology of SF/bio PBS composites with 10, 20, and 30 wt% fiber content, respectively. Similarly, the last three pictures (Figures 6d–6f) describe the morphology of SF/PLA composites. The SEM micrograph (Figure 6c) of the 30SF/bio PBS composite has shown better fiber-matrix interaction when compared to 10 and 20 wt% SF/bio PBS composites. The strong fiber-matrix interaction promotes load transfer between the matrix and untreated sisal fiber. Also, Figure 6c shows fiber breakage. Fiber breakage is only conceivable when strong interfacial adhesion exists between the matrix and fiber. On the other hand, as seen in the 10SF/bio PBS composite (Figure 6a), weak interfacial bonding (fiber debonding) inevitably leads to fiber pull-outs and voids. However, fewer fiber pull-outs were observed in 30SF/bio PBS composite (Figure 6c), proving that 30 wt% of sisal fiber loading has good compatibility with bio PBS [32].

The mode of fracture of composites made of 10SF/PLA, 20SF/PLA, and 30SF/PLA under tensile loading is depicted in Figures 6d, 6e, and 6f, respectively. The absence of adequate adhesion between the constituents in the composites leads to fiber pull-outs, as we can observe in 10 and 30 wt% SF/PLA composites [30]. These micrographs also revealed voids, fiber bending, and PLA matrix cracking (due to stress concentration). 30SF/PLA (Figure 6f) has demonstrated a weaker fiber-matrix interface than its counterparts. In the case of 10SF/PLA and 30SF/PLA composites, weak interfacial bonding inevitably causes

Table 2. Mechanical properties of developed composites.

Composition	Tensile strength [MPa]	Tensile modulus [GPa]	Flexural strength [MPa]	Flexural modulus [GPa]	Impact strength [J/m]
Neat PLA	43.00±3.81	1.40±0.04	83.28±2.97	4.08±0.10	74.28±1.34
10SF_PLA	44.13±0.40	1.60±0.01	85.93±1.31	4.62±0.04	33.70±1.50
20SF_PLA	45.12±0.47	1.87±0.07	87.00±2.54	5.22±0.19	44.34±2.75
30SF_PLA	39.72±2.51	2.36±0.08	75.29±3.50	6.06±0.40	54.30±0.80
Neat bio PBS	26.93±3.68	0.22±0.01	37.70±1.58	0.61±0.02	87.75±1.17
10SF_bio PBS	24.87±1.24	0.24±0.05	35.65±3.33	0.85±0.01	38.74±3.57
20SF_bio PBS	27.04±0.65	0.60±0.01	38.19±1.52	1.27±0.04	48.16±3.00
30SF_bio PBS	29.12±1.75	0.84±0.05	46.09±2.87	2.02±0.13	72.14±9.93

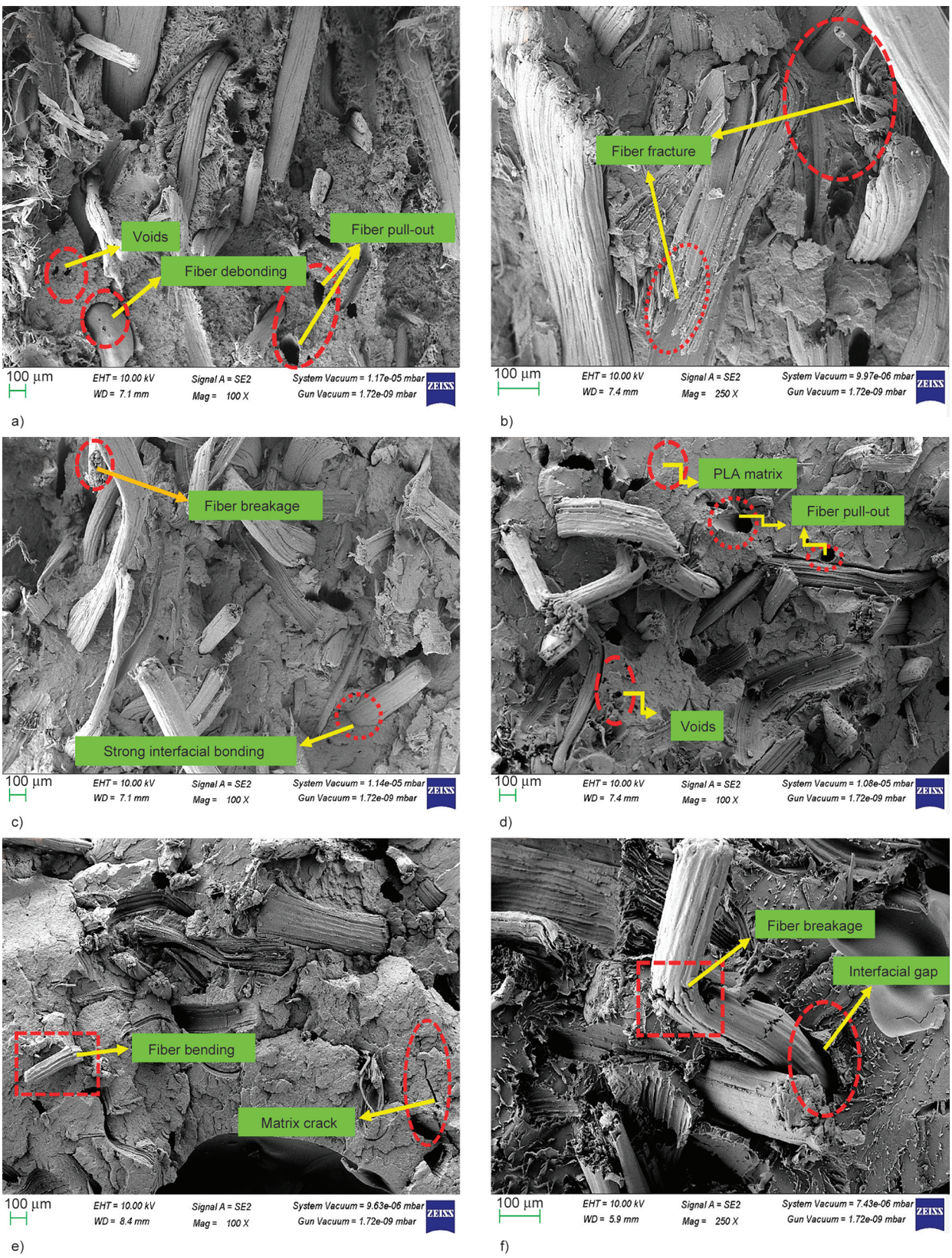

Figure 6. SEM images of a)–c) SF/bio PBS and d)–f) SF/PLA biocomposites after tensile testing.

fiber pull-outs and voids, leading to poor mechanical properties.

From the SEM micrographs, we can observe that 30SF/bio PBS (Figure 6c) and 20SF/PLA (Figure 6e) have shown better results than their counterparts, which was also substantiated by respective mechanical properties and degree of crystallinity of these composites.

3.6. Thermal properties of biocomposites

The weight loss of the biocomposites varies according to temperature, as demonstrated in Figures 7a and 7d. The thermal degradation pattern is consistent across all biocomposites. Due to the inclusion of sisal fibers into the matrix, the thermal degradation temperature of the developed biocomposites was slightly reduced. This may be because the relative molecular mass of the matrix was reduced, and the amount of the fibers increased leading to higher cellulose, hemicellulose, and lignin content in the composites. Since these chemical constituents of fiber are prone to thermal degradation, therefore, a decrease in the degradation temperature of biocomposites was

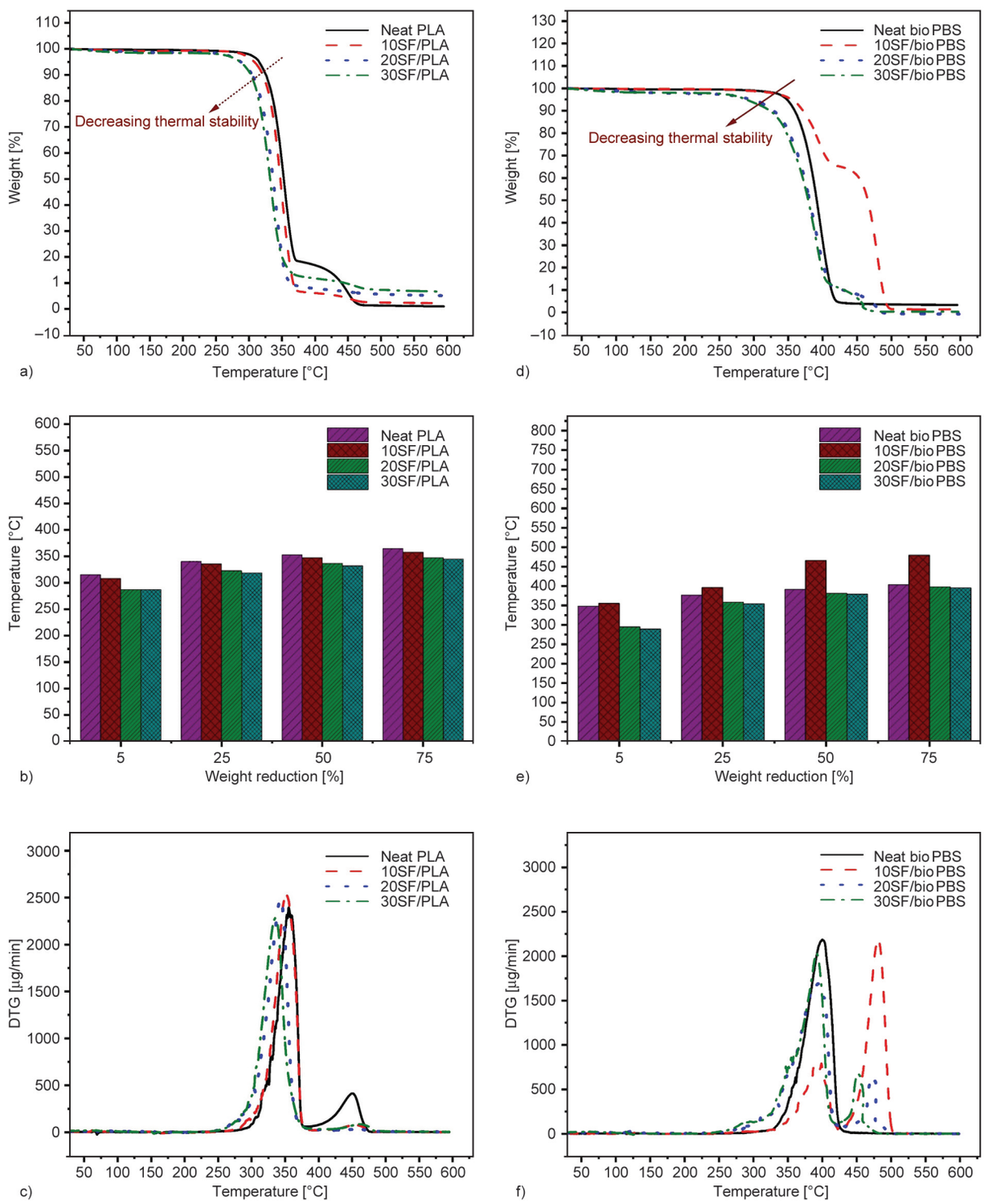

Figure 7. TGA (a), (d), weight reduction (b), (e), and DTG graphs (c), (f) for SF/PLA and SF/bio PBS composites, respectively.

observed [33]. In Figures 7b and 7e, a graphic representation of the weight loss [%] with the temperature is shown. It can be seen that, at the temperature ranges of 287–316, 318–340, 332–353, and 345–365 °C, respectively, all SF/PLA biocomposites lost 5, 25, 50, and 75% of their weight.

Similarly, in the case of SF/bio PBS composites, temperature ranges for similar weight loss [%] are 289–355, 355–397, 379–466, and 395–480 °C, respectively. From the results, it can be observed that SF/bio PBS biocomposites have better thermal stability than SF/PLA composites. Figure 7d shows the weight loss curves for the SF/bio PBS composites. Results showed that up to 200 °C, biocomposites had similar thermal stability as the pristine matrix. However, the thermal degradation behavior changed significantly when sisal fiber concentration increased to 30 wt% due to the lower thermal stability of constituents (cellulose, hemicellulose) of fibers [33]. The weight loss of the developed biocomposites with respect to temperature variation is categorized into three stages. The weight loss at 75–160 °C (SF/PLA composites) and 75–190 °C (SF/bio PBS composites) is related to moisture evaporation in the SF. Weight loss in the temperature range of 370 and 471 °C for SF/PLA composites and between 420 and 493 °C for SF/bio PBS composites is attributable to the pyrolysis of residual lignin and the pyrolysis of the matrix [33]. The peak in DTG curves for the SF/PLA and SF/bio PBS composites are depicted in Figures 7c and 7f, respectively. The highest weight loss was recorded between 255 and 370 °C for SF/PLA composites and between 250 and 420 °C for SF/bio PBS composites, representing the pyrolysis of the matrix and hemicellulose as well as cellulose present in the fibers. A comparable thermal disintegration pattern was determined for all biocomposites, indicating that thermal degradation behavior is not significantly impacted by fiber loading in the case of the developed composites. Figure 7f demonstrates that the virgin bio PBS only exhibits one degradation stage in the DTG profile, whereas composites exhibit two degradation steps. The degradation of the sisal fibers causes the first degradation to occur at 290 °C, while the degradation of the bio PBS matrix is responsible for the second degradation, which occurs at 401 °C [31, 35]. In the case of SF/bio PBS composites, the introduction of fibers resulted in a new interface (between fiber-matrix) which results in a change of thermal degradation mechanism, and therefore, the developed composites depicted two degradation peaks. Regarding the 10SF/bio PBS composite, we can observe the intense peak similar to the neat PBS degradation peak stated that 10SF/bio PBS follows the pristine PBS degradation process rather than the composite degradation process because 10SF/bio PBS has inadequate fiber content to be compatible with bio PBS. This is also evidence of decreased mechanical properties at 10SF/bio PBS. TGA and DTG results can be used to select operating conditions for the fabrication of biocomposite products. It is necessary to keep the processing temperature below 250 °C to prevent the thermal deterioration of developed biocomposites.

3.7. XRD analysis

The characteristics of biocomposites are substantially influenced by the crystallinity level. XRD analysis was used to assess the effect of sisal fiber loading on the crystallinity of the biocomposites. The XRD spectra for the surface of biocomposites are displayed in Figure 8. The software (Origin 2022b) was adopted

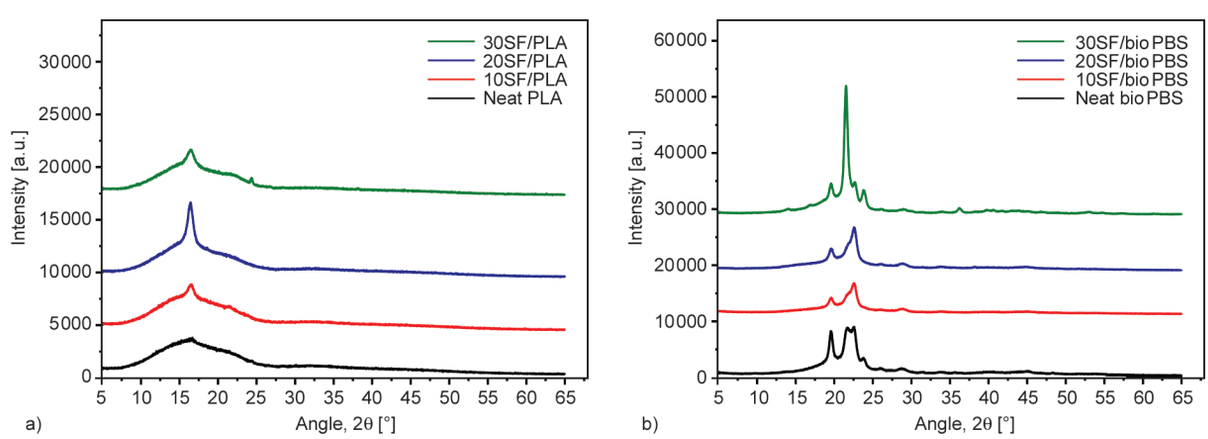

Figure 8. XRD spectra of a) SF/PLA and b) SF/bio PBS biocomposites.

to interpret the obtained data and calculate the total and crystalline area under the curve. The XRD patterns of pure PLA and SF/PLA green composites are shown in Figure 8a. XRD patterns of virgin PLA exhibit only one broad peak without sharp peaks at about $2\theta = 16.44°$. In the XRD spectra of SF/PLA composites, a single diffraction peak is detected, and the strength of this peak is ascertained to be greater and sharper than that of virgin PLA, suggesting increased crystallinity. In SF/PLA composites, comprising 10 to 30 wt% SF, the degree of crystallinity was almost 14.77, 17.88, and 16.81%, respectively [30, 36]. As illustrated in Figure 8b, the XRD for bio PBS provides three diffraction peaks at 19.6°, 21.71°, and 22.56° (with a variation of about ±0.2° [37]). The inclusion of fibers encourages structural alterations, and plane peaks frequently merge and change intensities [37]. From the results, the crystallinity index of pristine bio PBS was 37.03%, which was identified as a semi-crystalline polymer [38]. A degree of crystallinity of almost 33.04, 34.84, and 41.13% was obtained in SF/bio PBS composites comprising 10, 20, 30 wt% SF, respectively. Significant peaks between 16.44° and 22.56° in these composites confirm the existence of cellulose-I (existed between the fiber-matrix interface), proving the polymorphic nature of the composite structure. An interface between the fibers and the matrix can be created during extrusion as fibers and polymer pellets are compounded. Subsequent processing (injection molding) can improve the interfacial characteristics between constituents, increasing the crystallinity of composites. Compared to their counterparts, the crystallinity of the 20SF/PLA (20 wt% SF with PLA matrix) and 30SF/bio PBS (30 wt% SF with bio PBS matrix) biocomposites was found to be the highest. Generally, in plant fibers, cellulose is made of hydrocarbons, which determine the crystallinity of fibers and provide strength and stiffness because cellulose itself acts as a reinforcement in microfibrils of fibers. In biocomposites, natural fibers act as nucleating agents, changing composites' structural order. Therefore, cellulose and hemicellulose content in fibers affect the crystallinity and subsequently the mechanical and thermal properties of biocomposites.

3.8. DMA results

Figure 9 depicts the temperature-dependent variation of storage modulus (E'), loss modulus (E''), and tan δ of the SF/PLA and SF/bio PBS composites. Figures 9a and 9d have shown the temperature-dependent areas where the physical state of the neat polymers and their biocomposites has changed. The polymer and its biocomposites are often rigid and hard in the glassy zone (in the case of SF/bio PBS composites, the measurement starts at a temperature lower than –45 °C so that we can observe a very narrow region in Figure 9d). Beyond this zone, the material starts deforming due to increased temperature. Hence the behavior of the material has changed. At room temperature (around 30 °C), PLA is hard and brittle because it is in a glassy region, whereas bio PBS is soft and ductile as it is in the rubbery zone.

From Figures 9a and 9d, when SF is added to the matrix, E' significantly improves, which may be attributed to the better stress transfer efficiency between fiber and matrix [34]. The greater the value of E', the more rigid the material and the lower its deformation capacity. The movement of polymer molecular units and side groups is closely correlated with E' values [19]. The findings show that the E' values for all composite specimens are higher in the glassy region (rigid zone) since the material is hard and has lower deformation capacity in the glassy region, resulting in significant resistance to movement in the molecular chain. As the temperature increases, the values of E' slowly decline because of the reduction of stiffness in the fiber and improved molecular mobility of biopolymeric chains (increased temperature weakens the intramolecular bond strength of polymeric chains) [39]. At ambient temperature, SF/PLA composites are in the glassy region, whereas SF/bio PBS composites are in the rubbery zone and are ductile at room temperature. A sudden fall in E' was recorded for the SF/PLA specimens and SF/bio PBS specimens, respectively, in the temperature ranges of 55 to 65 °C and –45 to 0 °C, corresponding to a reduction in stiffness at the glass transition zone (T_g) [40, 41]. The 20SF/PLA (14232.69 MPa) and 30SF/bio PBS (11749.10 MPa) composites have higher storage modulus than their counterparts, associated with enhanced interfacial bonding between composite constituents as a result of the bolstering of interfaces. The storage modulus of 20SF/PLA and 30SF/bio PBS composites was almost 67 and 170% higher than the E' of the PLA matrix and bio PBS matrix, respectively. Furthermore, an increase in crystallinity could contribute to the growth in the storage modulus of the 20SF/PLA and 30SF/bio PBS composites. The increase in crystallinity

indicates a rise in the number of crystalline regions in the composites, which could serve as reinforcement or cross-linking for the amorphous areas, increasing the load-bearing properties of the 20SF/PLA and 30SF/bio PBS composites.

The viscous reaction of a substance is usually referred to as the loss modulus (E''). It concerns the movement of polymeric chains in composites that have been produced. Figures 9b and 9e show that the loss modulus of 30SF/PLA (2238.87 MPa) and 30SF/bio PBS (808.63 MPa) composites are significantly higher than that of virgin polymers. The mobility of polymer molecular chains is impeded and causes a rise in the viscosity of biocomposites because

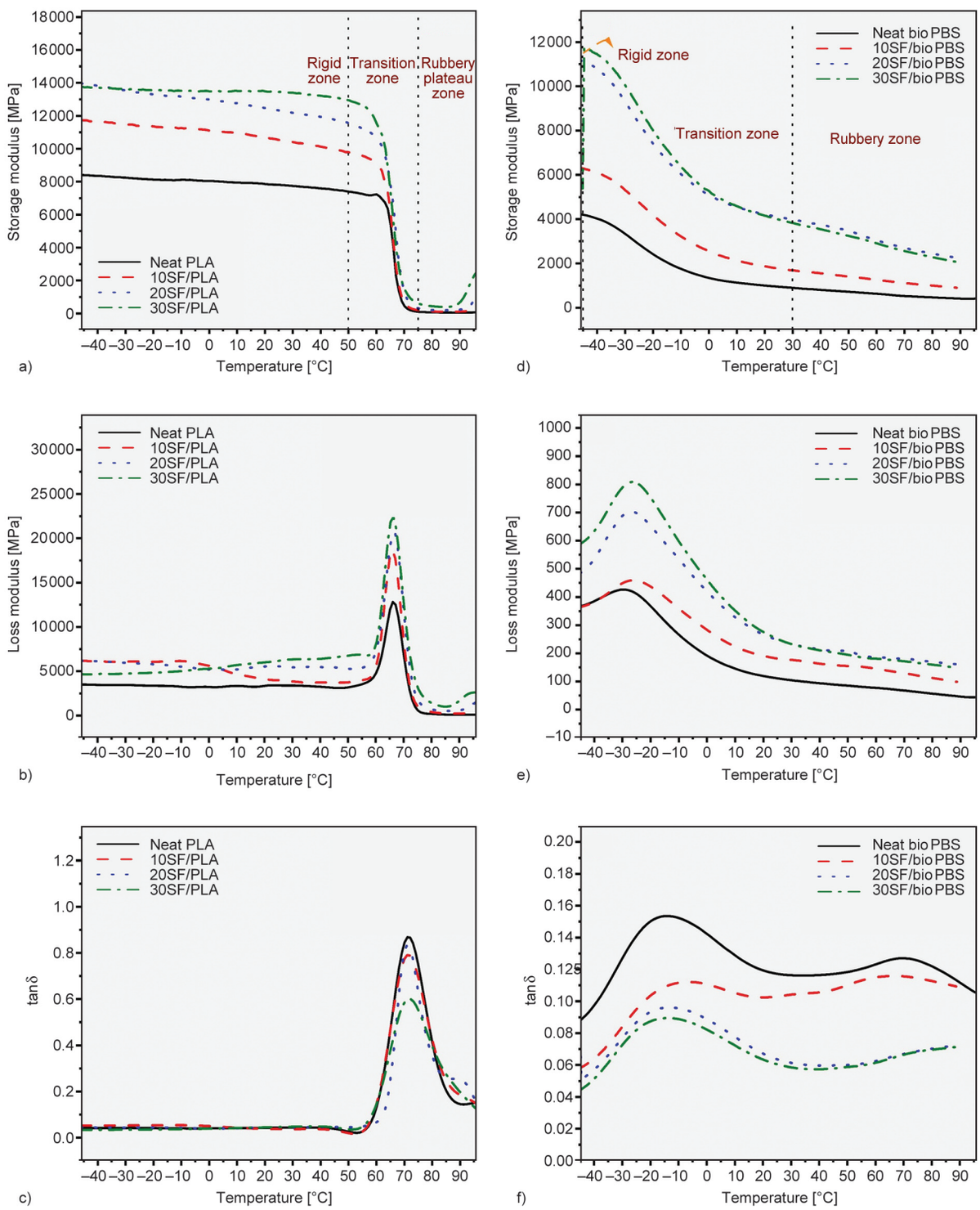

Figure 9. Storage modulus (a), (d), loss modulus (b), (e), and tan δ (c), (f) for SF/PLA and SF/bio PBS composites, respectively.

fibers increase stiffness and restrict the movement of polymeric chains in the composites [30]. The loss modulus of the 30SF/PLA and 30SF/bio PBS composites was around 74 and 89% greater than the loss modulus of the PLA matrix and the bio PBS matrix, respectively. Interfacial bonding between PLA and SF is low compared to bio PBS and SF. Hence, the increased percentile change in the loss modulus was more in SF/bio PBS composites.

Tan δ is also known as the damping coefficient or the loss factor. The loss factor is shown in Figures 9c and 9f as a function of temperature. The peak in the curves for each developed composite decreased compared to virgin polymers. It could be owing to the integration of SF, which leads to an interaction of the matrix and fiber, restricting the motion of polymeric chains. The tan δ peak height is commonly used to evaluate the damping capabilities of composites. Tan δ values for pure PLA and pure bio PBS are 0.868 and 0.153, respectively. On the other hand, the tan δ peak of the composite decreases with the addition of sisal fibers, which is due to interfacial interaction between the matrix and the fibers, inhibiting molecular mobility.

According to the results of DMA, it is evident that the increased percentile changes in E' and E'' values of SF/bio PBS composites were more than the SF/PLA composites. It is because the fibers and matrix have strong interfacial bonds and minimal defects during the fabrication of these types of composites, as observed in SEM analysis also.

4. Conclusions

The potential of sisal fiber as reinforcement for developing biodegradable SF/PLA and SF/bio PBS thermoplastic composites was experimentally investigated. The current research findings suggest that sisal fibers can be successfully incorporated into PLA and bio PBS biodegradable polymers to produce biocomposites. Extrusion-injection molding was used to fabricate SF/PLA and SF/bio PBS biocomposites with fiber content varying from 10 to 30 wt%. The primary conclusions of the current investigation are as follows;

- The maximum tensile and flexural strength of the SF/PLA and SF/bio PBS composites were observed at 20 and 30 wt% of fiber loading, respectively. On the other hand, the tensile and flexural modulus of developed composites increased with an increase in fiber loading from 10 to 30 wt% because the incorporation of rigid sisal fibers enhanced the modulus of biocomposites.
- The sisal fiber loading influences the thermal characteristics of developed composites because increased fiber loading results in increased cellulose and hemicellulose content in composites, which is thermally unstable at elevated temperatures.
- The degree of crystallinity of the 20SF/PLA (17.88%) and 30SF/bio PBS (41.13%) biocomposites was recorded to be maximum which consequently also led to the better mechanical properties of these composites.
- The SEM images have shown better fiber-matrix interfacial bonding for 20 and 30 wt% of the sisal fiber content for SF/PLA and SF/bio PBS composites, respectively. Fiber breakage was the major failure mechanism observed indicating good adhesion between PLA/bio PBS and the sisal fibers.
- The storage and loss modulus of developed composites increased with fiber loading from 10 to 30 wt%. The increased percentile change in mechanical, crystallinity, and DMA properties of SF/bio PBS composites was found to be higher than SF/PLA composites as compared to the neat polymers.

Additionally, it has been concluded that short-sisal fiber-based biocomposites have enormous potential for usage in various lightweight, secondary load-bearing, and non-structural applications, including dashboards, door panels, and other interior parts of automobiles. The produced biocomposites can also be used as paperweights, phone cases, and mirror casings. Thus for ensuring widespread commercial application of sustainable composite materials, the optimization of the fiber loading and development of good quality, cost-effective fabrication/processing techniques is necessary.

Acknowledgements

The authors would like to acknowledge the financial support provided by the Ministry of Education (MoE), Government of India.

References

[1] Nanni A., Messori M.: Thermo-mechanical properties and creep modelling of wine lees filled polyamide 11 (PA11) and polybutylene succinate (PBS) bio-composites. Composite Science and Technology, **188**, 107974 (2020). https://doi.org/10.1016/j.compscitech.2019.107974

[2] Song H., Lee S. Y.: Production of succinic acid by bacterial fermentation. Enzyme and Microbial Technology, **39**, 352–361 (2006). https://doi.org/10.1016/j.enzmictec.2005.11.043

[3] Zeikus J. G., Jain M. K., Elankovan P.: Biotechnology of succinic acid production and markets for derived industrial products. Applied Microbiology and Biotechnology, **51**, 545–552 (1999). https://doi.org/10.1007/s002530051431

[4] Yim H., Haselbeck R., Niu W., Pujol-Baxley C., Burgard A., Boldt J., Khandurina J., Trawick J. D., Osterhout R. E., Stephen R., Estadilla J., Teisan S., Schreyer H. B., Andrae S., Yang T. H., Lee S. Y., Burk M. J., Van Dien S.: Metabolic engineering of *Escherichia coli* for direct production of 1,4-butanediol. Nature Chemical Biology, **7**, 445–452 (2011). https://doi.org/10.1038/nchembio.580

[5] Aeschelmann F., Carus M.: Biobased building blocks and polymers in the world: Capacities, production, and applications-status quo and trends towards 2020. Industrial Biotechnology, **11**, 154–159 (2015). https://doi.org/10.1089/ind.2015.28999.fae

[6] Xu L., Zhao J., Qian S., Zhu X., Takahashi J.: Green-plasticized poly(lactic acid)/nanofibrillated cellulose biocomposites with high strength, good toughness and excellent heat resistance. Composites Science and Technology, **203**, 108613 (2021). https://doi.org/10.1016/j.compscitech.2020.108613

[7] Silva C. G., Campini P. A. L., Rocha D. B., Rosa D. S.: The influence of treated eucalyptus microfibers on the properties of PLA biocomposites. Composites Science and Technology, **179**, 54–62 (2019). https://doi.org/10.1016/j.compscitech.2019.04.010

[8] Yusoff R. B., Takagi H., Nakagaito A. N.: Tensile and flexural properties of polylactic acid-based hybrid green composites reinforced by kenaf, bamboo and coir fibers. Industrail Crops and Products, **94**, 562–573 (2016). https://doi.org/10.1016/j.indcrop.2016.09.017

[9] Mtibe A., Motloung M. P., Bandyopadhyay J., Ray S. S.: Synthetic biopolymers and their composites: Advantages and limitations – An overview. Macromolecular Rapid Communications, **42**, 2100130 (2021). https://doi.org/10.1002/marc.202100130

[10] Verma D., Fortunati E.: Biopolymer processing and its composites: An introduction. in 'Biomass, biopolymer-based materials and bioenergy' (eds.: Verma D., Fortunati E., Jain S., Zhang X.) Woodhead, Sawston, 3–23 (2019). https://doi.org/10.1016/B978-0-08-102426-3.00001-1

[11] Fiore V., Scalici T., Nicoletti F., Vitale G., Prestipino M., Valenza A.: A new eco-friendly chemical treatment of natural fibres: Effect of sodium bicarbonate on properties of sisal fibre and its epoxy composites. Composites Part B: Engineering, **85**, 150–160 (2016). https://doi.org/10.1016/j.compositesb.2015.09.028

[12] Bekele A. E., Lemu H. G., Jiru M. G.: Experimental study of physical, chemical and mechanical properties of enset and sisal fibers. Polymer Testing, **106**, 107453 (2022). https://doi.org/10.1016/j.polymertesting.2021.107453

[13] Thomas B. C., Jose Y. S.: A study on characteristics of sisal fiber and its performance in fiber reinforced concrete. Materials Today: Proceedings, **51**, 1238–1242 (2022). https://doi.org/10.1016/j.matpr.2021.07.312

[14] Pantaloni D., Rudolph A. L., Shah D. U., Baley C., Bourmaud A.: Interfacial and mechanical characterisation of biodegradable polymer-flax fibre composites. Composites Science and Technology, **201**, 108529 (2021). https://doi.org/10.1016/j.compscitech.2020.108529

[15] Ngaowthong C., Borůvka M., Běhálek L., Lenfeld P., Švec M., Dangtungee R., Siengchin S., Rangappa S. M., Parameswaranpillai J.: Recycling of sisal fiber reinforced polypropylene and polylactic acid composites: Thermo-mechanical properties, morphology, and water absorption behavior. Waste Management, **97**, 71–81 (2019). https://doi.org/10.1016/j.wasman.2019.07.038

[16] Zhu Z., Hao M., Zhang N.: Influence of contents of chemical compositions on the mechanical property of sisal fibers and sisal fibers reinforced PLA composites. Journal of Natural Fibers, **17**, 101–112 (2020). https://doi.org/10.1080/15440478.2018.1469452

[17] Feng Y-H., Zhang D-W., Qu J-P., He H-Z., Xu B-P.: Rheological properties of sisal fiber/poly(butylene succinate) composites. Polymer Testing, **30**, 124–130 (2011). https://doi.org/10.1016/j.polymertesting.2010.11.004

[18] Bajpai P. K., Singh I., Madaan J.: Comparative studies of mechanical and morphological properties of polylactic acid and polypropylene based natural fiber composites. Journal of Reinforced Plastics and Composites, **31**, 1712–1724 (2012). https://doi.org/10.1177/0731684412447992

[19] Yan X., Liu C., Qiao L., Zhu K., Tan H., Dong S., Lin Z.: Crystallization and dynamic mechanical behavior of coir fiber reinforced poly(butylene succinate) biocomposites. Journal of Renewable Materials, **10**, 1039–1048 (2022). https://doi.org/10.32604/JRM.2022.017239

[20] Li Y., Sang L., Wei Z., Ding C., Chang Y., Chen G., Zhang W., Liang J.: Mechanical properties and crystallization behavior of poly(butylene succinate) composites reinforced with basalt fiber. Journal of Thermal Analysis and Calorimetry, **122**, 261–270 (2015). https://doi.org/10.1007/s10973-015-4732-8

[21] Samouh Z., Molnar K., Boussu F., Cherkaoui O., El Moznine R.: Mechanical and thermal characterization of sisal fiber reinforced polylactic acid composites. Polymers for Advanced Technologies, **30**, 529–537 (2019). https://doi.org/10.1002/pat.4488

[22] Naik T. P., Gairola S., Singh I., Sharma A. K.: Microwave hybrid heating for moulding of sisal/jute/HDPE composites. Journal of Natural Fibers, **19**, 13524–13538 (2022). https://doi.org/10.1080/15440478.2022.2100553

[23] Silveira M. V., dos Santos Ferreira J. W., Casagrande M. D. T.: Effect of surface treatment on natural aging and mechanical behavior of sisal fiber–reinforced sand composite. Journal of Materials in Civil Engineering, **34**, 1–11 (2022). https://doi.org/10.1061/(asce)mt.1943-5533.0004237

[24] Gudayu A. D., Steuernagel L., Meiners D., Gideon R.: Effect of surface treatment on moisture absorption, thermal, and mechanical properties of sisal fiber. Journal of Industrial Textiles, **51**, 2853S–2873S (2022). https://doi.org/10.1177/1528083720924774

[25] Chaitanya S., Singh I.: Sisal fiber-reinforced green composites: Effect of ecofriendly fiber treatment. Polymer Composites, **39**, 4310–4321 (2018). https://doi.org/10.1002/pc.24511

[26] Ye C., Ma G., Fu W., Wu H.: Effect of fiber treatment on thermal properties and crystallization of sisal fiber reinforced polylactide composites. Journal of Reinforced Plastics and Composites, **34**, 718–730 (2015). https://doi.org/10.1177/0731684415579090

[27] Rajesh G., Ratna Prasad A. V., Gupta A. V. S. S. K. S.: Mechanical and degradation properties of successive alkali treated completely biodegradable sisal fiber reinforced poly lactic acid composites. Journal of Reinforced Plastics and Composites, **34**, 951–961 (2015). https://doi.org/10.1177/0731684415584784

[28] Sachin S. R., Kannan T. K., Rajasekar R.: Effect of wood particulate size on the mechanical properties of PLA biocomposite. Pigment & Resin Technology, **49**, 465–472 (2020). https://doi.org/10.1108/PRT-12-2019-0117

[29] Rasheed M., Jawaid M., Parveez B.: Preparation, characterization and properties of biodegradable composites from bamboo fibers – Mechanical and morphological study. Journal of Polymers and the Environment, **29**, 4120–4126 (2021). https://doi.org/10.1007/s10924-021-02158-7

[30] Pujar N. M., Mani Y.: Development and characterization of pigeon pea stalk fiber reinforced polylactic acid sustainable composites. Journal of Natural Fibers, **19**, 15637–15652 (2022). https://doi.org/10.1080/15440478.2022.2131684

[31] Pivsa-Art S., Pivsa-Art W.: Eco-friendly bamboo fiber-reinforced poly(butylene succinate) biocomposites. Polymer Composites, **42**, 1752–1759 (2021). https://doi.org/10.1002/pc.25930

[32] Nam T. H., Ogihara S., Nakatani H., Kobayashi S., Song J. I.: Mechanical and thermal properties and water absorption of jute fiber reinforced poly(butylene succinate) biodegradable composites. Advanced Composite Materials, **21**, 241–258 (2012). https://doi.org/10.1080/09243046.2012.723362

[33] Gairola S., Sinha S., Singh I.: Novel millet husk crop-residue based thermoplastic composites: Waste to value creation. Industrial Crops and Products, **182**, 114891 (2022). https://doi.org/10.1016/j.indcrop.2022.114891

[34] Komal U. K., Lila M. K., Singh I.: PLA/banana fiber based sustainable biocomposites: A manufacturing perspective. Composites Part B: Engineering, **180**, 107535 (2020). https://doi.org/10.1016/j.compositesb.2019.107535

[35] Gowman A., Wang T., Rodriguez-Uribe A., Mohanty A. K., Misra M.: Bio-poly(butylene succinate) and its composites with grape pomace: Mechanical performance and thermal properties. ACS Omega, **3**, 15205–15216 (2018). https://doi.org/10.1021/acsomega.8b01675

[36] Kaavessina M., Ali I., Al-Zahrani S. M.: The influences of elastomer toward crystallization of poly(lactic acid). Procedia Chemistry, **4**, 164–171 (2012). https://doi.org/10.1016/j.proche.2012.06.023

[37] Platnieks O., Gaidukovs S., Thakur V. K., Barkane A., Beluns S.: Bio-based poly(butylene succinate): Recent progress, challenges and future opportunities. European Polymer Journal, **161**, 110855 (2021). https://doi.org/10.1016/j.eurpolymj.2021.110855

[38] Bhattacharjee S. K., Chakraborty G., Kashyap S. P., Gupta R., Katiyar V.: Study of the thermal, mechanical and melt rheological properties of rice straw filled poly (butylene succinate) bio-composites through reactive extrusion process. Journal of Polymers and the Environment, **29**, 1477–1488 (2021). https://doi.org/10.1007/s10924-020-01973-8

[39] Kumar S., Zindani D., Bhowmik S.: Investigation of mechanical and viscoelastic properties of flax- and ramie-reinforced green composites for orthopedic implants. Journal of Materials Engineering and Performance, **29**, 3161–3171 (2020). https://doi.org/10.1007/s11665-020-04845-3

[40] Saffian H. A., Yamaguchi M., Ariffin H., Abdan K., Kassim N. K., Lee S. H., Lee C. H., Shafi A. R., Alias A. H.: Thermal, physical and mechanical properties of poly(butylene succinate)/kenaf core fibers composites reinforced with esterified lignin. Polymers, **13**, 2359 (2021). https://doi.org/10.3390/polym13142359

[41] Komal U. K., Lila M. K., Singh I.: Processing of PLA/pineapple fiber based next generation composites. Materials and Manufactuing Processes, **36**, 1677–1692 (2021). https://doi.org/10.1080/10426914.2021.1942904

Express Polymer Letters Vol.17, No.10 (2023) 1007–1018
Available online at www.expresspolymlett.com
https://doi.org/10.3144/expresspolymlett.2023.75

Research article

Monolayer films from poly(lactic acid) PLA/poly(3-hydroxybutyrate-*co*-hydroxyvalerate) PHBV blends for food packaging applications

Hosein Pouriman[1,2*], *Kevin Graham*[2], *Krishnan Jayaraman*[1]

[1]Centre for Advanced Composite Materials, Department of Mechanical and Mechatronics Engineering, The University of Auckland 1142, Auckland, New Zealand
[2]Friendlypak Ltd Corporation, 51b Rosebank Road, Avondale, 1026 Auckland, New Zealand

Received 6 April 2023; accepted in revised form 22 June 2023

Abstract. Four out of twelve different formulations consisting of poly(lactic acid) (PLA), poly(3-hydroxybutyrate-*co*-hydroxyvalerate) (PHBV), triethyl citrate (TC), and epoxy-functionalized styrene acrylate (ESA) components were selected based on their superior elongation at break, rheological properties, and composition range from other batches. Each batch was made into a monolayer thin film via a blown film extrusion process. The films' mechanical, oxygen gas, and moisture barrier and aesthetic properties were measured. The findings paved the understanding for developing biodegradable packaging to extend the shelf life of oxygen and moisture-sensitive food products. The results proved the significance of systematic analysis of the interacting effects of components' mixing ratios on different properties of the blend. The produced films' oxygen gas and moisture barrier properties showed significant improvement compared to neat PLA; however, still more than neat PHBV.

Keywords: *polymer blends and alloys, PLA-PHBV blend, flexible packaging, monolayer film, blown film extrusion*

1. Introduction

The packaging sector is the biggest global consumer of petroleum-based plastics and the largest contributor to global plastic waste [1]. It is determined that about 45% of the plastic packaging waste is used for food packaging [2]. This has led to a surge in research in the past decade in bio-based and biodegradable polymers to substitute petroleum-based plastics and offers a more sustainable production and waste solution for food packaging [1, 3]. The shelf life of plastic-packaged food products is specifically short due to the short shelf life of food products. Oxygen gas and moisture are particularly the two key factors influencing the shelf life of food. Curbing the diffusion of oxygen and moisture in packaging is essential to limit the initiation of biochemical spoilage reactions and microbial growth in packaged food. In order to achieve this goal, the factors affecting the solubility coefficient and diffusion of the packaging must be carefully considered. These factors include the processing method, chain orientation, degree of crystallinity of the polymers, and the size and shape of the penetrant. However, most of these factors are not in favor of bio-polymers; for instance, the slow crystallization rate and narrow processing window; hence most bio-polymers suffer from poor barrier properties [1].

Poly(lactic acid) (PLA) and poly(3-hydroxybutyrate-*co*-hydroxyvalerate) (PHBV) are two of the most produced bio-based and biodegradable polymers recently being employed in food packaging. PLA is an aliphatic polyester that can be derived via fermentation and chemical reactions from sustainable resources such as corn starch, cassava, potato starch,

*Corresponding author, e-mail: mpou994@aucklanduni.ac.nz
© BME-PT

rice, or sugar [4]. PLA is widely used in packaging as film and coating [5]. Similar to most biopolymers, PLA has its shortcomings. Slow crystallization rates, high brittleness, and poor barrier properties to gases such as oxygen, water vapor, and different aromas urge PLA to be blended with other polymers and additives to amend its properties to be more suitable for food packaging applications [6]. PHBV is a subset of polyhydroxyalkanoates (PHAs) and the copolymer of polyhydroxy butyrate (PHB)-hydroxyvalerate (HV) with significant ductility improvement over PHB polymer. PHAs are produced mostly from batch fermentation of bacteria and algae [7–9].

Many studies have been conducted on blends of PLA with PHAs at different mixing ratios, processing conditions, and for different applications. This is due to the synergistic effect as well as complementary properties [10–16] of these two polymers in the final blend. Table 1 summarises the properties of PLA and PHBV that are most important for food packaging applications.

Employing PLA and PHAs in flexible food packaging is specifically challenging due to the processing difficulties such as narrow processing windows and the brittleness of final products. Researchers employed different manufacturing methods to utilize PLA-PHAs combination in films. Some of the most notable works include solvent casting [26], compression molding [27, 28], and cast extrusion [29]. Guinault *et al*. [30] manufactured a multi-layer sheet composite via a coextrusion process with a total PLA:PHBV ratio of 90:10. The films' ductility was improved compared with neat PLA. The gas barrier properties of the films were also improved due to an increase in the crystallinity of the blend, which was corroborated by the observance of 'numerous long, thin crystallized lamellae' of PHBV in the layered composite. However, for comparison, the cooling time of final products in sheet extrusion (about 4 min) is significantly longer than for the blown film extrusion (about 10 s). This influences the molecular arrangement and degree of crystallinity, leading to higher barrier properties in sheet extrusion compared to blown film extrusion.

Hernández-García *et al*. [28] manufactured 75:25 ratio PLA-PHBV monolayer blends consisting of 15 wt% polyethylene glycol (PEG)/polymer mass and antimicrobial compounds via extrusion blending and compression molding. This study focused mostly on end-of-life options and active biodegradation of the blends, assuming the mixing ratio of the polymers and additives is suitable for food packaging applications. However, it was found earlier that the component contents can significantly affect the mechanical properties of the final blends. The closest research to the present study is the study done by Pietrosanto *et al*. [31] where monolayer blown-extruded films were manufactured from a melt-blended mixture of PLA:PHB ranging from 60:40 to 80:20 wt% without employing plasticizers. The resulting films showed an increase in ductility of the films and the degree of crystallization of PLA, hence, an improvement in barrier properties of the final films.

The significance of the present study is due that many papers reported a synergistic elongation at break increase from 250 to 5750% for PLA:PHBV blends with the ratio of 70:30 to 90:10 wt% [32–35], however, no studies have systematically investigated the interactive effect of each mixing component on the properties of the blend. We systematically explored this synergistic elongation effect region for the first time by defining a Mixture Design and identifying

Table 1. Summary of the most important properties of PLA and PHA for food packaging applications, adapted from [1, 3, 17–25].

Property/Polymer		PHAs	PLA
Elongation at break	[%]	1.4 to 5.5	0.5 to 9.2
Tensile strength	[MPa]	20 to 40	37 to 66
Glass transition temperature	[°C]	–9 to 9	55
Chemical resistance		Poor	Poor
Transparency		Medium	High
Water absorbance	[%]	0.7	3.1
Oxygen gas permeation (OP)	[cc.mil/(m^2·day·atm)]	8 (23 °C, 85%) 85 (23 °C, 0%) 230 (25 °C, 80%)	132–590 (23 °C, 0% or 50%)
Water vapor permeation (WVP)	[g·mil/(m^2·day·kPa)]	106 (23 °C, 50%) 30 (25 °C, 100%) 26 (37.8 °C, 100%)	63–342 (23 °C, 85%)

the most effective responses [36]. Four mixing compositions out of twelve were chosen to be processed into monolayer thin films based on their better exhibiting mechanical properties, rheological properties, and composition differences. The present paper studies the mechanical, barrier, and aesthetic properties of these films to understand and develop biodegradable flexible packaging based on PLA/PHBV blends for application in food products.

2. Materials and methodology

2.1. Materials

The PHBV and PLA polymer grades with the minimum difference in melting temperature were selected to minimize the chance of immiscibility of the blend. For PHBV, the polymer grade of ENMAT thermoplastic resin was supplied by TianAn Biopolymer (Ningbo, China) with T_m = 180 °C and MFI = 8–15 g/10 min, 180 °C, 2.16 kg). For PLA, Ingeo Biopolymer 2003D was supplied by NatureWorks (Minnesota, USA) with T_m = 160 °C, MFR = 6 g/10 min, 210 °C, 2.16 kg), and D-lactide content of 4.3%. This grade is suggested by the manufacturer as a grade used as part of a formulated blend. Triethyl citrate ($C_{12}H_{20}O_7$) (CAS-No 77-93-0), liquid state at room temperature, was used as a plasticizer with a molecular weight of 276.28 g/mol and supplied by Sigma Aldrich (Milwaukee, USA). An epoxy-functionalized styrene acrylate chain extender (Joncryl ADR 4468) was supplied by BASF, Singapore. Based on the supplier's claim, this polymeric chain extender reacts specifically with polycondensation polymers such as PLA and is used specifically for food contact applications. All materials were used as received without any treatment or modification.

2.2. Methodology

High values of melt strength and elongational viscosity of a polymer blend at molten state are the prerequisites for maintaining a stable bubble during the blown film extrusion process [37]. On the other hand, flexible packaging made via blown extrusion normally has high elongation at break values (>500%). Hence, a chain extender was added to the blend to improve the melt strength of the blend. Plasticiser was added to the blend to improve the elongation at break and boost the synergistic elongational effect of the blends. Mixture Design statistical analysis was employed to consider the synergistic elongation effect between the PLA/PHBV blend components

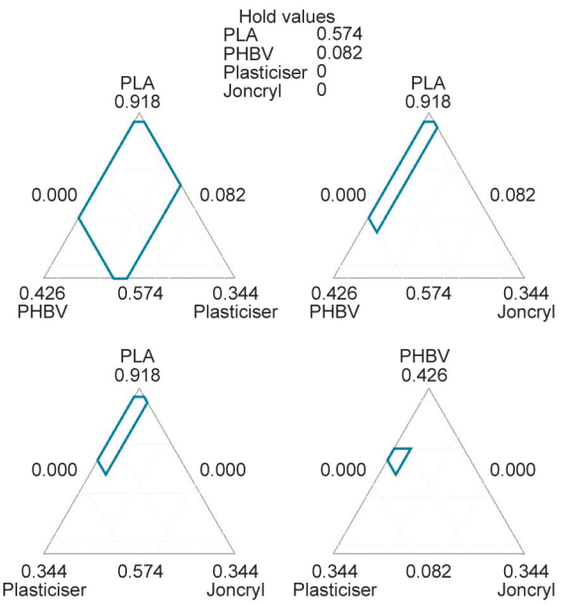

Figure 1. The material components simplex design plots [36].

within the 70/30 to 90/10 mixing ratios. PLA, PHBV, TC, and ESA were chosen as mixing components. Elongation at break and elongational viscosity were chosen as response surfaces to be maximized. A more thorough description of the statistical analysis could be found in our earlier work [36]. Figure 1 shows the simplex design plots of the mixing component. The extreme vertices design in a quadratic model with linear constraints of 0.82 < PLA + PHBV < 0.95 was considered.

Rheological results and trial tests showed that all twelve blends could be processed into blown films. However, the mechanical properties tests showed that batches 2, 3, 9, 10, 11, and 12 have the highest elongational strain values (near 200%). These blends all contained the highest plasticizer contents. Among these six candidate batches, batches 2, 3, 10, and 12 were chosen for blown film extrusion. This is because these batches contain a range of high and low PLA, PHBV, and ESA contents which would provide sufficient data for understanding the effect of component ratios on the properties of the final films. The material contents of selected batches for the blown film extrusion process are shown in Table 2.

Table 2. The weight percent materials of testing batches based on extreme vertices design in a quadratic model Mixture Design.

Batch	PLA	PHBV	Triethyl citrate	Joncryl
2	76.8	8.2	15	0
3	73.8	8.2	15	3
10	57.4	27.6	15	0
12	57.4	24.6	15	3

2.2.1. Sample manufacturing

The virgin PLA and PHBV pellets were subjected to a drying process at a temperature of 90 °C for 3 hours, which resulted in a moisture content of less than 0.025% (250 ppm). The PLA, PHBV, and ESA were premixed and then fed to the extruder through the hopper at a constant feeding speed. The TC was added to the extruder through a tube that was connected to a multi-syringe liquid pump (Cole-Parmer, IL, USA) equipped with a 60 ml syringe. Chain extenders are compounds with low molecular weight and bifunctional groups which have been reported to increase the molecular weight of biopolymers such as PLA and PHBV by engaging in a rapid reaction such as reacting with terminal alcohol groups in polyesters [38, 39]. The extrusion process was carried out using a co-rotating twin screw extruder (Labtech, Samut Prakan, Thailand) with an *L*/*D* ratio of 40:1, screw diameter of 25 mm, rpm of 75 and temperature profile of 160–180–185–190–185–180 °C for the different extrusion zones. The extruded filaments were then cooled down using an air-powered conveyer and wound onto filament spools. Some of the filaments were separated and used as a test sample for further mechanical tests. The remaining filaments were pelletized using an automatic pelletizer (Labtech, Samut Prakan, Thailand) to produce samples for rheological studies.

To manufacture monolayer film, the collected pelletized polymer blends were fed to a single screw blown film extrusion machine (Friend Machinery, Zhangjiagang, China) with an *L*/*D* ratio of 25, screw diameter of 25 mm and annular die diameter of 42 mm at rpm of 19 and heating profile of 170 °C for all zones. The blown film made from each batch was collected at the end of the machine via a mechanized thin film roller.

A set of compression molded films were manufactured to draw a comparison with blown film extruded samples. These samples were extruded, blended, and pelletized, similar to the rest. The blends were compression molded in the following sequence: The blend pellets (nearly 10 grams) were placed in the center of an aluminum frame with a thickness of 0.1 mm. Using a hydraulic press (Labtech, Samut Prakan, Thailand), the pellets were preheated to 180 °C at the point of contact of upper and lower heating plates for 4 min so that all pellets were molten and evenly spread across and within the frame. The molten materials were compressed for 1 min at 160 bar and then cooled to room temperature. The cooling time was set to 4 min. The compression molded samples were used only in oxygen transmission rate due to test limitations involved with water vapor permeability and mechanical properties.

2.2.2. Mechanical properties characterization

Tensile strength and elongation at break

Tensile strength, Young's modulus, and elongation at break of blown film samples were tested in both machine directions (MD), complying with ASTM D882-18 standard. The tests were conducted via a universal tensile testing machine (Instron 5567, Instron, Massachusetts, USA). A set of rubber-lined grips were used to hold the thin films in place. Strips of uniform thickness with a width of 15 mm were cut as test samples. An initial grip separation of 250 mm and a grip separation speed of 25 mm/min were used to determine the modulus of elasticity. To determine tensile strength, the initial grip separation was changed to 50 mm and crosshead speed to 500 mm/min.

Tear resistance

Tear-propagation resistance of the blown films was measured via the single-tear or trouser tear method based on ASTM D1938-19 standard via a universal tensile testing machine (Instron 5567, Instron, Massachusetts, USA). Sets consisting of at least five samples of 25×75 mm with the same thickness (varied between batches) were tested in both machine and transverse directions. The grip-separation speed was set to 250 mm/min. The test was continued until the tear was propagated through the entire unseparated part. A load [N] *vs*. time [s] graph was produced for each test. An average tear propagation force was calculated based on the films' performances. The initial force and maximum load point were used for highly extensible samples. For the non-extensible samples, the load was averaged over a 25.4 mm interval, disregarding the final and initial parts of the graph.

2.2.3. Barrier properties

Oxygen gas transmission rate

The oxygen gas transmission rate (O_2GTR) of the blown extruded films was measured by MOCON OX-TRAN® 2/10 (MN, USA) according to the ASTM F1927 standard. The tests were conducted at a recommended 10 sccm steady-state flow for oxygen gas (test gas), 0% relative humidity level for both the test gas and the carrier gas, and at a testing temperature

of 23 °C. In this test, the oxygen molecules permeate through the film, transporting them via a mixture of 98%-nitrogen/2%-hydrogen gases (carrier gas) to the coulometric device. The coulometric device generates a linear output as predicted by Faraday's law. In principle, four electrons are produced by the detector for each molecule of oxygen that passes through it. The amount of permeated oxygen was determined proportionately to the generated electric current. All test samples were cut via a 13 cm diameter annular cutting die to minimize the possible error due to variations of the area between the unmasked section of the samples. Each result was obtained from an average value from at least three samples. Samples were conditioned for 3 hrs before the tests. Conditioning in this test denotes the following sequence:

1. Before a measurement is taken, the samples are placed in the testing cell.
2. Test gas flows into the test cell, and oxygen molecules permeate the testing sample so that the sample reaches an equilibrium state with the testing condition.

The testing area of each film was 50 cm^2. Each film took 10 testing cycles, each cycle being 30 min, and the final permeation value was measured when the oxygen transmission rate (OTR) reached a constant level. To ensure that the coulometric sensor indicates the correct value for each specimen, the sensor was calibrated via the National Institute of Standards and Technology (NIST) certified calibration film with the O_2GTR of 0.198700 cc·mil/(pkg·day). The O_2GTR and permeance (PO_2) were determined as Equations (1) and (2):

$$O_2\text{GTR} = \frac{E_e - E_0}{A} \tag{1}$$

$$PO_2 = \frac{O_2\text{GTR}}{P} \tag{2}$$

where E_e is the steady state O_2GTR level [cc·mil/(m^2·day·atm)], E_0 is zero O_2GTR level [cc·mil/(m^2·day·atm)], A is specimen area [m^2] and P is the partial pressure of oxygen [atm], the mol fraction of oxygen multiplied by the total pressure (nominally, one atmosphere) in the test gas side. The partial pressure of O_2 on the carrier side is zero.

Water vapor transmission rate

The water vapor transmission rate (*WVTR*) test was carried out based on ASTM E96/E96M-16 standard. All the samples were cut via a 70 mm diameter annular cutting die to minimize the possible measurement error by keeping the exposed section of all samples equal, hence normalizing the passage of water vapor from outside the mouth section of the test vessels for all test specimens. Distilled water was poured into the light test vessels to a level of 20 mm from the specimen. Test dishes were placed in a controlled environment chamber with relative humidity maintained at 50% and temperature at 23 °C for a period of two months. The test assemblies were weighed once a day during this period to determine the rate of water vapor movement through the test films. To cancel out the possible adverse effect of the environment on the test dishes, an aluminum-foil-covered dish and an empty dish (a dummy unit) were also periodically weighed. The aluminum-foil-covered dish indicated the water that escaped through the water-repelling-grease used as a sealant for each test assembly. The empty dish indicated the weight changes of the test dish due to atmospheric conditions. An analytical balance sensitive to 0.0001 g was used for weighing. Water vapor transmission and permeance were calculated as Equation (3):

$$WVT = \frac{G}{t \cdot A} \tag{3}$$

where G is a weight change [g], t is time [h], G/t is the slope of the straight line [g/h], A is the test area or the cup mouth area [m^2] and WVT is the rate of water vapor transmission rate [g/(h·m^2] (Equation (4)):

$$\text{Permeance} = \frac{WVT}{\Delta p} = \frac{WVT}{S(R_1 - R_2)} \tag{4}$$

where Δp is a vapor pressure difference [mmHg, $1.333 \cdot 10^2$ Pa], S is saturation vapor pressure at test temperature [mmHg, $1.333 \cdot 10^2$ Pa], R_1 is relative humidity at the source expressed as a fraction in the dish, and R_2 is relative humidity at the vapor sink expressed as a fraction. Average permeability was calculated as Equation (5):

$$\text{Average permeability} = \text{Permeance} \cdot \text{Thickness} \tag{5}$$

The Equation (6) is used to correct the excess *WVT* due to edge masking:

$$\text{Percent excess } WVT = \frac{400t}{\pi S_1} \ln \frac{2}{1 + e^{-\frac{2\pi b}{t}}} \tag{6}$$

where t is specimen thickness [m], b is the width of masked edge [m], and S_1 is four times the test area divided by the perimeter [m].

3. Results and discussion

3.1. Mechanical properties

Four batches out of twelve were chosen to be processed into thin films. Although more than four blends had the capability to be filmed, however batches 2, 3, 10, and 12 were selected to provide the widest diversity of compositional content. For instance, the material contents in batch 9, which was also capable of being blown filmed, are close to batch 10. Hence batch 9 was omitted. This method was chosen to minimize the number of tests and identify the major differences in properties for the selected samples. If one sample is identified as best performing, the batches with close material contents would subsequently be investigated.

It is known that the mechanical properties of PLA/PHBV blend near 70:30 to 90:10 mixing ratio undergo a significant decrease within a month [32]. To consider this behavior, the manufactured films were stored in a freezer overnight, and the mechanical properties characterization was completed within 24 hrs of the processing time. Figure 2 shows the average tear propagation force obtained by the trouser tear resistance test for the four chosen blown film extruded samples. Upon initial inspection, it is observed that the tear propagation force is higher for the samples in the transverse direction compared with the sample where the slit is in the machine direction. It is commonly known that due to the existing shear forces in the extrusion barrel, polymer molecules tend to align along the length of the barrel to die direction, also known as the machine direction. Hence the polymer molecules are more intertwined in the machine direction than in the transverse direction. This means propagating the tear from a slit created in the structure of the processed film; it requires more force when the slit direction is perpendicular to the machine direction than when it is parallel to it.

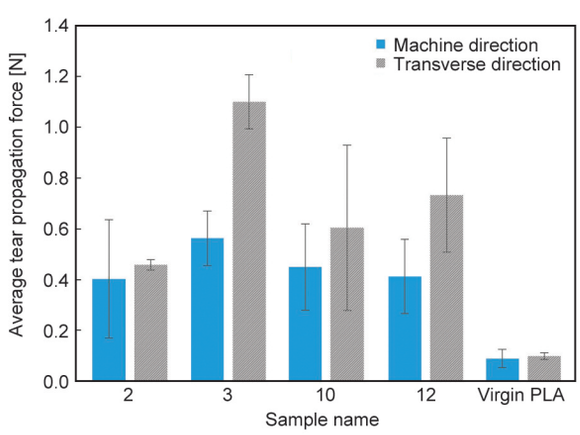

Figure 2. The average tear propagation force obtained by the trouser tear resistance test of blown film extruded samples.

Although in the blown film extrusion process, the bubble stretches the polymer in a transverse direction hence providing molecular orientation in the transverse direction, however, the polymer orientation would depend on both the blow-up ratio (BUR) and draw-down ratio (DDR). The BUR is the ratio of the final diameter of the tube to the diameter of the die, and the DDR is the ratio of the thickness of the extrudates exiting the die, *i.e.*, the die gap to the final film thickness. Table 3 presents the BUR and DDR of the processed films.

The significant tear propagation force difference between Samples 2 and 3 could be attributed to the presence of a joncryl chain extender in Sample 3. The formation of longer PLA and PHBV polymer chains due to chain extension could be associated with the increase of the chance of molecular intertwining, hence increasing the force required to break the intermolecular van der Waals forces via tearing. This effect is also visible in comparison of Samples 10 and 12, where it takes more force to tear Sample 12 (containing a 3% chain extender) in the transverse direction than to tear Sample 10 (containing no chain extender). It also can be seen that all blends have tear propagation force values at least 4.4 and 5.0 times the virgin PLA in the machine direction and transverse direction, respectively. This is a significant improvement to PLA, providing value to the produced films regarding packaging products that require tear propagation forces higher than virgin PLA. The addition of PHBV and plasticizer, specifically, adds to the ductility of PLA, rendering it more tear resistant. Figure 3 presents the obtained yield strength, ultimate tensile strength, and modulus of the films from the uniaxial tensile strength test. It is observed that Sample 2 has a significantly higher (3.6 times higher) modulus than Sample 3, and similarly, Sample 10

Table 3. Properties of the samples related to the blown extrusion process.

Sample name	2	3	10	12
Blow-up ratio (BUR)	2.00	1.50	1.50	1.50
Draw down ratio (DDR)	19.64	10.36	16.83	19.64

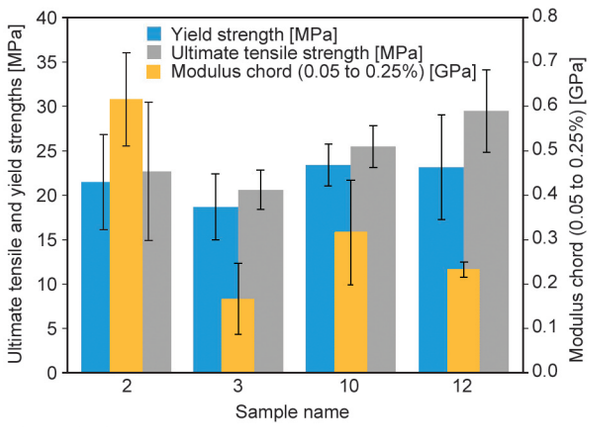

Figure 3. Comparison of the yield strength, ultimate tensile strength, and Young's modulus of the blown extruded film samples.

has a 26% higher modulus than Sample 12. The prominent compositional difference here is that Samples 2 and 10, although at similar PLA:PHBV ratio with Samples 3 and 12, both lack joncryl content in their composition compared to Samples 3 and 12. As established earlier [36], joncryl in addition to extending the chain lengths in most polyesters, when used in a dosage similar to the one used in this research, has a plasticizing effect in the blend as well. This effect increases the ductility of the blends containing joncryl, hence lowering their modulus. The same trend can be identified in the comparison of Sample 2 and Sample 10. In this case, both the triethyl citrate and joncryl content are equal between the two samples, but Sample 10 contains higher PHBV contents than Sample 2. Although both PLA and PHBV are considered brittle polymers, when blended, the addition of PHBV adds ductility. Hence Sample 10, with higher PHBV content, would be more ductile than Sample 2, having a modulus of only 316 MPa. The ultimate tensile strength from Samples 2 to 3 and Samples 10 to 12 decreases, however, this change is not significant, and it could be concluded that all samples have a tensile strength in the range of 20 to 25 MPa, considering the standard deviation range. Sample 12 stands out from all samples, presenting a different set of tensile properties. Although it follows the trend of other samples in modulus, as explained earlier, it has an ultimate tensile strength higher than Sample 10, although it contains triethyl citrate contents. This could be associated either with the synergistic effect between the components or the presence of the chain extender that when the formulation enters the plastic deformation region, it can withstand higher tensile forces compared to Sample 10, which contains no chain extender. The increase in chain length could also be associated with the increase in ultimate tensile strength.

3.2. Barrier properties

3.2.1. Oxygen gas permeability

Permeation of a gas or vapor through a polymer material occurs by the following sequence: absorption of permeant molecules into the surface of the polymer, solubility, and diffusion of the permeant molecules through polymer chains, and desorption from the opposite polymer surface. The difficulty involved in this process is measured and referred to as gas transmission rate, permeation, and permeability by the researchers and the industry. Permeation accounts for the time involved, the effective surface area of the polymer, the pressure the experiment was conducted under, and the volume of permeant passed through the thin film. Permeation is independent of the thickness of the test sample because it is obtained by multiplying the testing film thickness by the gas transmission rate. Hence permeability can be used to compare the barrier performance of different materials given that the testing conditions, such as pressure, relative humidity, and temperature, remain the same. The measured oxygen gas permeability of all samples is presented in Figure 4. The permeability of blown extruded samples was compared with compression molded samples to broaden the comparison. In the sample names, 'A' denotes PLA, 'B' denotes PHBV, and 'J' denotes a joncryl chain extender. For example, the A60-B40 sample has a PLA:PHBV ratio of 60:40 percent, and 49.5A-49.5B-J1 has 49.5% PLA, 49.5% PHBV and 1% joncryl chain extender (hence 0% plasticizer). Pure PHBV could not be blown to film due to its low melt strength; hence it was only compression molded. On the blown film extruded samples, Samples 3 and 12 show higher permeation values compared to Samples 2 and 10, denoting the adverse effect of the joncryl chain extender on oxygen gas permeation through the blend formulation compared to samples without chain extender contents. This effect is seen once again in comparison of Sample A50-B50 with A49.5-B49.5-J1, where the latter has 2.6 times an inferior barrier. One reason to explain this effect could be that the amount of joncryl that was not reacted with terminal hydroxyl groups in polymer (excess joncryl content), which act as a plasticizer, facilitate the passage of oxygen molecules through the created spaces between the

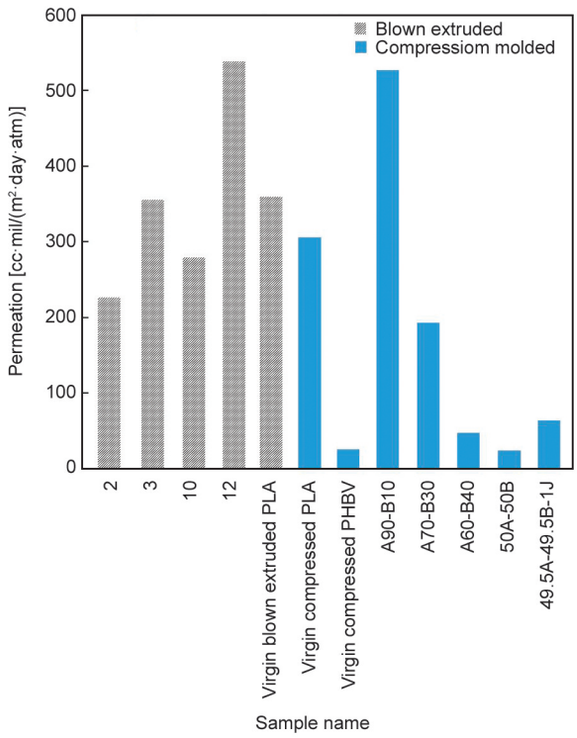

Figure 4. Oxygen gas permeability of blown film extruded samples in comparison with compression molded samples.

polymer chain. Some studies pointed out the deterioration of oxygen barrier performance by incorporating joncryl due to a possible less perfect arrangement of new crystal structures from branching or crosslinking chain structures and hence a lower crystallinity of the compound [40].

The oxygen permeation of blown extruded pure PLA (395.6 cc·mil/(m^2·day)) is higher than but relatively close to the compression molded pure PLA (305.7 cc·mil/(m^2·day)). This is expected as PLA polymer molecules in compression molding experience a longer (roughly 4 min compared to 8 s) cooling time to arrange and form crystals compared to almost instant cooling in blown film extrusion. This takes to account that PLA is a semi-crystalline polymer. It also provides a good basis for comparing the permeability of different samples. For instance, in blown extruded samples, although it was expected to observe a permeability decrease from Sample 2 to Sample 10 because Sample 10 has a higher PHBV content, the permeability increases. But in compression molded samples, oxygen permeability decreases with the increase of PHBV. For example, permeation in Samples A70-B30, A60-B40, and A50-B50 is 192.7, 47.4, and 24.3 cc·mil/(m^2·day), respectively.

One comparison that comes as a key to resolving the contrasting results from the effect of the increase of PHBV content on the permeability of the blend is the comparison of the A90-B10 sample vs the compression molded pure PLA. Here, with the addition of 10% PHBV with a measured oxygen permeability equal to 8% of PLA (25.4 cc·mil/(m^2·day)) with PLA, the oxygen permeability of PLA increases by 72%. This comes hand in hand with the premise of this study which was based on the synergistic effect of PLA/PHBV blend when the PHBV content is at around 10 to 30%. This synergistic effect is identified in the elongation at break in other studies [32, 40].

3.2.2. Water vapor permeability

The water vapor permeation (*WVP*) of manufactured films is presented in Figure 5. The water permeability of PLA at 23 °C and 85% relative humidity is reported in the literature between 63–342 g·mil/(m^2·day·kPa) [1, 21, 24] while we found it at 393 g·mil/(m^2·day·kPa). This value is slightly higher than the highest reported value in the literature. However, there are two main differences between this and the reported values. First, this test was conducted in standard condition (*RH* at 50%, which is lower than the reported 85%). The permeability coefficients of PLA are reported to decrease with the increase in moisture content [41]. Second, the films were blown extruded rather than melt cast or calendered. It is more plausible that blown extrusion could reduce the barrier properties of the films. Alternatively, pure PLA film is very crinkly, so when the bubble is formed and the tube is narrowed down and folded by the take-up nips, many creases are made on the surface of the film. The creases could be potential failure points that may lead to increased water vapor permeation of a blown extruded brittle film compared to a non-creased melt casted film.

Samples 2 and 10 show the lowest, and Samples 3 and 12 show the highest permeability values. The presence of trace joncryl contents in Samples 3 and 12 clearly indicates that the presence of a joncryl chain extender is the only reason for the significant increase in the water vapor permeability of the films, regardless of the PLA/PHBV ratio. This behavior could be attributed to the increased molecular polarity of the blends containing chain extenders. Furthermore, joncryl is a multifunctional compound containing an epoxy functional group. This can facilitate the formation of secondary hydrogen bonding between

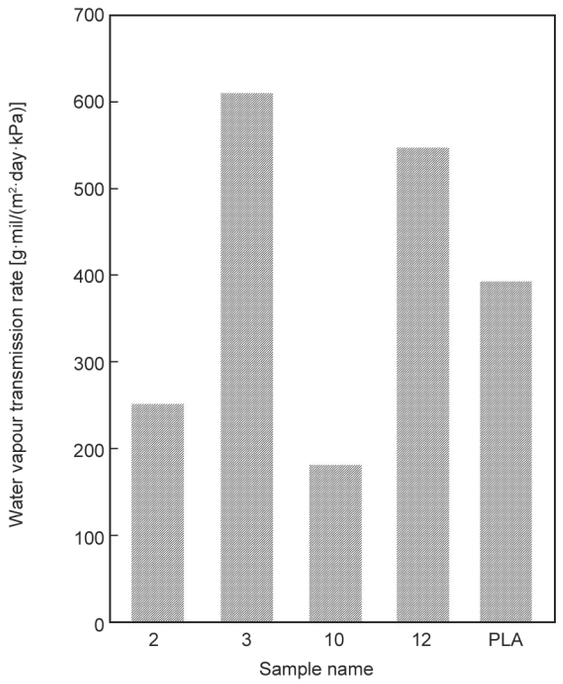

Figure 5. Water vapor transmission rate of blown film extruded samples, equilibrium over a two-month period.

the surface of the films and the water vapor molecules, leading to faster absorption of water vapor particles and an increased *WVP* value. In total, the addition of 3 wt% chain extender increased the *WVP* of Sample 2 by 142% and Sample 3 by 203%.

By comparing Sample 2 with 10 and Sample 3 with 12, it can be deduced that the increase of PHBV content improved the water vapor transmission rate of Sample 2 by 38% and Sample 3 by 11%. It can be seen again that the effect of the chain extender with the epoxy functional group is dominant compared to the effect of the increase of PHBV content in reducing the *WVP* when comparing the proportion of reduced *WVP* between Samples 2 and 10 and with Sample 3 and 12. By observing the *WVP* value of pure PLA film that was blown extruded with the very same processing condition as the other four samples, it can be concluded that the addition of PHBV can significantly improve the *WVP* of the PLA up to 55% (PHBV being added 27%). However, pure PLA would still be a higher barrier to water vapor than a PLA-PHBV blend containing an epoxy group containing a chain extender. It would, however, be interesting to see whether the same applies if a PLA-PHBV blend would have less chain extender content, for instance, up to only 0.3%.

3.3. Texture and haze

All the samples were manufactured at the same processing conditions; however, as each had a different material composition, the texture, and haze of each sample were different from one another (Figure 6). To indicate the texture and haze difference, samples were placed in front of the same background scene tion made to the background image was used as a reference to texture and haze differences between samples. It was observed in the bubble formation in the processing stage and can be seen in Samples 3 and 12 that the blends leave a pronounced track in the machine direction. This track for Samples 3 and 12 is quite wavy, especially in Sample 12, where this effect is even more pronounced. However, this effect in Sample 11 is not wavy but straight and much more subdued. The waviness of the polymer track line in the machine direction could be associated with the presence of a chain extender in the blend composition.

The presence of a chain extender in the blends containing PLA and PHBV polyesters leads to an improvement in melt strength. Although the melt strength was not measured in this study, with the respect that each batch contains a different content of PLA, PHBV, and joncryl chain extender, it is expected that each formulation has a different melt strength. This means that to provide the best texture and minimize the track line of polymers in the machine direction, each batch could be processed at slightly different processing conditions. This includes tweaking the process temperature and screw speed and adjusting the air pressure inside the bubble, and spinning the speed of take-up nips. Being said, all the films in this study were processed at the exact same processing conditions.

4. Conclusions

In conclusion, twelve different blends of PLA/PHBV with the addition of plasticizers and chain extenders were investigated. Only four blends were suitable for blown film extrusion, and these four were chosen to provide a diverse range of compositional contents for further analysis. The tear propagation force was found to be higher in the transverse direction, which was attributed to the molecular orientation of the polymers in the extrusion process. Adding PHBV and plasticizers improved the films' tear resistance

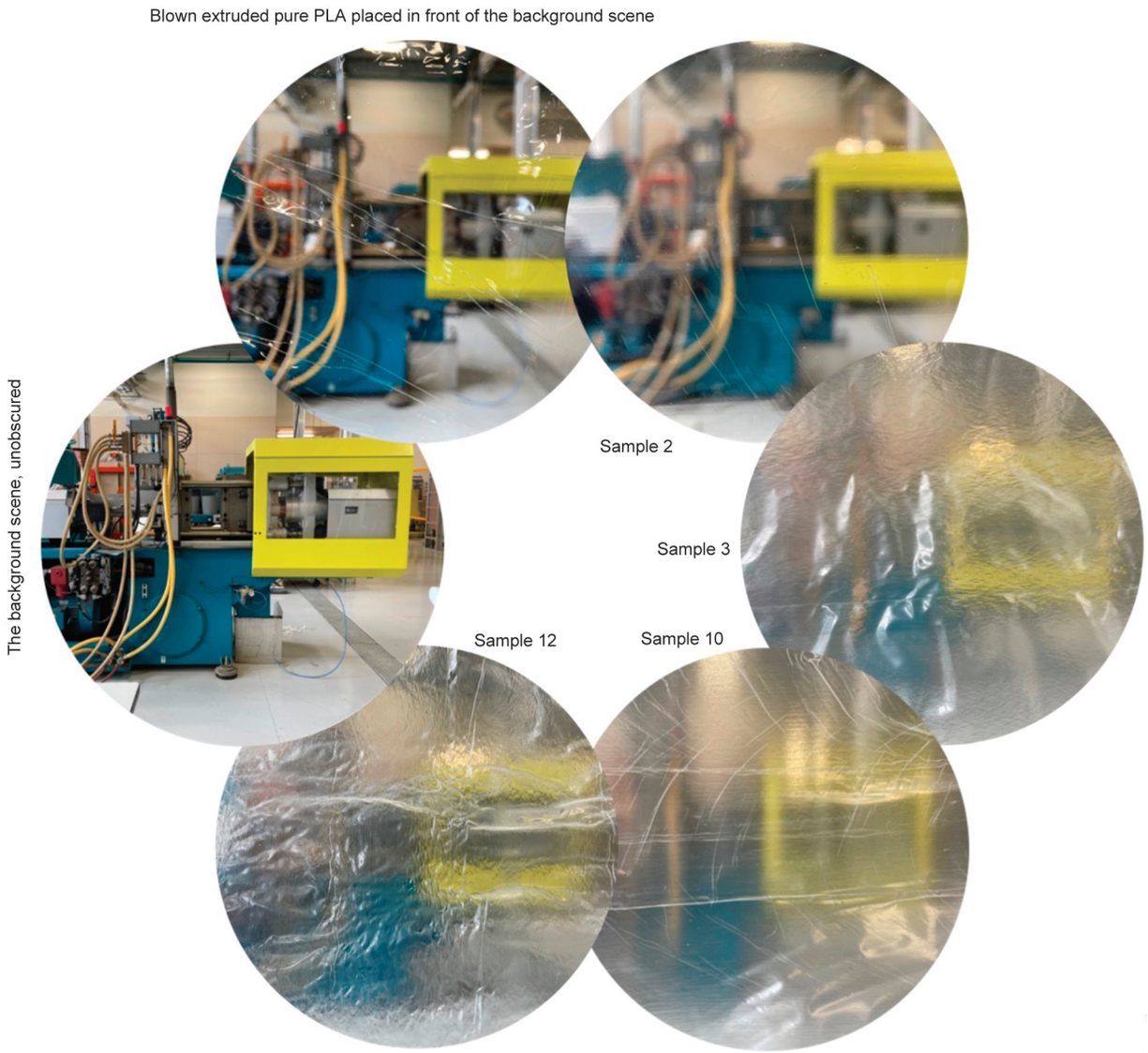

Figure 6. Image of the same background taken through the samples to reflect the texture and haze of the blown extruded films. [The blur effect is due to film opacity and not lens focus. The camera remained focused on the films for all samples.]

compared to virgin PLA, making them suitable for packaging products that require higher tear propagation forces. The modulus of the films was found to be influenced by the compositional content, and the addition of a chain extender and plasticizer reduced the modulus of the films. The ultimate tensile strength of the films was found to be in the range of 20 to 25 MPa, with Sample 12 standing out for having a higher ultimate tensile strength. Overall, this study provides valuable insights into the mechanical properties of PLA/PHBV blends and their potential applications in the packaging industry.

Acknowledgements

The authors acknowledge the financial support provided by Callaghan Innovation (a Crown Research entity) in New Zealand for the entirety of this research project.

References

[1] Wu F., Misra M., Mohanty A. K.: Challenges and new opportunities on barrier performance of biodegradable polymers for sustainable packaging. Progress in Polymer Science, **117**, 101395 (2021). https://doi.org/10.1016/j.progpolymsci.2021.101395

[2] Tambawala H., Batra S., Shirapure Y., More A. P.: Curcumin- a bio-based precursor for smart and active food packaging systems: A review. Journal of Polymers and the Environment, **30**, 2177–2208 (2022). https://doi.org/10.1007/s10924-022-02372-x

[3] Drieskens M., Peeters R., Mullens J., Franco D., Lemstra P. J., Hristova-Bogaerds D. G.: Structure *versus* properties relationship of poly(lactic acid). I. Effect of crystallinity on barrier properties. Journal of Polymer Science Part B: Polymer Physics, **47**, 2247–2258 (2009). https://doi.org/10.1002/polb.21822

[4] Öz A. T., Süfer Ö., Çelebi Sezer Y.: Poly(lactic acid) films in food packaging systems. Food Science & Nutrition Technology, **2**, 131 (2017). https://doi.org/10.23880/fsnt-16000131

[5] Rhim J-W., Hong S-I., Ha C-S.: Tensile, water vapor barrier and antimicrobial properties of PLA/nanoclay composite films. LWT-Food Science and Technology, **42**, 612–617 (2009). https://doi.org/10.1016/j.lwt.2008.02.015

[6] Auras R., Harte B., Selke S.: An overview of polylactides as packaging materials. Macromolecular Bioscience, **4**, 835–864 (2004). https://doi.org/10.1002/mabi.200400043

[7] Koller M., Salerno A., Tuffner P., Koinigg M., Böchzelt H., Schoberd S., Pieber S., Schnitzer H., Mittelbach M., Braunegg G.: Characteristics and potential of micro algal cultivation strategies: A review. Journal of Cleaner Production, **37**, 377–388 (2012). https://doi.org/10.1016/j.jclepro.2012.07.044

[8] Mendhulkar V. D., Shetye L. A.: Synthesis of biodegradable polymer polyhydroxyalkanoate (PHA) in cyanobacteria *Synechococcus elongates* under mixotrophic nitrogen- and phosphate-mediated stress conditions. Industrial Biotechnology, **13**, 85–93 (2017). https://doi.org/10.1089/ind.2016.0021

[9] Singh A. K., Sharma L., Mallick N., Mala J.: Progress and challenges in producing polyhydroxyalkanoate biopolymers from cyanobacteria. Journal of Applied Phycology, **29**, 1213–1232 (2017). https://doi.org/10.1007/s10811-016-1006-1

[10] Ausejo J. G., Rydz J., Musioł M., Sikorska W., Sobota M., Włodarczyk J., Adamus G., Janeczek H., Kwiecień I., Hercog A., Johnston B., Khan H. R., Kannappan V., Jones K. R., Morris M. R., Jiang G. Z., Radecka I., Kowalczuk M.: A comparative study of three-dimensional printing directions: The degradation and toxicological profile of a PLA/PHA blend. Polymer Degradation and Stability, **152**, 191–207 (2018). https://doi.org/10.1016/j.polymdegradstab.2018.04.024

[11] Burzic I., Pretschuh C., Kaineder D., Eder G., Smilek J., Másilko J., Kateryna W.: Impact modification of PLA using biobased biodegradable PHA biopolymers. European Polymer Journal, **114**, 32–38 (2019). https://doi.org/10.1016/j.eurpolymj.2019.01.060

[12] Ecker J. V., Burzic I., Haider A., Hild S., Rennhofer H.: Improving the impact strength of PLA and its blends with PHA in fused layer modelling. Polymer Testing, **78**, 105929 (2019). https://doi.org/10.1016/j.polymertesting.2019.105929

[13] Plavec R., Hlaváčiková S., Omaníková L., Feranc J., Vanovčanová Z., Tomanová K., Bočkaj J., Kruželák J., Medlenová E., Galisová I., Danišová L., Přikryl R., Figalla S., Melčová V., Alexy P.: Recycling possibilities of bioplastics based on PLA/PHB blends. Polymer Testing, **92**, 106–880 (2020). https://doi.org/10.1016/j.polymertesting.2020.106880

[14] Szuman K., Krucińska I., Boguń M., Draczyński Z.: PLA/PHA-biodegradable blends for pneumothermic fabrication of nonwovens. Autex Research Journal, **16**, 119–127 (2016). https://doi.org/10.1515/aut-2015-0047

[15] Weng Y-X., Wang L., Zhang M., Wang X-L., Wang Y-Z.: Biodegradation behavior of P(3HB,4HB)/PLA blends in real soil environments. Polymer Testing, **32**, 60–70 (2013). https://doi.org/10.1016/j.polymertesting.2012.09.014

[16] Zhao H., Cui Z., Wang X., Turng L-S., Peng X.: Processing and characterization of solid and microcellular poly(lactic acid)/polyhydroxybutyrate-valerate (PLA/PHBV) blends and PLA/PHBV/clay nanocomposites. Composites Part B: Engineering, **51**, 79–91 (2013). https://doi.org/10.1016/j.compositesb.2013.02.034

[17] Ibrahim N. I., Shahar F. S., Sultan M. T. H., Shah A. U. M., Safri S. N. A., Yazik M. H. M.: Overview of bioplastic introduction and its applications in product packaging. Coatings, **11**, 14–15 (2021). https://doi.org/10.3390/coatings11111423

[18] Bugnicourt E., Cinelli P., Lazzeri A., Alvarez V.: Polyhydroxyalkanoate (PHA): Review of synthesis, characteristics, processing and potential applications in packaging. Express Polymer Letters, **8**, 791–808 (2014). https://doi.org/10.3144/expresspolymlett.2014.82

[19] Ncube L. K., Ude A. U., Ogunmuyiwa E. N., Zulkifli R., Beas I. N.: Environmental impact of food packaging materials: A review of contemporary development from conventional plastics to polylactic acid based materials. Materials, **13**, 4994 (2020). https://doi.org/10.3390/ma13214994

[20] Zhao X., Cornish K., Vodovotz Y.: Narrowing the gap for bioplastic use in food packaging: An update. Environtal Science & Technology, **54**, 4712–4732 (2020). https://doi.org/10.1021/acs.est.9b03755

[21] Auras R. A., Harte B., Selke S., Hernandez R.: Mechanical, physical, and barrier properties of poly(lactide) films. Journal of Plastic Film and Sheeting, **19**, 123–135 (2003). https://doi.org/10.1177/8756087903039702

[22] Jost V., Langowski H. C.: Effect of different plasticisers on the mechanical and barrier properties of extruded cast PHBV films. European Polymer Journal, **68**, 302–312 (2015). https://doi.org/10.1016/j.eurpolymj.2015.04.012

[23] Crétois R., Follain N., Dargent E., Soulestin J., Bourbigot S., Marais S., Lebrun L.: Microstructure and barrier properties of PHBV/organoclays bionanocomposites. Journal of Membrane Science, **467**, 56–66 (2014). https://doi.org/10.1016/j.memsci.2014.05.015

[24] Fabra M. J., Lopez-Rubio A., Lagaron J. M.: Nanostructured interlayers of zein to improve the barrier properties of high barrier polyhydroxyalkanoates and other polyesters. Journal of Food Engineering, **127**, 1–9 (2014).
https://doi.org/10.1016/j.jfoodeng.2013.11.022

[25] Siracusa V., Rocculi P., Romani S., Dalla Rosa M.: Biodegradable polymers for food packaging: A review. Trends in Food Science & Technology, **19**, 634–643 (2008).
https://doi.org/10.1016/j.tifs.2008.07.003

[26] El-Hadi A. M.: Increase the elongation at break of poly (lactic acid) composites for use in food packaging films. Scientific Reports, **7**, 46767 (2017).
https://doi.org/10.1038/srep46767

[27] Arrieta M. P., Samper M. D., López J., Jiménez A.: Combined effect of poly(hydroxybutyrate) and plasticizers on polylactic acid properties for film intended for food packaging. Journal of Polymers and the Environment, **22**, 460–470 (2014).
https://doi.org/10.1007/s10924-014-0654-y

[28] Hernandez-Garcia E., Vargas M., Chiralt A., Gonzalez-Martinez C.: Biodegradation of PLA-PHBV blend films as affected by the incorporation of different phenolic acids. Foods, **11**, 243 (2022).
https://doi.org/10.3390/foods11020243

[29] Armentano I., Fortunati E., Burgos N., Dominici F., Luzi F., Fiori S., Jiménez A., Yoon K., Ahn J., Kang S., Kenny J. M.: Bio-based PLA_PHB plasticized blend films: Processing and structural characterization. LWT-Food Science and Technology, **64**, 980–988 (2015).
https://doi.org/10.1016/j.lwt.2015.06.032

[30] Guinault A., Dutarte G., Boufarguine M., Miquelard-Garnier G., Sollogoub C.: Morphology-crystallinity relationship in PLA-PHBV blends prepared *via* extrusion. Key Engineering Materials, **554**, 1707–1714 (2013).
https://doi.org/10.4028/www.scientific.net/KEM.554-557.1707

[31] Pietrosanto A., Scarfato P., Di Maio L., Incarnato L.: Development of PLA /PHB blown films with improved performance for food packaging applications. Chemical Engineering Transactions, **87**, 91–96 (2021).
https://doi.org/10.3303/CET2187016

[32] Gerard T., Budtova T., Podshivalov A., Bronnikov S.: Polylactide/poly(hydroxybutyrate-*co*-hydroxyvalerate) blends: Morphology and mechanical properties. Express Polymer Letters, **8**, 609–617 (2014).
https://doi.org/10.3144/expresspolymlett.2014.64

[33] Han L., Han C., Zhang H., Chen S., Dong L.: Morphology and properties of biodegradable and biosourced polylactide blends with poly(3-hydroxybutyrate-*co*-4-hydroxybutyrate). Polymer Composites, **33**, 850–859 (2012).
https://doi.org/10.1002/pc.22213

[34] Li L., Huang W., Wang B., Wei W., Gu Q., Chen P.: Properties and structure of polylactide/poly(3-hydroxybutyrate-*co*-3-hydroxyvalerate) (PLA/PHBV) blend fibers. Polymer, **68**, 183–194 (2015).
https://doi.org/10.1016/j.polymer.2015.05.024

[35] Liu Q., Wu C., Zhang H., Deng B.: Blends of polylactide and poly(3-hydroxybutyrate-*co*-3-hydroxyvalerate) with low content of hydroxyvalerate unit: Morphology, structure, and property. Journal of Applied Polymer Science, **132**, 426–489 (2015).
https://doi.org/10.1002/app.42689

[36] Pouriman H., Lin R., Graham K., Jayaraman K.: Mechanical, thermal and rheological investigation of poly (lactic acid) (PLA)/poly(3-hydroxybutyrate-*co*-hydroxyvalerate) (PHBV) blend within its synergistic elongation effect region. Express Polymer Letters, **17**, 373–389 (2023).
https://doi.org/10.3144/expresspolymlett.2023.27

[37] Cantor K.: Blown film extrusion. Hanser, Cincinnati (2018).

[38] Naser A. Z., Deiab I., Darras B. M.: Poly(lactic acid) (PLA) and polyhydroxyalkanoates (PHAs), green alternatives to petroleum-based plastics: A review. Royal Society of Chemistry, **11**, 17151–17196 (2021).
https://doi.org/10.1039/D1RA02390J

[39] Baharu M. N., Kadhum A. A. H., Al-Amiery A. A., Mohamad A. B.: Synthesis and characterization of polyesters derived from glycerol, azelaic acid, and succinic acid. Green Chemistry Letters and Reviews, **8**, 31–38 (2015).
https://doi.org/10.1080/17518253.2014.991810

[40] Flodberg G., Helland I., Thomsson L., Fredriksen S. B.: Barrier properties of polypropylene carbonate and poly(lactic acid) cast films. European Polymer Journal, **63**, 217–226 (2015).
https://doi.org/10.1016/j.eurpolymj.2014.12.020

[41] Auras R., Harte B., Selke S.: Effect of water on the oxygen barrier properties of poly(ethylene terephthalate) and polylactide films. Journal of Applied Polymer Science, **92**, 1790–1803 (2004).
https://doi.org/10.1002/app.20148

Express Polymer Letters Vol.17, No.10 (2023) 1019–1030
Available online at www.expresspolymlett.com
https://doi.org/10.3144/expresspolymlett.2023.76

Research article

Introducing metal-ligand coordination interaction for self-healing and recyclable nitrile–butadiene rubber: A facile strategy

Yuan Gao[1], *Weiran Zhang*[1], *Junhao Wang*[2], *Zishuo Wang*[1], *Zhaobo Wang*[1*]

[1]College of Material Science & Engineering, Qingdao University of Science & Technology, 266042 Qingdao, P. R. China
[2]School of Mechanical, Electrical & Information Engineering, SHANDONG UNIVERSITY, WEIHAI, 264209 Weihai, P. R. China

Received 21 April 2023; accepted in revised form 1 July 2023

Abstract. In this research, a nitrile-butadiene rubber (NBR) was prepared with excellent mechanical, self-healing and recycling properties by introducing metal-ligand coordination interaction. A coordination crosslinking network based on ligand bonding was successfully introduced in the NBR matrix by mechanical compounding. The dynamic reversibility of the coordination crosslinking network not only provides the vulcanizate with excellent mechanical properties but also confers a remarkable self-healing ability under high temperatures and recyclable property under mechanical shear, respectively. The sample, which was subjected to the complete cut, could be capable of restoring its original tensile strength after self-healing treatment. The self-healing efficiency of NBR vulcanizate is significantly dependent on the self-healing temperature and time, which can surprisingly reach 97% of the original tensile strength after self-healing treatment at 180 °C for 60 min. After the mechanical shear, the coordination crosslinking network is reversibly transformed. The tensile strength of the NBR vulcanizates after mechanical shearing recycling and re-vulcanization was similar to that of the original NBR vulcanizates. This research presents a novel approach to enhance the durability of rubber used in commercial applications, endowing it with reshaping and recycling capabilities and mitigating environmental issues associated with waste rubber.

Keywords: *self-healing, coordination, rubber, recycling, mechanical properties*

1. Introduction

Self-healing is one of the most intriguing phenomena in nature. Most organisms could self-heal themselves when they suffer damage. Since White *et al*. [1] first reported the self-healing polymers in 2001, many scholars have attempted to introduce this brilliant and biological concept into synthetic materials. In the last decade, a series of self-healing polymers have been emerged [2–4], which can repair their own damage spontaneously in response to light, heat, or other stimuli. Usually, self-healing polymers can be classified into two distinct categories: extrinsic and intrinsic self-healing materials. Due to the simpler preparation process and the ability to achieve repeated healing, intrinsic self-healing materials are more desirable to researchers. A common approach for constructing intrinsic self-healing materials is to introduce reversible bonds, such as Diels-Alder bonds [5, 6], disulfide bonds [7], hydrogen bonds [8], ionic interactions [3, 9] and metal-ligand coordination [10, 11], *etc*. These dynamic reversible bonds make it feasible to self-heal the broken bonds. Moreover, polymers based on reversible bonds have better chain mobility since the reversible bonds are less restrictive to the polymer crosslinking network, which is also essential for self-healing [9].

*Corresponding author, e-mail: wangzhb@qust.edu.cn
© BME-PT

Rubber, as a superior polymer material with a history of application, can be traced back to a century ago. With its unique high elasticity and remarkable mechanical properties, rubber has an irreplaceable wide range of applications in medical materials [12], aerospace [13], automotive industry [14] and other fields. However, during the service, rubber is prone to cracking under stress, light, and heat, resulting in a gradual loss of mechanical properties [15, 16]. In order to improve the strength and rebounded resilience of rubber products, crosslinking is necessary. Unfortunately, the vulcanizates, crosslinked in the traditional way, are difficult to recycle, which could cause serious pollution [17]. However, these methods are complex and ineffective, while the deterioration in the mechanical properties of the recycled product is inevitable [18, 19]. Self-healing materials are a promising solution to improve material sustainability and prolong the lifetime [20, 21]. By constructing the reversible supramolecular networks, rubber is expected to exhibit self-healing and recyclable properties. Nevertheless, rubbers based on reversible supramolecular crosslinking networks often have weak mechanical properties due to relatively weak non-covalent interactions [4]. In order to address this challenge, Liu *et al*. [22] achieved high strength and stability by constructing the ionic-covalent crosslinking networks while failing to consider the mechanical and self-healing properties effectively. Therefore, it is expected to prepare a rubber with excellent mechanical and self-healing properties simultaneously by introducing the coordination interactions to form the metal-ligand crosslinking networks, which have the highest bond energy among the non-covalent interactions. Based on the above-mentioned, commercial nitrile–butadiene rubber (NBR) seems to be an ideal choice for rubber with self-healing and recyclable properties. The cyano groups in NBR could react with various transition metal ions to form a metal-ligand crosslinking network effectively [23, 24]. The dynamic reversible behavior in the metal-ligand crosslinking networks can endow rubber with the self-healing and recyclable features [25].

In this research, a simple strategy was utilized to prepare the self-healing and recyclable NBR. The strategy is based on the formation of a metal-ligand crosslinking network between the cyano group and metal ions. With the reversible dynamic crosslinking network, the NBR vulcanizate with excellent self-healing and recyclable properties could be achieved successfully.

2. Experimental

2.1. Materials

Nitrile–butadiene rubber (NBR, 4155 type, 41 wt% acrylonitrile content and ML_{1+4}[100 °C] = 55±5) was used in present research and obtained from Nantex Industry Co. Ltd. (Zhenjiang, China). Cupric sulfate anhydrous ($CuSO_4$, AR) was procured from Reagent Chemical Co. Ltd. (Tianjin, China). Dioctyl phthalate (DOP) plasticizer was sourced from Guangcheng Chemical Industry Co. Ltd. (Tianjin, China).

2.2. Sample preparation

The NBR was initially mixed with DOP in a two-roll mill (X[S] K-160, Qun Yi Rubber Machinery Co. Ltd., Shanghai, China) for 5 min at room temperature. Subsequently, $CuSO_4$ powder was introduced into NBR and the blending process proceeded for another 5 min to ensure the uniform dispersion of DOP and $CuSO_4$ particles in the NBR matrix. The resulting mixture was subjected to compression molding at 180 °C for 60 min using a plate vulcanizing machine (50 T, Qun Yi Rubber Machinery Co. Ltd., Shanghai, China) and the series NBR/$CuSO_4$/DOP vulcanizates with coordination crosslinking induced by metal-ligand interactions was prepared. The above NBR vulcanizates were formed into 2 mm thick sheets.

For the convenience of narration, the vulcanizates were designated according to their NBR/$CuSO_4$/DOP composition. For instance, NCu10-D10 was used to refer to the NBR/$CuSO_4$/DOP (100/10/10) vulcanizate. The specific compositions of the NBR/$CuSO_4$/DOP vulcanizates are summarized in Table 1. For illustrating purposes, the unvulcanized NCu10-D10 blend was noted as NCu10-D10a and the vulcanized NCu10-D10 vulcanizate was noted as NCu10-D10b.

2.3. Characterization

The curing behavior of the NBR/$CuSO_4$/DOP vulcanizates was investigated using a Rotorless Rheometer (KY-6002, Kai Yuan Machinery Co. Ltd., China)

Table 1. Ingredients [phr] of NBR/$CuSO_4$/DOP vulcanizates.

Sample	NCu3-D10	NCu5-D10	NCu10-D10	NCu20-D10
NBR	100	10	100	100
$CuSO_4$	3	5	10	20
DOP	10	10	10	10

at a constant temperature of 180 °C and a vibrating angle of ±1°.

The glass transition temperature (T_g) of the samples was investigated using a differential scanning calorimeter (DSC 204 F1, NETZSCH Instruments, Germany) under a nitrogen atmosphere. The samples were heated at a rate of 10 K/min from –60 to 70 °C to determine their T_g values.

X-ray photoelectron spectra (XPS) survey scans were analyzed by an EscalabTM 250Xi X-ray photoelectron spectrometer (Thermo Fisher Scientific, USA). The chemical components related to nitrogen in NBR/$CuSO_4$/DOP vulcanizates were analyzed to examine their chemical species.

The mechanical properties of NBR/$CuSO_4$/DOP vulcanizates were evaluated using a universal material testing machine (TCS-2000, GoTech Testing Machines Inc., China) at room temperature, with a crosshead speed of 500 mm·min^{-1}. Each sample was tested a minimum of three times to ensure precision and reproducibility.

For the self-healing test, an original dumbbell-shaped sample was cut into two separate pieces using a clean razor blade. The cutting surfaces were aligned and adjoined immediately with minimal pressure. Subsequently, the healed samples were subjected to the healing treatment at the predetermined temperature for a certain time without loading. After healing, the mechanical properties were assessed through stress-strain testing. The healing efficiency was calculated as the ratio of the tensile strength of the healed sample to that of the original one.

The morphology of NBR/$CuSO_4$/DOP vulcanizates was investigated by the utilization of field-emission scanning electron microscopy (FE-SEM, JSM-6700F, Japan Electron Optics Laboratory Co., Ltd., Japan). Prior to analysis, the surfaces of the samples were sputter-coated with a thin layer of platinum coating to prevent electrostatic accumulation.

Tensile stress relaxation experiments were conducted using a high-temperature and low-temperature servo-controlled tensile testing machine (AI-7000S, GoTech Testing Machines Inc., China) at room temperature (*RT*), 60, 120 and 180 °C, respectively. The sample were subjected to a strain of 100% at a constant crosshead speed of 100 mm·min^{-1}. The sample were tested after a 5 min incubation period, and the relaxation time was set at 5 min.

Equilibrium swelling experiments were conducted to ascertain the crosslinking density of the NBR/$CuSO_4$/DOP vulcanizates. Initially, the samples were submerged in dichloromethane (DCM) for a period of 7 days to attain the swelling equilibrium. Then the surface of the swollen samples was gently blotted using the dust-free filter paper to remove any residual DCM, and the samples were subsequently weighed. Finally, the swollen samples were dried at 60 °C for a duration of 12 hours until a constant weight was achieved. The crosslinking density of samples was computed by the Flory-Rehner equation as shown as Equation (1) [26]:

$$V = -\frac{\ln(1-V_0) + V_0 + \chi V_0^2}{V_1\left(V_0^{1/3} - \frac{V_0}{2}\right)} \quad (1)$$

where V_0 is given by Equation (2):

$$V_0 = \frac{\frac{m_2}{\rho_2}}{\frac{m_2}{\rho_2} + \frac{m_1 - m_2}{\rho_1}} \quad (2)$$

The crosslinking density (V) of the samples was calculated using the formula above, where V_1 represented the molar volume of dichloromethane (DCM) at 67.8 cm^3·mol^{-1}, χ was the NBR-DCM interaction parameter at 0.33, ρ_1 and ρ_2 were the densities of DCM and NBR at 1.325 and 0.98 g·cm^{-3}, respectively. The mass of the swollen sample before and after drying was represented as m_1 and m_2, respectively.

3. Results and discussion

3.1. Curing characteristics and coordination crosslinking behaviors of NBR/$CuSO_4$/DOP vulcanizates

In our research, a distinctive characteristic of self-healing rubber is the formation of a coordination crosslinking network through the reversible coordination bonds, which is achieved by utilizing the metal-ligand interaction of cyano in NBR with $CuSO_4$. A schematic illustration of this process is presented in Figure 1. Our previous work has demonstrated that the unmodified commercial NBR can engage in coordination interactions with metal salts to establish a stable coordination crosslinking network [27]. This strategy ensures the formation of supramolecular networks in NBR/$CuSO_4$/DOP compounds based on dynamic bonds.

Under the stimulation of heat treatment, the cyano group in NBR will react with the copper ion in $CuSO_4$ by coordination effectively. During the vulcanization, the chain mobility of the NBR is decreased obviously due to the implication of metal-ligand interactions, which can be derived from the analysis of

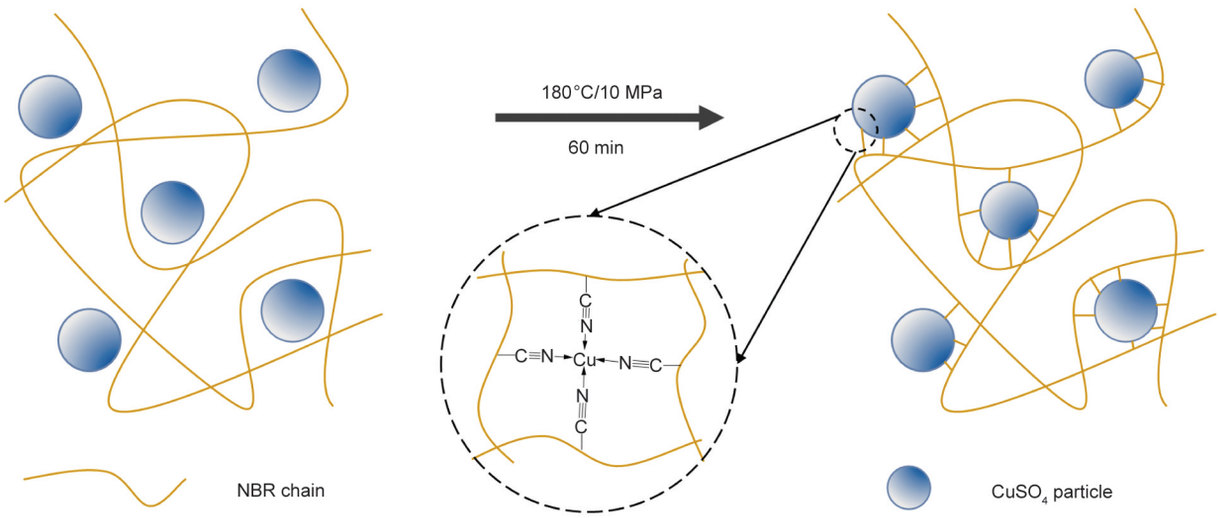

Figure 1. Diagrammatical illustration of the coordination crosslinking structure in NBR vulcanizate.

curing curves as shown in Figure 2. As seen in the figure, the series NBR/$CuSO_4$/ DOP compounds with different $CuSO_4$ dosages at 180 °C. The torque of the compounds was increased with increasing curing time, resulting from the formation of the coordination crosslinking networks induced by the interaction between the cyano group and Cu^{2+}. Moreover, the torque was also increased with increasing $CuSO_4$ dosage, which could attribute to the increasing crosslinking density.

The glass transition temperature (T_g) is a useful indicator of the mobility of macromolecular segments. Comparing the T_g values of the NBR/$CuSO_4$/DOP blend with that of the vulcanizates, it is possible to identify the occurrence of crosslinking within the NBR/$CuSO_4$/DOP vulcanizates. The T_g of the series NBR/$CuSO_4$/DOP blend and the vulcanizates were measured by DSC. The DSC curves are displayed in Figure 3. It is evident that the T_g of the series of the pure NBR and NBR/$CuSO_4$/DOP blend did not show significant changes in T_g of the series (–22.1 and –21.6 °C), indicating that the simple blending of $CuSO_4$ with NBR did not result in the considerable crosslinking between Cu^{2+} and a cyano group. However, after vulcanization, the T_g of the series value of NCu10-D10 increased significantly from –21.6 to –15.1 °C, indicating the formation of a coordination crosslinking network through the strong coordination effect of Cu^{2+} and cyano group. The crosslinking network greatly restricted the mobility of NBR chain segments greatly, resulting in significantly increasing T_g of the series values. Moreover, the T_g of the series values of the NBR/$CuSO_4$/DOP vulcanizates were increased with the increasing $CuSO_4$ dosage, indicating that the higher the $CuSO_4$ content led to the higher the crosslinking density, which

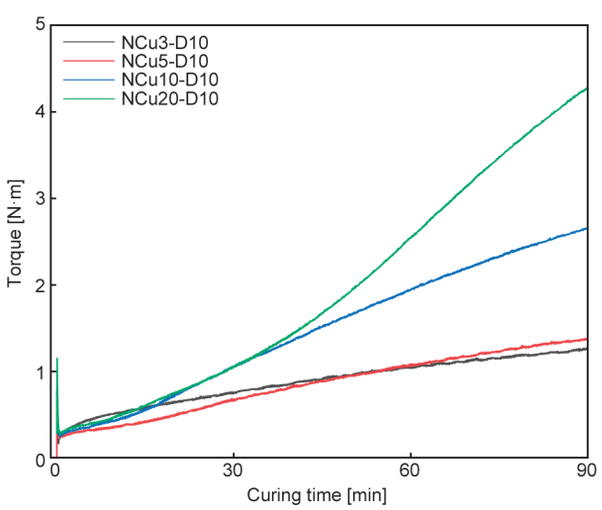

Figure 2. Curing curves of NBR/$CuSO_4$/DOP compounds with different $CuSO_4$ dosage at 180 °C.

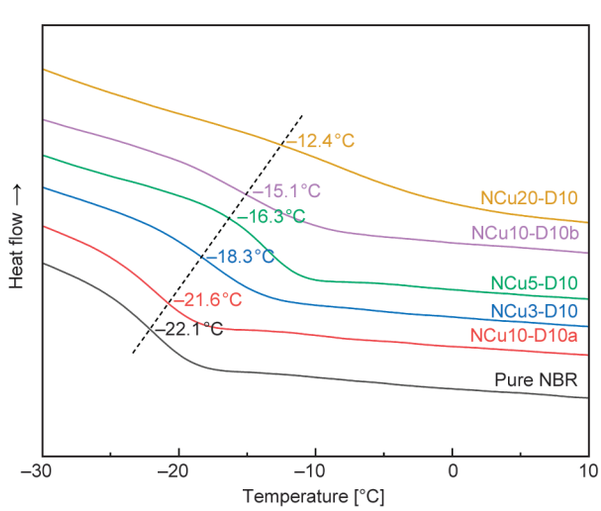

Figure 3. DSC curves of NBR/$CuSO_4$/DOP blend and vulcanizates.

resulted in the strongly restricted movement of NBR chain segments.

XPS could identify the chemical environments of elements by detecting their characteristic binding energies. Coordination structures, such as those formed between metal ions and ligands, can significantly alter the chemical environment of the central and ligand atoms. In this research, the N 1s XPS spectra of NBR/$CuSO_4$/DOP blend and vulcanizates were analyzed to investigate the occurrence of coordination reactions. As illustrated in Figure 4a, the N 1s spectra of the NBR/$CuSO_4$/DOP blend reveal a solitary nitrogen environment, displaying a central binding energy of 399.3 eV, which belonged to the nitrogen atoms of free cyano groups. However, after vulcanization, as illustrated in Figure 4b, a new peak appeared at higher binding energy (401.6 eV), and the shift is caused by the coordination of the cyano group with Cu^{2+}, which results in a transfer of electrons from the nitrogen atom to the metal ions [28]. The resulting increase in the internal electron binding energy of the coordinated nitrogen atoms leads to a different chemical environment compared to that of the NBR/$CuSO_4$/DOP blend without coordination, resulting in a shoulder peak at the higher binding energy in the XPS spectrum. These observations provide supporting evidence for forming coordination structures between Cu^{2+} and cyano groups in the NBR/$CuSO_4$/DOP vulcanizates.

3.2. Mechanical properties of NBR/$CuSO_4$/DOP vulcanizates

The stress-strain curves of NBR/$CuSO_4$/DOP vulcanizates with different $CuSO_4$ dosage were shown in Figure 5. The tensile strength of the series vulcanizates was substantially increased with the increasing $CuSO_4$ dosage, while the elongation at break was decreased gradually. For the coordination crosslinking vulcanizates, the metal-ligand coordination bond acts as a 'sacrificial bond', which could improve the tensile strength significantly while can maintain the relative high elongation at break [29, 30]. The increasing $CuSO_4$ dosage improved the coordination efficiency of the cyano group with Cu^{2+} greatly, resulting in an increased crosslinking density of the NBR vulcanizates (as shown in Table 3). Under the external force, the dumbbell-shaped sample was stretched to fracture and more coordination bonds were required to be broken, resulting in increased tensile strength. The mechanical properties of the series NBR/$CuSO_4$/DOP vulcanizates are summarized in Table 2. It can be observed that the tearing strength

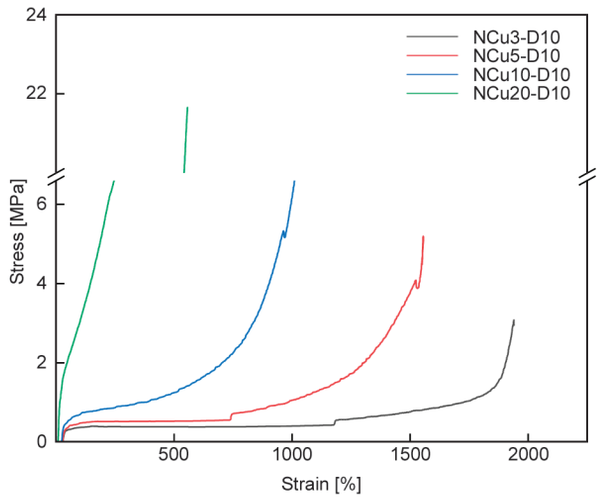

Figure 5. Stress–strain curves of NBR/$CuSO_4$/DOP vulcanizates with different $CuSO_4$ dosage at 180 °C.

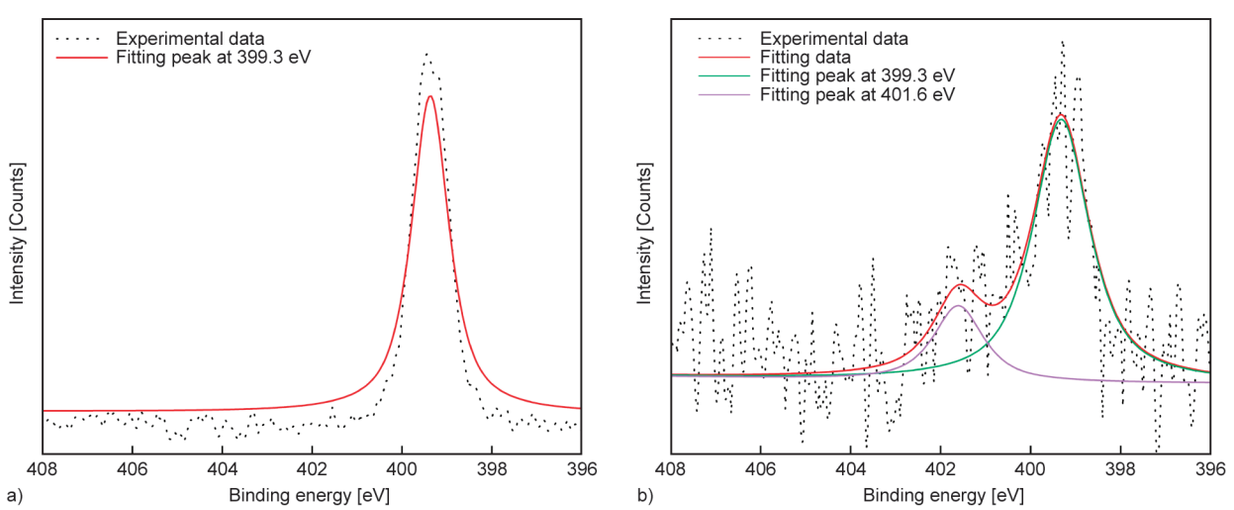

Figure 4. N 1s XPS spectra of NBR/$CuSO_4$/DOP blend and vulcanizate: a) NCu10-D10a; b) NCu10-D10b.

Table 2. Mechanical properties of NBR/$CuSO_4$/DOP vulcanizates.

Samples	Tensile strength [MPa]	Elongation at break [%]	Tearing strength [kN·m^{-1}]	Shore A hardness
NCu3-D10	3.08	1940	8.87	35
NCu5-D10	5.19	1557	10.84	42
NCu10-D10	6.62	1012	18.37	65
NCu20-D10	21.65	578	32.58	78

and Shore A hardness of the vulcanizates were increased with increasing $CuSO_4$ dosage, which can be attributed to the increasing crosslinking density.

3.3. Self-healing properties of NBR/$CuSO_4$/DOP vulcanizates

In order to assess the self-healing ability, the original dumbbell-shaped sample was cut into two separate pieces and then gently rejoined together to ensure good contact between the cutting surfaces, as shown in Figure 6. The samples were then subjected to various temperatures and duration for healing. Subsequently, the stress-strain behavior of the healed samples was tested at a stretch rate of 500 mm·min^{-1} after cooling to room temperature.

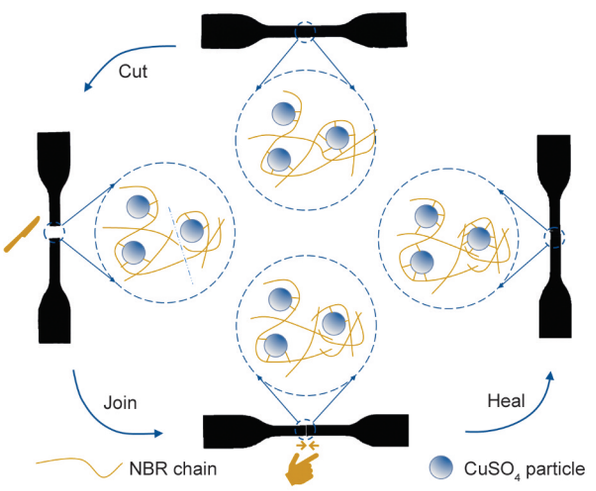

Figure 6. Diagrammatical illustration of self-healing behavior of vulcanizates.

Figure 7 shows the FE-SEM photographs of the cut position of the NCu10-D10 sample before and after healing (180 °C, 60 min). Figure 7a shows the surface of the sample with evident cutting marks, which have clear, sharp edges and an obvious 'step'-like fracture, indicating that the separating cut sample only keeps in contact with each other rather than producing a strong bonding. After healing at 180 °C for 60 min, as shown in Figure 7b, the cutting marks on the sample surface became blurry, and the edges of the cuts fused with each other, and the 'step'-like fractures was disappeared. Only a superficial depression could be found in the cut position, indicating the fine fracture healing after heat treatment.

The healed Dumbbell-shaped sample (180 °C for 60 min) could successfully sustain a 500 g load without breaking, as shown in Figure 8a, indicating the excellent self-healing capability of the NBR vulcanizate. Figure 8b displays the stress-strain curves of NCu10-D10 tested before and after healing at 180 °C for 60 min. It is evident that the healed sample was fractured at 6.4 MPa (the original sample was 6.6 MPa) with a healing efficiency of about 97%. At the elevated temperature, the chain mobility of the vulcanizates can be enhanced obviously, and the NBR molecular chains diffuse each other in the cutting surface. The Cu^{2+} exposed due to bond breakage and the uncoordinated Cu^{2+}, dispersed in NBR could

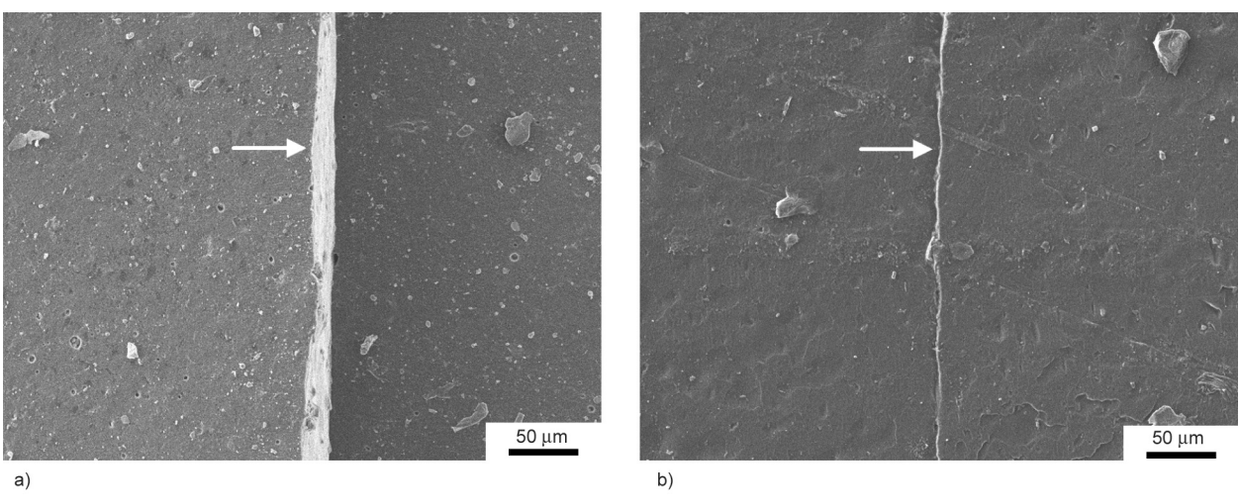

Figure 7. FE-SEM photographs of the cut position of NCu10-D10 before and after healing (180 °C, 60 min): a) before healing; b) after healing.

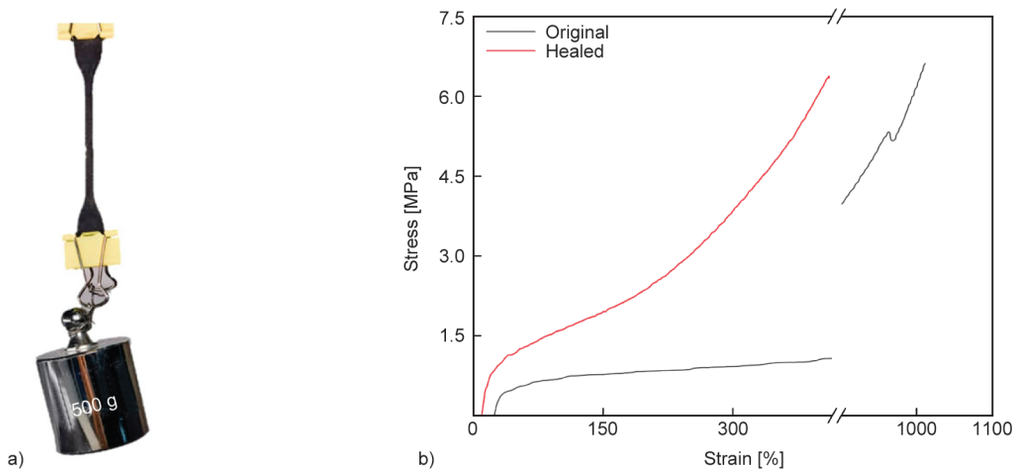

Figure 8. a) Photograph of NCu10-D10 hanging a 500 g load after healing; b) stress-strain curves of NCu10-D10 healed at 180 °C for 60 min.

reorganize with the cyano group to form a well-established network in the cutting surfaces. Moreover, the elastic modulus (as observed from the slope of the stress-strain curves) of the healed NCu10-D10 sample was significantly increased, and the elongation at break was significantly decreased compared to that of the original sample. This can be attributed to the repair of broken coordination bonds in the cutting surface and the formation of new coordination bonds during the healing treatment, resulting in increased crosslinking density. It is notable that, during the testing of the tensile strength of healed samples, many samples were not fractured at the cut position (refer to Figure 9), which is valuable evidence of the vulcanizate's excellent self-healing ability.

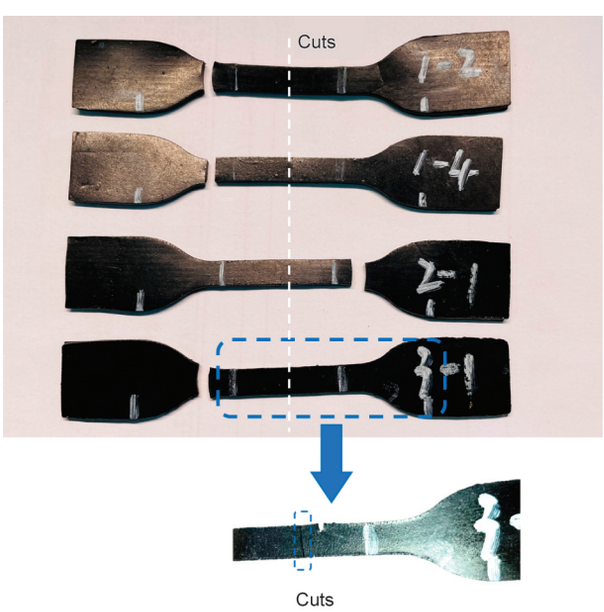

Figure 9. Digital photograph of the healed sample after fracture (Sample incisions are marked with white dashed lines).

Figure 10a illustrates the tensile strength of NCu10-D10 sample healed at different healing temperatures for different times. As can be seen from Figure 10a, the tensile strength of vulcanizates after healing was increased with the healing temperature and healing time remarkably. Under the same healing temperature and healing time (1 h, 60 °C), our study demonstrates higher tensile strength and healing efficiency than Mandal *et al.*'s work in 2021 [31]. Usually, the self-healing ability of the coordination bond-based materials is influenced by the viscosity of the interface, the diffusive mobility of molecular chain segments and the exchanging rate of coordination bonds [32, 33]. The coordination bond-based self-healing process involves both the reorganization and exchange of coordination bonds and the faster exchange rate of coordination bonds could improve the self-healing efficiency. Increasing the healing temperature and time can remarkably accelerate the diffusion rate of molecular chains and the exchange rate of coordination bonds.

Reorganization of the coordination crosslinked network is an important mechanism underlying the self-healing behavior of vulcanizates. To further investigate the reorganization of the coordination crosslinking network, the tensile stress relaxation experiments were conducted at various temperatures, as shown in Figure 10b. Generally, the stress relaxation curves of NBR vulcanizate exhibit a continuous decrease of stress with increasing relaxation time and the higher temperature could accelerate the stress relaxation. However, it was surprising to find that the stress relaxation curves of NCu10-D10 sample exhibited an abnormal phenomenon. With increasing temperature, the stress relaxation rate of NCu10-D10

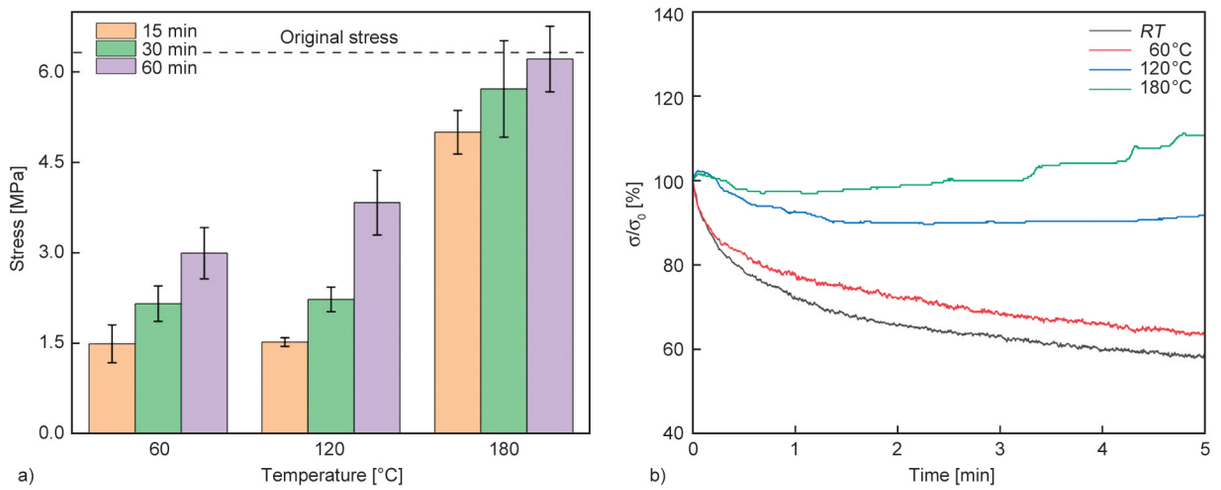

Figure 10. a) Tensile strength of NCu10-D10 healed at different temperature and time; b) tensile stress relaxation curves of NCu10-D10 at different temperature with 100% strain.

was significantly decreased. Interestingly, the stress relaxation curves of NCu10-D10 even exhibited stress recovery at 120 and 180 °C. This can be attributed to the reorganization of the coordination crosslinked network in the NBR vulcanizate under high temperature. The elevation of temperature accelerated the rate of coordination bond exchange, strengthening the coordination crosslinked network of the vulcanizate and requiring great force to maintain the original strain. Increasing healing temperature, the reorganization of the coordination crosslinked network in the vulcanizate occurred more rapidly, which was consistent with the influence of temperature on the healing strength, as shown in Figure 10a.

It should be noted that the influence of increasing healing temperature on the healing efficiency of the NBR vulcanizate is more sensitive than that of increasing healing time, as shown in Figure 11 and Figure 10a. Notably, the healing efficiency of the vulcanizates was only 16.7% after 72 h healing at room temperature, indicating that the coordination crosslinking network of vulcanizates is not active at room temperature. The lower temperature limits the exchange rate of coordination bonds, which hinders them from rebuilding in the short term after breaking. It also implies that the coordination crosslinking network is reversible, which could enable the recycling of vulcanizates through appropriate methods.

3.4. Recycling properties of NBR/$CuSO_4$/DOP vulcanizates

The recycled method of vulcanizates is shown in Figure 12. NCu10-D10 scraps were sheared using a two-roll mill for 20 min to obtain the plasticity, then

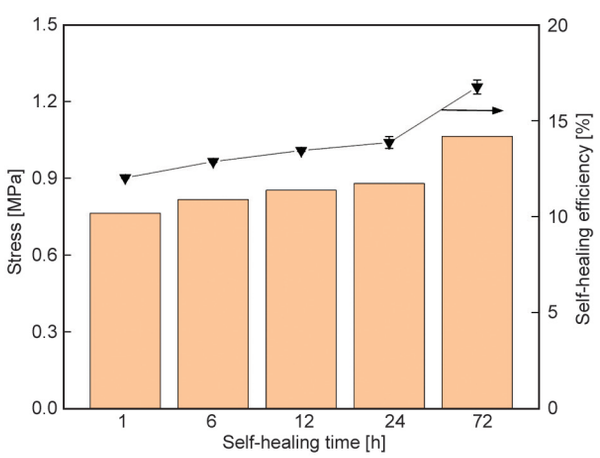

Figure 11. Tensile strength and healing efficiency of NCu10-D10 healed at different times at room temperature.

followed by hot-pressing at 180 °C for 20 min using a plate vulcanizing machine. The surface of the recycled vulcanizate was smooth and flat. Moreover, compared with the original vulcanizate, there was no discernible difference in appearance in the recycled vulcanizate.

We conducted serial tests to verify the recycling effect of vulcanizates after the mechanical shear.

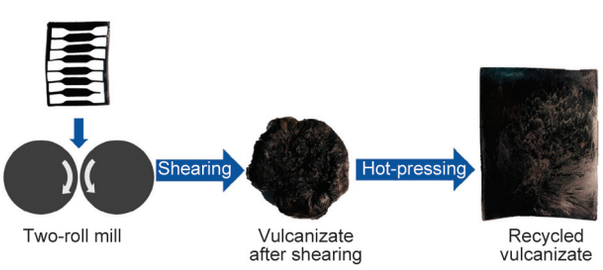

Figure 12. Schematic diagram of recycling method of vulcanizates.

Figures 13a, and 13b displays the N 1s XPS spectra of NCu10-D10 after being subjected to mechanical shearing and re-vulcanization. The N 1s spectra of NCu10-D10 after mechanical shearing exhibited a singular nitrogen environment with a central binding energy of 399.3 eV. This value is consistent with the N 1s spectra of the NBR/$CuSO_4$/DOP blend, which is shown in Figure 4a. It indicates that the coordination crosslinking network of vulcanizates underwent a reversible transformation after mechanical shearing and reverted to the unvulcanized condition. However, a shoulder peak appeared at a higher binding energy after the re-vulcanization, indicating that the re-vulcanized vulcanizates could recover the coordination structure after hot-pressing. Figure 13c shows the DSC curves of NCu10-D10 before and after mechanical shearing and re-vulcanized. Similarly, the transition of T_g in NCu10-D10 before and after mechanical shearing and the re-vulcanized process is attributed to the reversible transformation of the coordination crosslinking network. The coordination bonds in vulcanizates are broken by the strong mechanical shear force, reducing the constraint of the NBR chain segments and reducing the T_g value. After re-vulcanization, the coordination crosslinking network of vulcanizates is reconstructed with a subsequent increase in T_g. The T_g of the re-vulcanized vulcanizates is higher than that of the NBR vulcanizates, which should be due to the higher crosslinking density (refer to Table 3). Figure 13d shows the stress-strain curves of NCu10-D10 after the re-vulcanization treatment. The tensile strength of the re-vulcanized vulcanizate was almost the same compared to the original sample. Moreover, an increase in elastic modulus (as observed from the slope of the stress-strain curves) of re-vulcanized NCu10-D10

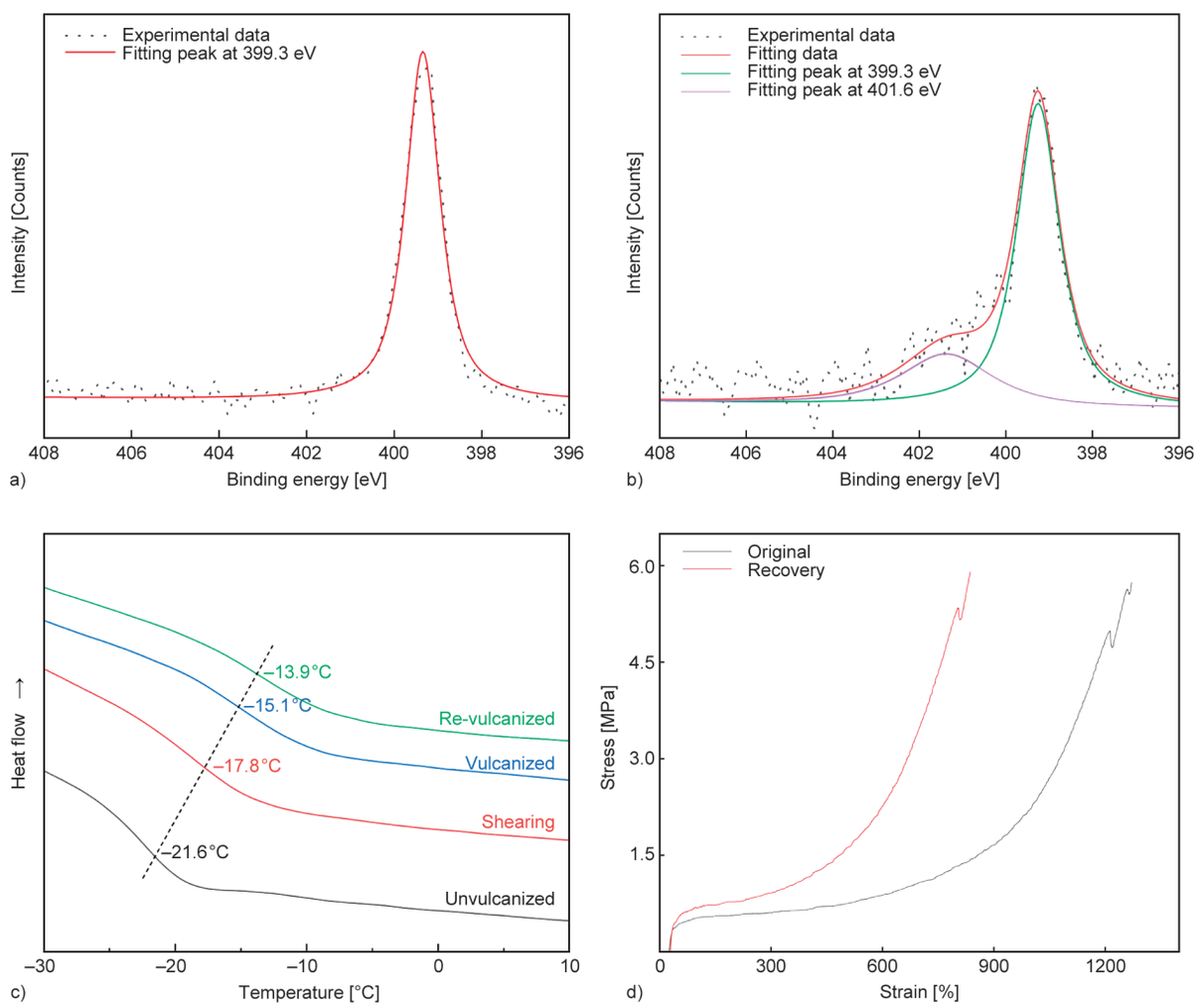

Figure 13. a) N 1s XPS spectra of NCu10-D10 after shearing and b) re-vulcanized; c) DSC curves of NCu10-D10 with recycled process; d) stress-strain curves of NCu10-D10 after re-vulcanization.

was also observed in Figure 13d, which can be attributed to the increased crosslinking density of the re-vulcanized NBR vulcanizate.

3.5. Swelling properties of NBR/$CuSO_4$/DOP vulcanizates

The coordination crosslinking behavior of the series NCu10-D10 vulcanizates was visually investigated by the swelling experiments, as shown in Figure 14. The unvulcanized NCu10-D10 was completely dissolved by DCM at room temperature, indicating that the NBR matrix was not crosslinked. Interestingly, the mechanical sheared NCu10-D10 sample was almost completely dissolved after 24 h of immersion in DCM as well, indicating that the coordination crosslinking network had already disappeared after mechanical shear. Conversely, the vulcanized NCu10-D10 and re-vulcanized NCu10-D10 could not be dissolved completely but only partially swelled, indicating that the crosslinking between the cyano group and Cu^{2+} had occurred after hot-pressing. After 24 hours of immersion, the re-vulcanized NCu10-D10 exhibited less swelling compared to the vulcanized NCu10-D10, indicating the formation of more crosslinking points between molecular chain segments in the re-vulcanized NCu10-D10. The observation agrees with the crosslinking density calculated using the Flory-Rehner equation, as shown in Table 3.

Table 3. Dissolvability and crosslinking density of NBR/$CuSO_4$/DOP blend and vulcanizates by swelling at equilibrium.

Sample	Dissolvability	Crosslinking density $\cdot 10^{-5}$ [mol/cm^3]
NCu3-D10	×	0.13
NCu5-D10	×	0.37
NCu10-D10a	√	/
NCu10-D10b	×	2.11
Sheared NCu10-D10	√	/
Re-vulcanized NCu10-D10	×	2.79
NCu20-D10	×	3.45

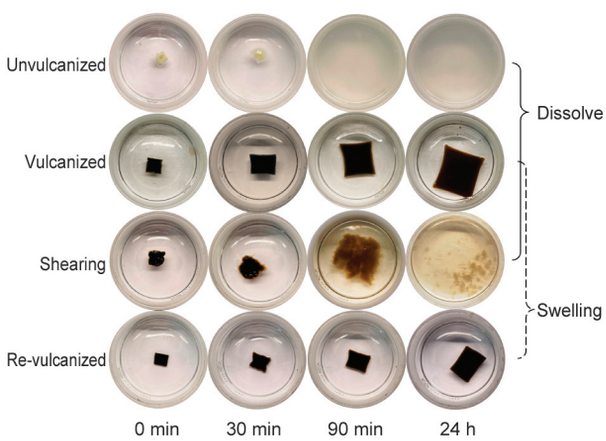

Figure 14. Digital pictures of swelling experiments in DCM of series NCu10-D10 vulcanizates.

4. Conclusions

In conclusion, a facile strategy was developed to create an NBR with remarkable mechanical properties, excellent self-healing, and recycling abilities by introducing metal-ligand coordination interactions through simple mechanical blending. The curing curves, DSC, XPS, and equilibrium swelling experiments demonstrated the successful formation of the coordination crosslinking network. Crosslinking of NBR chains was achieved by using Cu^{2+}-cyano coordination bonds instead of conventional crosslinking agents such as sulfur or peroxide. The $CuSO_4$ dosage strongly affects the mechanical properties of the prepared vulcanizates, and the vulcanizates exhibited excellent mechanical properties, including a stretchability of up to 1900% (NCu3-D10) and a tensile strength of up to 21.7 MPa (NCu20-D10). Moreover, the NBR/$CuSO_4$/DOP vulcanizates possessed the excellent self-healing and recycling properties, which is due to the dynamic reversibility of the coordination crosslinking network. The healing temperature and healing time played a critical role in determining the self-healing properties of the vulcanizates, with a remarkable healing efficiency of up to 97% of the original tensile strength achieved after healing at 180 °C for 60 min. Furthermore, the tensile strength of the NBR/$CuSO_4$/DOP vulcanizates after recycling was comparable to that of the original sample. It is believed that this strategy of preparing a combination of excellent mechanical and self-healing properties has great potential for application in other polar polymers.

Acknowledgements

The work was supported by the Shandong Provincial Natural Science Foundation, China [grant number ZR2021ME028].

References

[1] White S. R., Sottos N. R., Geubelle P. H., Moore J. S., Kessler M. R., Sriram S., Brown E. N., Viswanathan S.: Autonomic healing of polymer composites. Nature, **409**, 794–797 (2001). https://doi.org/10.1038/35057232

[2] Habault D., Zhang H., Zhao Y.: Light-triggered self-healing and shape-memory polymers. Chemical Society Reviews, **42**, 7244–7256 (2013). https://doi.org/10.1039/C3CS35489J

[3] Das A., Sallat A., Böhme F., Suckow M., Basu D., Wießner S., Stöckelhuber K. W., Voit B., Heinrich G.: Ionic modification turns commercial rubber into a self-healing material. ACS Applied Materials and Interfaces, **7**, 20623–20630 (2015). https://doi.org/10.1021/acsami.5b05041

[4] Xu C., Cao L., Lin B., Liang X., Chen Y.: Design of self-healing supramolecular rubbers by introducing ionic cross-links into natural rubber *via* a controlled vulcanization. ACS Applied Materials and Interfaces, **8**, 17728–17737 (2016). https://doi.org/10.1021/acsami.6b05941

[5] Ryu Y. S., Oh K. W., Kim S. H.: Synthesis and characterization of a furan-based self-healing polymer. Macromolecular Research, **24**, 874–880 (2016). https://doi.org/10.1007/s13233-016-4122-5

[6] Hou H. H., Yin J., Jiang X. S.: Reversible diels-alder reaction to control wrinkle patterns: From dynamic chemistry to dynamic patterns. Advanced Materials, **28**, 9126–9132 (2016). https://doi.org/10.1002/adma.201602105

[7] Lai Y., Kuang X., Zhu P., Huang M. M., Dong X., Wang D. J.: Colorless, transparent, robust, and fast scratch-self-healing elastomers *via* a phase-locked dynamic bonds design. Advanced Materials, **30**, 1802556 (2018). https://doi.org/10.1002/adma.201802556

[8] Cordier P., Tournilhac F., Soulie-Ziakovic C., Leibler L.: Self-healing and thermoreversible rubber from supramolecular assembly. Nature, **451**, 977–980 (2008). https://doi.org/10.1038/nature06669

[9] Xu C., Cao L., Huang X., Chen Y., Lin B., Fu L.: Self-healing natural rubber with tailorable mechanical properties based on ionic supramolecular hybrid network. ACS Applied Materials and Interfaces, **9**, 29363–29373 (2017). https://doi.org/10.1021/acsami.7b09997

[10] Wang Z., Xie C., Yu C., Fei G., Wang Z., Xia H.: A facile strategy for self-healing polyurethanes containing multiple metal-ligand bonds. Macromolecular Rapid Communications, **39**, 1700678 (2018). https://doi.org/10.1002/marc.201700678

[11] Cui X., Song Y., Wang J-P., Wang J-K., Zhou Q., Qi T., Li G. L.: Self-healing polymers with tunable mechanical strengths *via* combined hydrogen bonding and zinc-imidazole interactions. Polymer, **174**, 143–149 (2019). https://doi.org/10.1016/j.polymer.2019.04.060

[12] Kasem H., Shriki H., Ganon L., Mizrahi M., Abd-Rbo K., Domb A. J.: Rubber plunger surface texturing for friction reduction in medical syringes. Friction, **7**, 351–358 (2019). https://doi.org/10.1007/s40544-018-0227-5

[13] Ramezani M., Ripin Z. M., Ahmad R.: Computer aided modelling of friction in rubber-pad forming process. Journal of Materials Processing Technology, **209**, 4925–4934 (2009). https://doi.org/10.1016/j.jmatprotec.2009.01.015

[14] Jaafar C. N. A., Zainol I., Ishak N. S., Ilyas R. A., Sapuan S. M.: Effects of the liquid natural rubber (LNR) on mechanical properties and microstructure of epoxy/silica/kenaf hybrid composite for potential automotive applications. Journal of Materials Research and Technology, **12**, 1026–1038 (2021). https://doi.org/10.1016/j.jmrt.2021.03.020

[15] Rodriguez N., Dorogin L., Chew K. T., Persson B. N. J.: Adhesion, friction and viscoelastic properties for non-aged and aged styrene butadiene rubber. Tribology International, **121**, 78–83 (2018). https://doi.org/10.1016/j.triboint.2018.01.037

[16] Li B., Li S-X., Shen M-X., Xiao Y-L., Zhang J., Xiong G-Y., Zhang Z-N.: Tribological behaviour of acrylonitrile-butadiene rubber under thermal oxidation ageing. Polymer Testing, **93**, 106954 (2021). https://doi.org/10.1016/j.polymertesting.2020.106954

[17] Asaro L., Gratton M., Seghar S., Hocine N. A.: Recycling of rubber wastes by devulcanization. Resources, Conservation and Recycling, **133**, 250–262 (2018). https://doi.org/10.1016/j.resconrec.2018.02.016

[18] Molanorouzi M., Mohaved S. O.: Reclaiming waste tire rubber by an irradiation technique. Polymer Degradation and Stability, **128**, 115–125 (2016). https://doi.org/10.1016/j.polymdegradstab.2016.03.009

[19] Movahed S. O., Ansarifar A., Zohuri G., Ghaneie N., Kermany Y.: Devulcanization of ethylene–propylene–diene waste rubber by microwaves and chemical agents. Journal of Elastomers & Plastics, **48**, 122–144 (2016). https://doi.org/10.1177/0095244314557975

[20] Shields Y., De Belie N., Jefferson A., van Tittelboom K.: A review of vascular networks for self-healing applications. Smart Materials and Structures, **30**, 063001 (2021). https://doi.org/10.1088/1361-665X/abf41d

[21] Peng T., Huang J., Gong Z., Chen X., Chen Y.: Self-healing of reversibly cross-linked thermoplastic vulcanizates. Materials Chemistry and Physics, **292**, 126804 (2022). https://doi.org/10.1016/j.matchemphys.2022.126804

[22] Liu Y., Li Z., Liu R., Liang Z., Yang J., Zhang R., Zhou Z., Nie Y.: Design of self-healing rubber by introducing ionic interaction to construct a network composed of ionic and covalent cross-linking. Industrial and Engineering Chemistry Research, **58**, 14848–14858 (2019). https://doi.org/10.1021/acs.iecr.9b02972

[23] Shen F., Yuan X-F., Guo W-H., Wu C-F.: Coordination crosslinking of nitrile rubber filled with copper sulfate particles. Chinese Journal of Polymer Science, **25**, 447–459 (2007). https://doi.org/10.1142/S0256767907002345

[24] Mou H., Shen F., Shi Q., Liu Y., Wu C., Guo W.: A novel nitrile butadiene rubber/zinc chloride composite: Coordination reaction and miscibility. European Polymer Journal, **48**, 857–865 (2012). https://doi.org/10.1016/j.eurpolymj.2012.02.004

[25] Li C-H., Zuo J-L.: Self-healing polymers based on coordination bonds. Advanced Materials, **32**, 1903762 (2020). https://doi.org/10.1002/adma.201903762

[26] Flory P. J.: Statistical mechanics of swelling of network structures. The Journal of Chemical Physics, **18**, 108–111 (1950). https://doi.org/10.1063/1.1747424

[27] Sun Y., Wang J., Sun L., Hua J., Wang Z.: Synergistic effect of copper sulfate and tetramethylthiuram monosulfide induced metal-coordination cross-linking in nitrile–butadiene rubber. Macromolecular Materials and Engineering, **306**, 2100057 (2021). https://doi.org/10.1002/mame.202100057

[28] Cano A., Avila Y., Avila M., Reguera E.: Structural information contained in the XPS spectra of nd^{10} metal cyanides. Journal of Solid State Chemistry, **276**, 339–344 (2019). https://doi.org/10.1016/j.jssc.2019.05.021

[29] Liu J., Wang S., Tang Z., Huang J., Guo B., Huang G.: Bioinspired engineering of two different types of sacrificial bonds into chemically cross-linked cis-1,4-polyisoprene toward a high-performance elastomer. Macromolecules, **49**, 8593–8604 (2016). https://doi.org/10.1021/acs.macromol.6b01576

[30] Liu Y., Tang Z., Wu S., Guo B.: Integrating sacrificial bonds into dynamic covalent networks toward mechanically robust and malleable elastomers. ACS Macro Letters, **8**, 193–199 (2019). https://doi.org/10.1021/acsmacrolett.9b00012

[31] Mandal S., Simon F., Banerjee S. S., Tunnicliffe L. B., Nakason C., Das C., Das M., Naskar K., Wiessner S., Heinrich G., Das A.: Controlled release of metal ion cross-linkers and development of self-healable epoxidized natural rubber. ACS Applied Polymer Materials, **3**, 1190–1202 (2021). https://doi.org/10.1021/acsapm.1c00039

[32] Bode S., Enke M., Bose R., Schacher F., Garcia S., van der Zwaag S., Hager M., Schubert U.: Correlation between scratch healing and rheological behavior for terpyridine complex based metallopolymers. Journal of Materials Chemistry A, **3**, 22145–22153 (2015). https://doi.org/10.1039/C5TA05545H

[33] Wang D-P., Lai J-C., Lai H-Y., Mo S-R., Zeng K-Y., Li C-H., Zuo J-L.: Distinct mechanical and self-healing properties in two polydimethylsiloxane coordination polymers with fine-tuned bond strength. Inorganic Chemistry, **57**, 3232–3242 (2018). https://doi.org/10.1021/acs.inorgchem.7b03260

Express Polymer Letters Vol.17, No.10 (2023) 1031–1041
Available online at www.expresspolymlett.com
https://doi.org/10.3144/expresspolymlett.2023.77

Research article

The polymorphic composition of long-chain branched polypropylene processed by injection and compression molding

Lenka Gajzlerova, Jana Navratilova, Martina Polaskova, Lubomir Benicek, Roman Cermak*

Tomas Bata University in Zlin, Faculty of Technology, Vavreckova 5669, 760 01 Zlin, Czech Republic

Received 22 March 2023; accepted in revised form 7 July 2023

Abstract. The impact of injection molding processing parameters, including mold temperature, injection speed, and holding pressure, on the supermolecular structure of long-chain branched polypropylene (LCB-PP) was investigated. Commercial LCB-PP was processed under different conditions, with four sets of processing parameters applied. Holding pressure was varied from 30–70 MPa by 10 MPa in the P-SET, mold temperature was raised from 40 to 120 °C in 20 °C steps in the T-SET, and injection speed increased from 20 to 140 mm/s in 30 mm/s steps in S-SET1 and S-SET2, with mold temperatures at 40 or 120 °C. The polymorphic composition of the specimens was analyzed using wide-angle X-ray scattering, demonstrating a strong dependence on the processing parameters. The skin of the specimens showed an increase in β-phase content with higher mold temperature and injection speed. Conversely, growing holding pressure slightly suppressed β-phase content and promoted the formation of the γ-phase, which was predominantly manifested in the core of the specimens. The polymorphic composition, with both β- and γ-phases present in notable amounts, had a beneficial effect on the impact strength of the specimens.

Keywords: *processing technologies, material testing, mechanical properties, long-chain branched polypropylene, polymorphism*

1. Introduction

Polymorphism of polymers is a very interesting phenomenon predetermining the end-use properties of products. As a result, it is essential to carefully control specific nucleation and processing parameters to achieve the desired characteristics. Flow-induced crystallization is particularly important in manufacturing processes such as injection and blow molding [1–4]. The utilization of flow fields has been shown to accelerate crystallization kinetics [4], enhance nucleation density [5], and induce various morphologies, such as oriented crystalline structures like shish-kebab [6] or β-crystals [7]. Therefore, understanding the mechanisms of applied shear fields, as characterized by flow rate and temperature, and their impact on polymorphism is crucial in optimizing processing conditions.

Isotactic polypropylene (iPP) and its modifications, *e.g.*, long-chain branched polypropylene, are among the most widely used polymorphic polymers due to their versatility in terms of both property function and processability [8]. The molecular structure of iPP allows it to solidify into several crystallographic modifications, including the α-, β-, and γ-phases, as well as the mesomorphic 'smectic' phase formed during high undercooling. Only a small fraction of the

*Corresponding author, e-mail: j1navratilova@utb.cz
© BME-PT

material, the ε-crystal modification, is obtained with the most stereodefective or 'an-isotactic' part of iPP produced with a zirconene catalyst [9, 10].

Nevertheless, only monoclinic α-phase and trigonal β-phase possess relevance to practice [8, 11]. The α-modification is the most common phase of iPP and grows dominantly under normal processing conditions. The β-modification is thermodynamically less favorable and recrystallizes into the α-phase on heating. However, several special crystallization techniques have been developed – the temperature gradient method [12], shear-induced crystallization [13, 14], or the most effective specific nucleation caused by an insertion of the heterogeneous β-nucleating agent [15–18]. Nucleating agents, which are typically low-molecular-mass organic or inorganic substances added to polymers, can induce specific β-nucleation that enhances the toughness of iPP while reducing its stiffness and heat resistance [18–20]. In comparison to the ordinary α-phase, this modification also improves resistance to photodegradation [21–23]. The orthorhombic γ-phase is another metastable polymorph of iPP that can form in the presence of chain irregularities, such as stereo- or regio-irregularities, through methods such as metallocene catalyzed crystallization [24, 25], high-pressure crystallization of homopolymers [26], crystallization of very low molecular weight fractions of iPP [27], or through the crystallization of propylene copolymers containing small amounts of 1-olefin co-units [28]. Long-chain branched polypropylene (LCB-PP) typically contains a higher content of chain irregularities, resulting in a higher tendency to form γ-phase. LCB-PP can be produced by introducing a long-chain branching architecture onto the polypropylene backbone using techniques such as in situ polymerization in a reactor [29], high energy irradiation [30], or melt-free radical grafting, with the latter being the most commonly used method [31, 32]. The crystalline system of LCB-PP usually consists of α- and γ-phases, with the formation of β-phase being suppressed under standard processing conditions [15, 33]. LCB-PP exhibits unique crystallization behavior compared to iPP, including higher crystallization temperature, faster overall crystallization, and a broader melting scale [15, 34]. LCB-PP also exhibits high melt strength and strain hardening in elongational flow, making it suitable for various industrial processes such as foaming, blow film processing, blow molding, and thermoforming [35, 36].

However, certain processing techniques that involve a dominant shear field, such as injection molding, can facilitate the development of desirable crystalline structures in long-chain branched polypropylene. Recent research by Zhou *et al*. [37] has revealed an increase in the β-phase content of LCB-PP with increasing LCB structure content, along with the occurrence of the trigonal modification. While flow-induced crystallization of isotactic polypropylene has been extensively studied, less is known about the crystallization behavior of LCB-PP under complex flow fields [1, 4, 37, 38]. Therefore, the objective of this study is to investigate the influence of important processing parameters, including injection speed, holding pressure, and mold temperature, on the morphology evolution and distribution of β- and/or γ-crystals in the 'skin-core' structure of LCB-PP. This structure results from non-homogeneous flow fields and thermo-mechanical conditions in the thickness direction, with the final polymorphic composition reflecting mechanical properties such as impact strength. The results of this research could offer a comprehensive understanding of shear-induced crystallization behavior in LCB-PP and potentially enable the prediction and customization of the final multi-component crystalline system, thereby enhancing the prospects for successful processing and industrial utilization.

2. Experimental

2.1. Material

In this study, Daploy WB140HMS was utilized, a commercially available long-chain branched polypropylene supplied by Borealis Company in Vienna, Austria. This propylene-based polymer is produced through in situ polymerization, where monomers are grafted onto isotactic polypropylene using peroxides to create long-chain branches. The examined material has a melt flow rate of 2.8 g/10 min, as measured at 230 °C and 2.16 kg using the ISO 1133 standard, weight-averaged molecular weight of 600 000, and polydispersity index of 5.2.

2.2. Specimens preparation

For the preparation of specimens, a Demag NC4 injection molding machine, Demag AG, Dusseldorf, Germany, was used to mold Charpy test specimens following ISO 179-1 with dimensions of 80×10×4 mm. The parameters of the mold were: sprue diameter ranging from 3.5 to 6.0 mm, runner

diameter of 10 mm, the gate located at the top side of the specimen with dimensions of 7×4 mm, and a length of 5 mm. Four sets of processing parameters were employed, namely P-SET with holding pressure varied from 30 to 70 MPa by 10 MPa, T-SET with mold temperature precisely controlled at temperatures increasing from 40 to 120 °C in 20 °C increments, and S-SET1 and S-SET2 with injection speed ranging from 20 to 140 mm/s in 30 mm/s increments and a mold temperature of 40 or 120 °C, respectively. Other parameters remained constant, as shown in Table 1. For the investigation of the effect of processing parameters on the supermolecular structure of the material, the same Charpy test specimens were also compression-molded (CM) in a manual press from Versta, Zlin, Czech Republic: at a pressing temperature of 210 °C for 5 min and cooled at 80 °C for 5 min. The skin and core of the specimens were analyzed using wide-angle X-ray scattering (WAXS), where the core was exposed by grinding off two millimeters of material from the surface using a Buehler Phoenix Alpha 1, Buehler, Lake Bluff, Illinois, USA. Grinding was carried out under running water at a temperature of 15 °C.

2.3. Wide-angle X-ray scattering

Wide-angle X-ray scattering was applied in order to obtain information about the crystallinity and polymorphic composition of specimens. X-ray patterns were taken of both the skin and the core of the specimens using an XRDynamic 500 diffractometer, Anton Paar, Graz, Austria, with Bragg-Brentano beam geometry in reflection mode, CuK_α radiation with a Ni filter ($\lambda = 0.154$ nm) and the diffraction angle interval of $2\theta = 5–30°$ was used. The peak search algorithm was based on the second derivative of the measured data, which showed local minima at peak positions. Peaks were searched and fitted using a variant of the pseudo-Voigt profile, which is a linear combination of a Gaussian and a Lorentzian curve. For the determination of the total crystallinity (X) of the specimens and polymorphic composition (K_β, K_γ), the data were fitted using a linear combination of Chebyshev polynomials. The total crystallinity was calculated from the share of the fitted areas of the crystalline part (A_C) and amorphous part (A_A) using Equation (1):

$$X = \frac{A_C}{A_C + A_A} \cdot 100\ [\%] \tag{1}$$

The multi-component α/β/γ crystalline system was determined using Equations (2)–(5) given by Obadal *et al*. [39] based on Turner-Jones *et al*.' work [40]. The K_β and K_γ, respectively, represent relative β- and γ-phase content in the three-phase crystalline system of polypropylene and can be calculated as Equation (2):

$$K_\beta = \frac{I_\beta}{I_{\alpha_1} + I_{\alpha_2} + I_{\alpha_3} + I_\beta + I_\gamma} \cdot 100\ [\%] \tag{2}$$

where $I_{\alpha 1}$, $I_{\alpha 2}$, $I_{\alpha 3}$, I_β, and I_γ denote the integral intensities of the individual diffraction peaks (α_1 at $2\theta = 14.20°$, α_2 at 17.00°, α_3 at 18.80°, β at 16.20° and γ at 20.05°).

The common content of both α- and γ-phases ($K_{\alpha+\gamma}$) in a three-phase crystalline system can be expressed (Equation (3)):

$$K_{\alpha+\gamma} = 1 - K_\beta \tag{3}$$

In the γ/α crystalline system, reflections at $2\theta = 14.2°$ and 17.0° are shared by both α- and γ-phases. Thus, γ-phase part (G) in the crystalline part can be derived only from the intensities of (130) α_3 reflection ($I_{\alpha 3}$ at 18.80°) and (117) γ reflection (I_γ at 20.05°), that are unique reflections for each phase [41] (Equations (4) and (5)):

$$G = \frac{I_\gamma}{I_{\alpha_3} + I_\gamma} \cdot 100\ [\%] \tag{4}$$

$$K_\gamma = G \cdot K_{\alpha+\gamma} \tag{5}$$

Table 1. Processing parameters of injection molding.

	Parameter	Unit	Value
	Temperatures of heating zones	°C	190; 220; 230
	Melt temperature (nozzle)	°C	240
	Holding pressure time	s	60
T-SET	Mold temperature	°C	40 / 60 / 80 / 100 / 120
	Injection speed	mm/s	80
	Holding pressure	MPa	50
P-SET	Holding pressure	MPa	30 / 40 / 50 / 60 / 70
	Mold temperature	°C	40
	Injection speed	mm/s	80
S-SET1	Injection speed	mm/s	20 / 50 / 80 / 110 / 140
	Mold temperature	°C	40
	Holding pressure	MPa	50
S-SET2	Injection speed	mm/s	20 / 50 / 80 / 110 / 140
	Mold temperature	°C	120
	Holding pressure	MPa	50

The above method allows for a relative calculation of the polymorphic composition in three-phase crystalline systems of polypropylene; however, the results can be used to quantify multiphase crystalline systems.

2.4. Charpy impact test

Non-instrumented Charpy impact tests were performed on a Charpy impact tester Impact 803, Tinius Olsen, Salfords Surrey, United Kingdom, using the specimens with a V-notch. The tests were carried out with a striker energy of 1.97 J and a span length of 62 mm at 23 °C. The average values of notched Charpy impact energy were obtained from each group of ten specimens.

3. Results and discussion

3.1. Polymorphic composition

The skin and core layers of the specimens prepared under various processing conditions were analyzed using X-ray diffractograms (Figures 1–5). The peaks of the main planes of various phases demonstrate common diffraction spectra of polymorphic crystalline systems. Injection-molded specimens show monoclinic α-phase α_1 (110), α_2 (040), and α_3 (130), trigonal β-phase (300), and orthorhombic γ-phase (117) peaks, as seen in Figures 1–4. The skin layer of all specimens exhibits a distinct β-diffraction peak, while the core layer shows a less significant peak. Diffractograms of compression-molded specimens (Figure 5) almost solely contain peaks corresponding to α-phase and γ-phase (117), with a negligible amount of trigonal β-phase. These results illustrate the significant influence of processing conditions on the LCB-PP's polymorphic composition.

Crystallinity and the relative amount of β-phase and γ-phase in the skin and core of specimens were determined by deconvoluting WAXS patterns and evaluated using Equations (1)–(5). These parameters, as a function of mold temperature, holding pressure, or injection speed, are shown in Figures 6–9. The reported dependences were determined at a significance level of $\alpha = 0.05$. It was found that the processing technology used significantly affects the crystallinity achieved. Table 2 shows that compression-molded specimens had lower crystallinity, reaching around 55% in the skin and 54% in the core, compared to injection-molded specimens. The content of γ-phase in compression-molded specimens was around 12%, regardless of the skin/core position

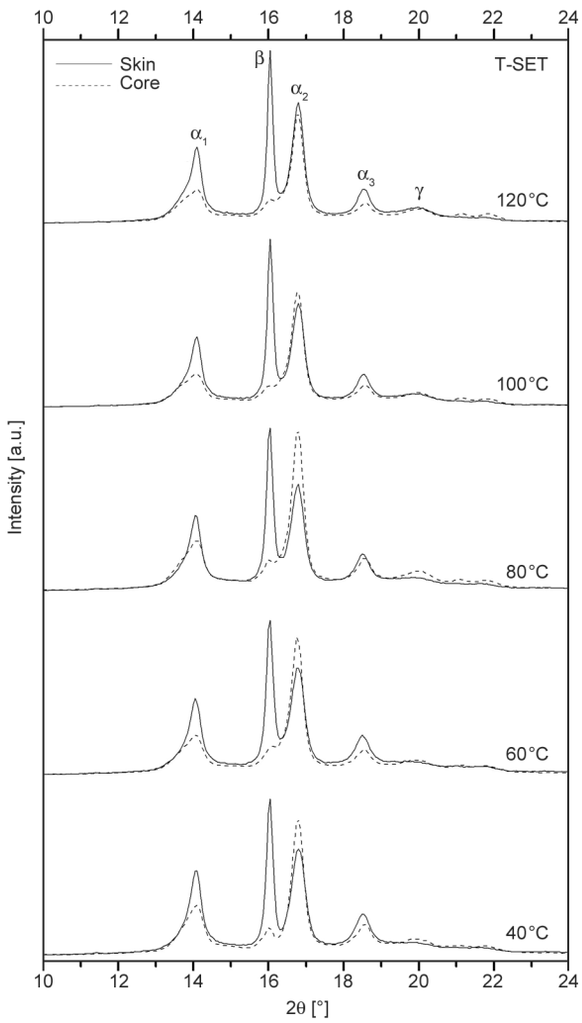

Figure 1. X-ray diffraction patterns of specimens injection-molded into the mold with various temperatures – T-SET.

(Figure 6), and the amount of β-phase was negligible. The effect of processing parameters on the crystallinity of injection-molded specimens was not significant (Table 2). The skin layer had crystallinity of around 69%, with the core having slightly lower values in most cases, regardless of holding pressure, injection speed, or mold temperature, except for high mold temperature (120 °C), which led to an increase in skin layer crystallinity. The skin crystallized at almost the same temperature as the mold temperature, while the core solidified under more complex thermal conditions due to the low thermal conductivity of polypropylene melt. There was no observable dependence of crystallinity on mold temperature in the core.

An interesting observation can be made by comparing the morphology evolution throughout the thickness of injection-molded specimens - the co-existence of α-, β-, and γ-phases. It has been reported that γ-crystals

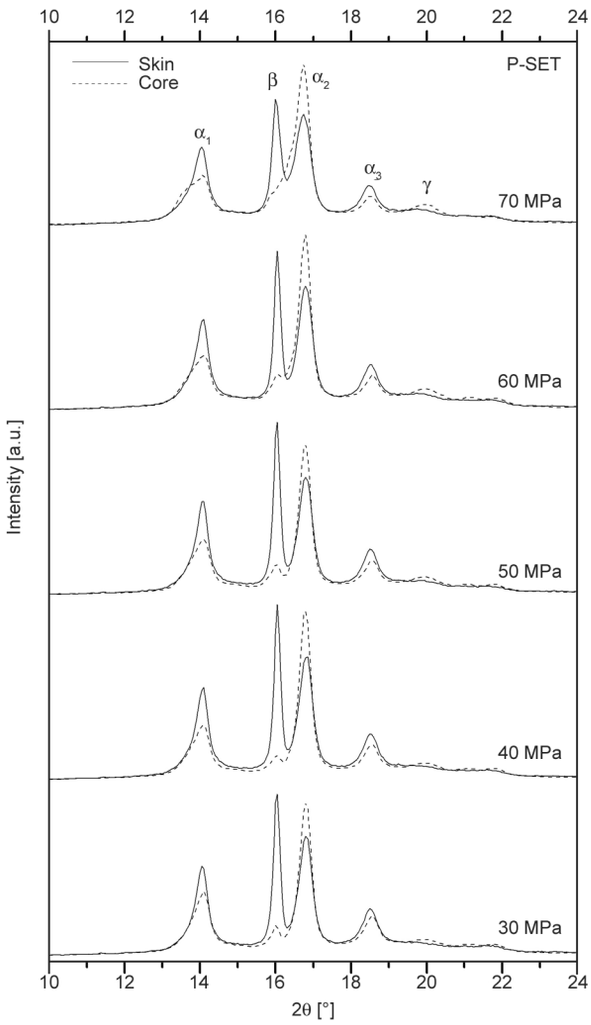

Figure 2. X-ray diffraction patterns of specimens injection-molded with various holding pressures – P-SET.

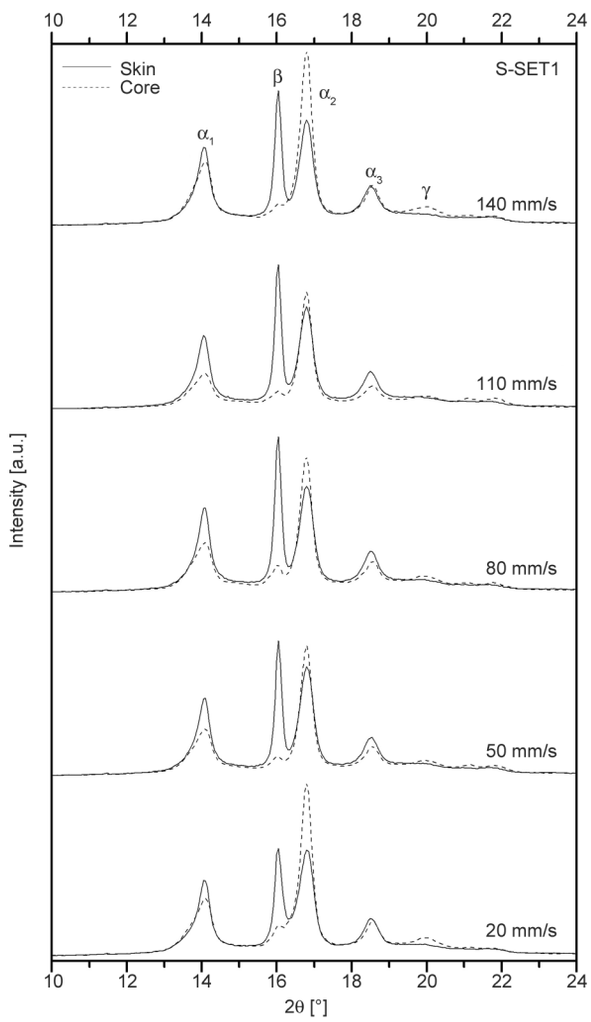

Figure 3. X-ray diffraction patterns of specimens injection-molded in various injection speeds into the mold with the temperature of 40 °C – S-SET1.

are formed due to the presence of stereo- and regio-defects [41], whereas the formation of β-crystals is induced under the flow field. The shearing of polypropylene melt causes the creation of α-row nuclei, which subsequently leads to the growth of the β-phase on the formed α-nuclei [1, 42].

The influence of mold temperature on the content of β- and γ-phases can be seen in Figure 6. The data also indicate that the polymorphic composition of LCB-PP is significantly affected by the skin-core structure. An increase in both phases with increasing mold temperature can be observed, particularly in the case of the γ-phase. Its content in the skin layer doubled from 7 to 14%, while in the core, it increased by about half, from 25 to 37%, for mold temperatures in the range of 40–120 °C which is expected trend based on earlier works [24, 25]. Crystallization temperatures above 110 °C result in nearly exclusive formation of the γ-modification, which is thermodynamically favored over the α-modification [43, 44].

In the case of the β-phase, a slightly higher content of over 40% was observed in the skin layer, and only a small increase in this trigonal phase was observed with increasing mold temperature. However, the formation of the β-phase in the core of LCB-PP was minimally influenced by processing conditions, as its content in all specimens was very low or negligible. The growth rate of the β-modification reaches its maximum at approximately 120 °C [16]. It is known that shear flow leads to oriented or even stretched polymer chains, which subsequently crystallize with different kinetics than under steady-state conditions. The shear flow influences both the nucleation and crystal growth steps. Nevertheless, the flow-enhanced crystallization rate is mainly due to a considerable increase in the nucleation rate and the density of nuclei. In this context, temperature is very crucial because it impacts the relaxation of the polymer chains or their segments. The influence of flow

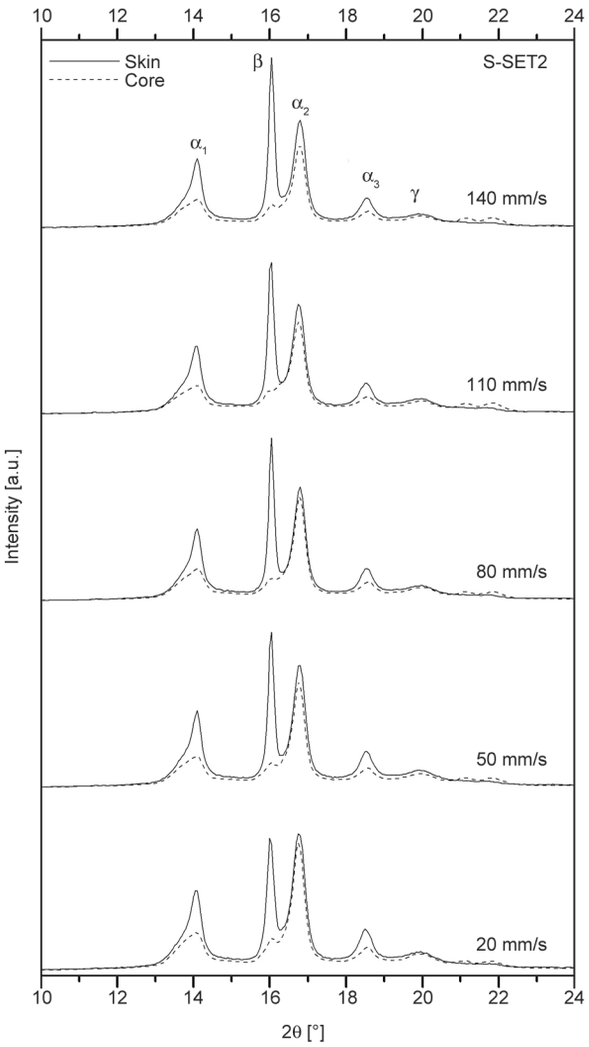

Figure 4. X-ray diffraction patterns of specimens injection-molded in various injection speeds into the mold with the temperature of 120 °C – S-SET2.

on polypropylene nucleation is more effective at high crystallization temperatures because the rate of resting crystallization tends to zero with increasing temperature as the temperature gets near the thermodynamic melting point. However, the orientation

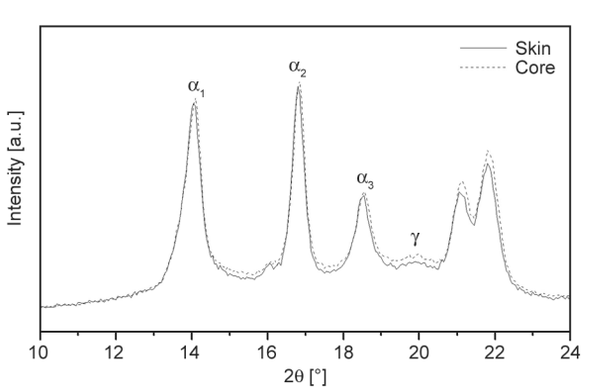

Figure 5. X-ray diffraction patterns of compression-molded specimens.

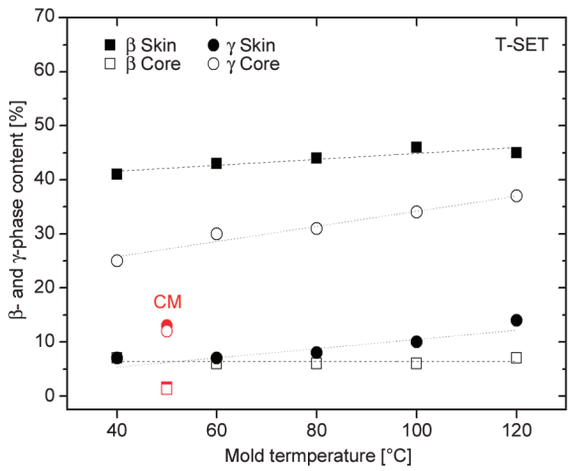

Figure 6. Dependence of β- and γ-phases content on the mold temperature during injection molding – T-SET and compression molding.

induced by flow at this temperature remains [45]. According to Janeschitz-Kriegl and coworkers [46, 47], there is a great amount of poorly organized aggregates of molecular chains that can form efficient nuclei only at quite low temperatures in a steady-state melt. But, the flow can support their growth. Thus, a great number of poor-quality sleeping nuclei are changed into better-quality nuclei, active at high temperatures in shear. Consequently, as the degree of supercooling decreases, the effect of flow on crystallization kinetics becomes more pronounced.

Figure 7 shows the changes in β- and γ-phase content as a function of holding pressure. An increase in holding pressure, from 30 to 70 MPa, results in a significant increase in the orthorhombic γ-phase, particularly in the core, where the growth is approximately 20% (from 17 to 37%). This positive effect of increasing

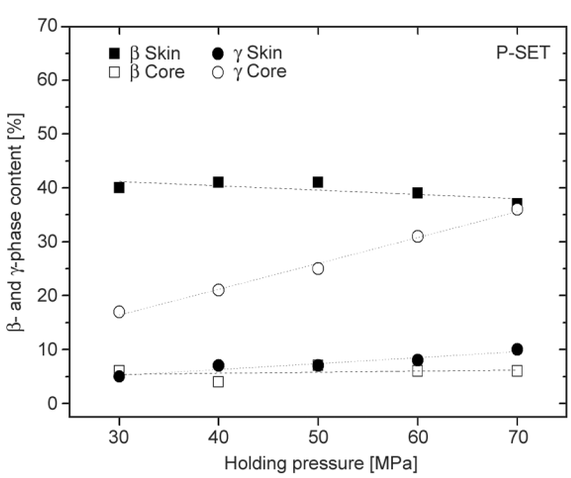

Figure 7. Dependence of β- and γ-phases content on the holding pressure – P-SET.

Table 2. The crystallinity of the specimens *vs*. mold temperature (T-SET), holding pressure (P-SET), injection speed (S-SET1, S-SET2), and compression molding (CM).

T-SET [°C]	Crystallinity [%]		P-SET [MPa]	Crystallinity [%]		S-SET1 [mm/s]	Crystallinity [%]		S-SET2 [mm/s]	Crystallinity [%]	
	Skin	Core		Skin	Core		Skin	Core		Skin	Core
40	70	67	20	69	66	20	70	71	30	72	68
60	70	68	50	66	67	50	69	65	40	71	67
80	71	68	80	70	67	80	70	67	50	71	67
100	71	66	110	67	65	110	69	66	60	70	65
120	71	67	140	66	65	140	67	69	70	72	64
CM	55	54									

pressure on γ-phase formation has also been observed by Navratilova *et al.* [26]. However, the effect of holding pressure within the range of 30–70 MPa on trigonal β-phase content is insignificant, with only a small decrease observed in the skin layer. This decrease may be attributed to a shortening of the crystallization time, whereby the previously mentioned α-nuclei created during melt flow can relax and result in competitive β-phase growth, which decreases with decreasing holding pressure [37].

Interesting results can also be observed in the case of specimens injection-molded at various injection speeds into molds tempered at 40 °C (Figure 8) and 120 °C (Figure 9). The highest increase in the trigonal β-phase content depending on injection speed and mold temperature can be observed in the skin layer. At low injection speeds (20 mm/s), the β-phase content reached 34% independent of mold temperature. As the injection speed increased, the β-phase content also increased, reaching up to 42% at 40 °C mold temperature and even up to 46% at 120 °C. These results are supported by the fact that the enhanced entanglement introduced by LCB prolongs the relaxation time of molecules after deformation. Hence, they can easily initiate the oriented core under shear flow and then give nucleation sites for β-crystal growth. The loosely coiled linear chains can be incorporated on the surface by the orientation of the induced nuclei and crystallize into a β-crystal [4, 37]. A higher mold temperature of 120 °C promoted β-phase formation up to 46% in the skin layer, while the content of β-phase in the core remains relatively low and independent of injection speed, with values of around 5 or 8% at mold temperatures of 40 and 120 °C, respectively. The formation of the orthorhombic γ-phase in the injection-molded specimens was not found to be significantly affected by the injection speed. However, the content of γ-phase was observed to increase with higher crystallization temperatures, reaching 15% in the skin and 35% in the core layer, as compared to 7 and 25%, respectively, at lower temperatures.

3.2. Charpy impact strength

The polymorphic composition of the individual specimens is reflected in their mechanical properties.

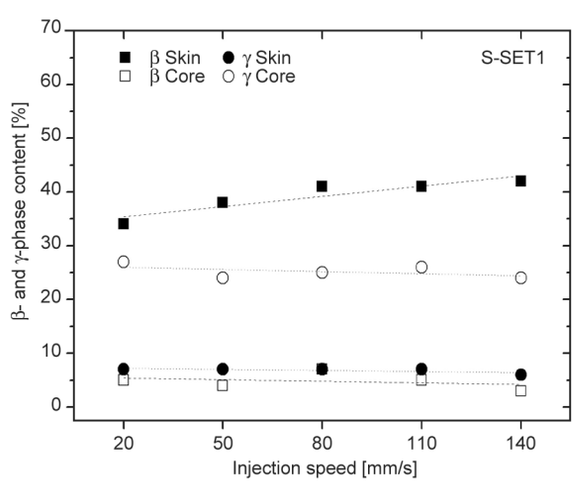

Figure 8. Dependence of β- and γ-phases content on the injection speed into the mold with the temperature of 40 °C – S-SET1.

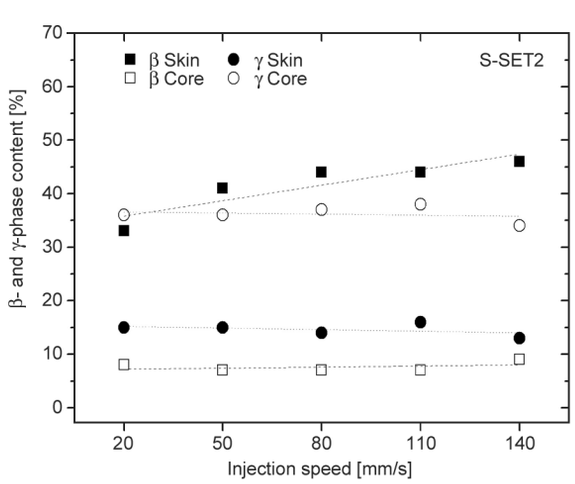

Figure 9. Dependence of β- and γ- phases content on the injection speed into the mold with the temperature of 120 °C – S-SET2.

The occurrence of the trigonal β-phase to a greater extent in the structure of polypropylene leads to a change in impact strength [19]. The impact performance of all specimens – injection-molded in various conditions and compression-molded is summarized in Figure 10. Compression-molded ones reach Charpy impact strength of 4.2 kJ/m^2. In the case of injection-molded specimens positive joint effect of mold temperature and injection speed on impact strength is evident. Increasing injection speed (from 20 to 140 mm/s) at 40 °C of mold temperature leads to an increase in impact strength of about 15% (from 3.8 to 4.4 kJ/m^2). At the same time, it is possible to observe a one-third increase in impact strength at all injection speeds with higher mold temperature (120 °C) – an increase in impact strength from 3.8 kJ/m^2 (mold temperature 40 °C) to 5.1 kJ/m^2 (120 °C) at 20 mm/s speed. Thus, the highest impact strength has been achieved in the specimens injection-molded at a speed of 140 mm/s at the mold temperature of 120 °C, which shows an impact strength of 5.7 kJ/m^2. The effect of holding pressure on the impact strength of the specimens has also been demonstrated – with increasing holding pressure from 30 to 70 MPa, the impact strength increased by 23% from 3.6 to 4.4 kJ/m^2.

Comparison of the results of polymorphic composition (Figures 6–9) and Charpy impact strength (Figure 10) clearly shows that impact strength is positively influenced by β-phase and simultaneously γ-phase content.

4. Conclusions

In the present paper, the impact of processing parameters, including mold temperature, injection speed, and holding pressure, on the supermolecular structure of long-chain branched polypropylene, as well as its impact strength, was investigated. Findings, based on data obtained through wide-angle X-ray scattering, demonstrated that injection speed, mold temperature, and holding pressure all have a significant impact on the polymorphic composition of LCB-PP specimens. Specifically, the joint effect of high injection speed and mold temperature led to the formation of trigonal β-phase in the skin layer. It was found that under shear flow, an oriented center can easily initiate, providing nucleation sites for β-crystal growth. Furthermore, prolonged relaxation times of LCBs after deformation contribute to the incorporation of loosely coined linear chains on the surface, which then orient the induced nuclei and crystallize into β-crystals. In contrast, it was found that growing holding pressure had a significant effect on the γ-phase, primarily in the core of the specimens. The higher content of γ-phase was promoted by higher mold temperature and holding pressure. The results also demonstrated that the polymorphic composition of the individual specimens was reflected in their impact strength. Interestingly, it was found that the co-existence of both β-phase and γ-phase had a favorable impact on the enhancement of impact strength. Overall, this study sheds new light on the importance of processing parameters in controlling

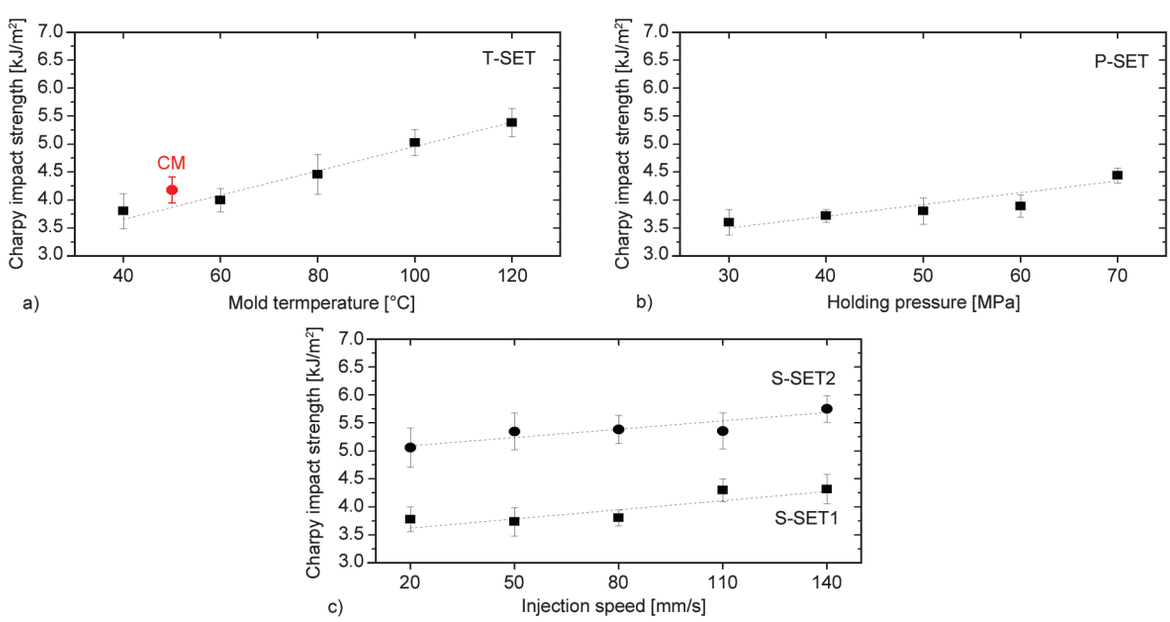

Figure 10. Variations of the Charpy impact strength for specimens processed at various conditions: a) T-SET and compression-molded (CM), b) P-SET, c) S-SET1 and S-SET2.

the supermolecular structure and impact strength of LCB-PP, which could have significant implications in the design and manufacture of polymeric materials.

References

[1] Somani R. H., Hsiao B. S., Nogales A., Fruitwala H., Srinivas S., Tsou A. H.: Structure development during shear flow induced crystallization of i-PP: *In situ* wide-angle X-ray diffraction study. Macromolecules, **34**, 5902–5909 (2001). https://doi.org/10.1021/ma0106191

[2] Kalay G., Bevis M. J.: Processing and physical property relationships in injection-molded isotactic polypropylene. 2. Morphology and crystallinity. Journal of Polymer Science Part B: Polymer Pysics, **35**, 265–291 (1997). https://doi.org/10.1002/(SICI)1099-0488(19970130)35:2<265::AID-POLB6>3.0.CO;2-R

[3] Varga J.: Supermolecular structure of isotactic polypropylene. Journal of Material Science, **27**, 2557–2579 (1992). https://doi.org/10.1007/BF00540671

[4] Sun H., Zhao Z., Yang Q., Yang L., Wu P.: The morphological evolution and β-crystal distribution of isotactic polypropylene with the assistance of a long chain branched structure at micro-injection molding condition. Journal of Polymer Research, **24**, 75 (2017). https://doi.org/10.1007/s10965-017-1234-3

[5] Huo H., Jiang S., An L., Feng J.: Influence of shear on crystallization behavior of the β phase in isotactic polypropylene with β-nucleating agent. Macromolecules, **37**, 2478–2483 (2004). https://doi.org/10.1021/ma0358531

[6] Zuo F., Keum J. K., Yang L., Somani R. H., Hsiao B. S.: Thermal stability of shear-induced shish-kebab precursor structure from high molecular weight polyethylene chains. Macromolecules, **39**, 2209–2218 (2006). https://doi.org/10.1021/ma052340g

[7] Zhang B., Chen J., Cui J., Zhang H., Ji F., Zheng G., Heck B., Reiter G., Shen C.: Effect of shear stress on crystallization of isotactic polypropylene from a structured melt. Macromolecules, **45**, 8933–8937 (2012). https://doi.org/10.1021/ma3014756

[8] Gahleitner M., Mileva D., Androsch R., Gloger D., Tranchida D., Sandholzer M., Doshev P.: Crystallinity-based product design: Utilizing the polymorphism of isotactic PP homo- and copolymers. International Polymer Processing, **31**, 618–627 (2016). https://doi.org/10.3139/217.3242

[9] Lotz B. A.: A new ε crystal modification found in stereodefective isotactic polypropylene samples. Macromolecules, **47**, 7612–7624 (2014). https://doi.org/10.1021/ma5009868

[10] Rieger B., Mu X., Mallin D. T., Chien J. C. W., Rausch M. D.: Degree of stereochemical control of racemic ethylenebis(indenyl)zirconium dichloride/methyl aluminoxane catalyst and properties of anisotactic polypropylenes. Macromolecules, **23**, 3559–3568 (1990). https://doi.org/10.1021/ma00217a005

[11] Chvátalová L., Navrátilová J., Čermák R., Raab M., Obadal M.: Joint effects of molecular structure and processing history on specific nucleation of isotactic polypropylene. Macromolecules, **42**, 7413–7417 (2009). https://doi.org/10.1021/ma9005878

[12] Lovinger A. J., Chua J. O., Gryte C. C.: Studies on the α and β forms of isotactic polypropylene by crystallization in a temperature gradient. Journal of Polymer Science: Polymer Physics Edition, **15**, 641 (1977). https://doi.org/10.1002/pol.1977.180150405

[13] Karger-Kocsis J., Varga J.: Effects of β-α transformation on the static and dynamic tensile behavior of isotactic polypropylene. Journal of Applied Polymer Science, **62**, 291–300 (1996). https://doi.org/10.1002/(SICI)1097-4628(19961010)62:2<291::AID-APP4>3.0.CO;2-S

[14] Somani R. H., Hsiao B. S., Nogales A., Srinivas S., Tsou A. H., Sics I., Balta-Calleja F. J., Ezquerra T. A.: Structure development during shear flow-induced crystallization of i-PP: *In-situ* small-angle X-ray scattering study. Macromolecules, **33**, 9385–9394 (2000). https://doi.org/10.1021/ma001124z

[15] Gajzlerova L., Navratilova J., Ryzi A., Slabenakova T., Cermak R.: Joint effects of long-chain branching and specific nucleation on morphology and thermal properties of polypropylene blends. Express Polymer Letters, **14**, 952–961 (2020). https://doi.org/10.3144/expresspolymlett.2020.77

[16] Varga J.: β-modification of isotactic polypropylene: Preparation, structure, processing, properties, and application. Journal of Macromolecular Science Part B, **41**, 1121–1171 (2002). https://doi.org/10.1081/MB-120013089

[17] Romankiewicz A., Sterzynski T., Brostow W.: Structural characterization of α- and β-nucleated isotactic polypropylene. Polymer International, **53**, 2086–2091 (2004). https://doi.org/10.1002/pi.1632

[18] Grein C.: Toughness of neat, rubber modified and filled β-nucleated polypropylene: From fundamentals to applications. in 'Intrinsic molecular mobility and toughness of polymers II' (ed.: Kausch H. H.) Vol. 188, 43–104 (2005). https://doi.org/10.1007/b136972

[19] Obadal M., Čermák R., Baran N., Stoklasa K., Simonik J.: Impact strength of β-nucleated polypropylene. International Polymer Processing, **19**, 35–39 (2004). https://doi.org/10.3139/217.1802

[20] Čermák R., Obadal M., Ponížil P., Polášková M., Stoklasa K., Lengálová A.: Injection-moulded α- and β-polypropylenes: I. Structure *vs*. processing parameters. European Polymer Journal, **41**, 1838–1845 (2005). https://doi.org/10.1016/j.eurpolymj.2005.02.020

[21] Navrátilová J., Čermák R., Obadal M., Verney V., Commereuc S.: Effect of β-nucleation on crystallization of photodegraded polypropylene. Journal of Thermal Analysis and Calorimetry, **95**, 215–220 (2009). https://doi.org/10.1007/s10973-008-8892-7

[22] Výchopňová J., Čermák R., Obadal M., Raab M., Verney V., Commereuc S.: The role of specific nucleation in polypropylene photodegradation. Polymer Degradation and Stability, **92**, 1763–1768 (2007). https://doi.org/10.1016/j.polymdegradstab.2007.07.010

[23] Obadal M., Čermák R., Raab M., Verney V., Commereuc S., Fraïsse F.: Study on photodegradation of injection-moulded β-polypropylenes. Polymer Degradation and Stability, **91**, 459–463 (2006). https://doi.org/10.1016/j.polymdegradstab.2005.01.046

[24] Thomann R., Wang C., Kressler J., Mülhaupt R.: On the γ-phase of isotactic polypropylene. Macromolecules, **29**, 8425–8434 (1996). https://doi.org/10.1021/ma951885f

[25] Hosier I. L., Alamo R. G., Esteso P., Isasi J. R., Mandelkern L.: Formation of the α and γ polymorphs in random metallocene–propylene copolymers. Effect of concentration and type of comonomer. Macromolecules, **36**, 5623–5636 (2003). https://doi.org/10.1021/ma030157m

[26] Navratilova J., Gajzlerova L., Kovar L., Cermak R.: Long-chain branched polypropylene: Crystallization under high pressure and polymorphic composition. Journal of Thermal Analysis and Calorimetry, **143**, 3377–3383 (2021). https://doi.org/10.1007/s10973-020-09931-1

[27] Morrow D. R., Newman B. A.: Crystallization of low-molecular-weight polypropylene fractions. Journal of Applied Physics, **39**, 4944–4950 (1968). https://doi.org/10.1063/1.1655891

[28] Hosier I. L., Alamo R. G., Lin J. S.: Lamellar morphology of random metallocene propylene copolymers studied by atomic force microscopy. Polymer, **45**, 3441–3455 (2004). https://doi.org/10.1016/j.polymer.2004.02.071

[29] Langston J. A., Colby R. H., Chung T. C. M., Shimizu F., Suzuki T., Aoki M.: Synthesis and characterization of long chain branched isotactic polypropylene *via* metallocene catalyst and T-reagent. Macromolecules, **40**, 2712–2720 (2007). https://doi.org/10.1021/ma062111+

[30] Zhang X., Wang X., Huang J., Xia Z.: Quasi-static and dynamic piezoelectric d_{33} coefficients of irradiation cross-linked polypropylene ferroelectrets. Journal of Materials Science, **44**, 2459–2465 (2009). https://doi.org/10.1007/s10853-009-3312-3

[31] Zhang Z. J., Wan D., Xing H. P., Zhang Z. J., Tan H. Y., Wang L., Zheng J., An Y. J. Tang T.: A new grafting monomer for synthesizing long chain branched polypropylene through melt radical reaction. Polymer, **53**, 121–129 (2012). https://doi.org/10.1016/j.polymer.2011.11.033

[32] Wang K., Wang S., Wu F., Pang Y., Liu W., Zhai W., Zheng W.: A new strategy for preparation of long-chain branched polypropylene *via* reactive extrusion with supercritical CO_2 designed for an improved foaming approach. Journal of Materials Science, **51**, 2705–2715 (2016). https://doi.org/10.1007/s10853-015-9584-x

[33] Su Z., Wang H., Dong J., Zhang X., Dong X., Zhao Y., Yu J., Han C. C., Xu D., Wang D.: Conformation transition and crystalline phase variation of long chain branched isotactic polypropylenes (LCB-iPP). Polymer, **48**, 870–876 (2007). https://doi.org/10.1016/j.polymer.2006.12.013

[34] Tian J., Yu W., Zhou C.: Crystallization behaviors of linear and long chain branched polypropylene. Journal of Applied Polymer Science, **104**, 3592–3600 (2007). https://doi.org/10.1002/app.26024

[35] McCallum T. J., Kontopoulou M., Park C. B., Muliawan E. B., Hatzikiriakos S. G.: The rheological and physical properties of linear and branched polypropylene blends. Polymer Engineering and Science, **47**, 1133–1140 (2007). https://doi.org/10.1002/pen.20798

[36] Nam G. J., Yoo J. H., Lee J. W.: Effect of long-chain branches of polypropylene on rheological properties and foam-extrusion performances. Journal of Applied Polymer Science, **96**, 1793–1800 (2005). https://doi.org/10.1002/app.21619

[37] Zhou S., Wang W., Xin Z., Zhao S., Shi Y.: Relationship between molecular structure, crystallization behavior, and mechanical properties of long chain branching polypropylene. Journal of Materials Science, **51**, 5598–5608 (2016). https://doi.org/10.1007/s10853-016-9856-0

[38] Wang L., Ishihara S., Ando M., Minato A., Hikima Y., Ohshima M.: Fabrication of high expansion microcellular injection-molded polypropylene foams by adding long-chain branches. Industrial and Engineering Chemistry Research, **55**, 11970–11982 (2016). https://doi.org/10.1021/acs.iecr.6b03641

[39] Obadal M., Čermák R., Stoklasa K: Tailoring of three-phase crystalline systems in isotactic poly(propylene). Macromolecular Rapid Communications, **26**, 1253–1257 (2005). https://doi.org/10.1002/marc.200500272

[40] Turner-Jones A., Aizlewood J. M., Beckett D. R.: Crystalline forms of isotactic polypropylene. Macromolecular Chemistry and Physics, **75**, 134–158 (1964). https://doi.org/10.1002/macp.1964.020750113

[41] Sauer J. A., Pae K. D.: Structure and thermal behavior of pressure-crystallized polypropylene. Journal of Applied Physics, **39**, 4959–968 (1968). https://doi.org/10.1063/1.1655893

[42] Varga J., Karger-Kocsis J.: Rules of supermolecular structure formation in sheared isotactic polypropylene melts. Journal of Polymer Science Part B: Polymer Physics, **34**, 657–670 (1996). https://doi.org/10.1002/(SICI)1099-0488(199603)34:4<657::AID-POLB6>3.0.CO;2-N

[43] Zhao W., Huang Y., Liao X., Yang Q.: The molecular structure characteristics of long chain branched polypropylene and its effects on non-isothermal crystallization and mechanical properties. Polymer, **54**, 1455–1462 (2013). https://doi.org/10.1016/j.polymer.2012.12.073

[44] Wood-Adams P. M., Dealy J. M., deGroot A. W., Redwine O. D.: Effect of molecular structure on the linear viscoelastic behavior of polyethylene. Macromolecules, **33**, 7489–7499 (2000). https://doi.org/10.1021/ma991533z

[45] Liu Q., Sun X., Li H., Yan S.: Orientation-induced crystallization of isotactic polypropylene. Polymer, **54**, 4404–4421 (2013). https://doi.org/10.1016/j.polymer.2013.04.066

[46] Janeschitz-Kriegl H., Ratajski E., Stadlbauer M.: Flow as an effective promotor of nucleation in polymer melts: A quantitative evaluation. Rheologica Acta, **42**, 355–364 (2003). https://doi.org/10.1007/s00397-002-0247-x

[47] Janeschitz-Kriegl H.: A recollection with respect to flow induced crystallization in polymer melt processing. International Polymer Processing, **32**, 227–236 (2017). https://doi.org/10.3139/217.3331

Express Polymer Letters Vol.17, No.10 (2023) 1042–1055
Available online at www.expresspolymlett.com
https://doi.org/10.3144/expresspolymlett.2023.78

Research article

Synthesis and evaluation of poly(isoprene-*co*-acrylonitrile) as synthetic rubber with enhanced oil resistance

*Zhen Hern Boon, Yin Yin Teo, Desmond Teck-Chye Ang**

Department of Chemistry, Universiti Malaya, 50603 Kuala Lumpur, Malaysia

Received 20 March 2023; accepted in revised form 11 July 2023

Abstract. Increasing demand for durable rubber and rapid advancement in the automotive sector has made oil-resistant rubber an increasingly important material. Among them, nitrile rubber (NBR) is the most iconic due to its extraordinary oil resistance contributed by the polar nitrile pendant groups. Synthesis of NBR, however, is highly hazardous due to the explosive nature of the gaseous monomer butadiene. In this work, poly(isoprene-*co*-acrylonitrile) (NIR) was synthesized using free radical emulsion polymerization, with liquid monomer isoprene as the diene in the rubber formulation. The spectroscopic analysis confirmed the formation of NIR and indicated that the polymerized isoprene in the rubber is predominantly of 1,4-microstructure. A series of rubbers with different contents of acrylonitrile were produced and the mechanical, thermal, as well as oil resistant property of the resultant rubber films were evaluated. Vulcanized NIR films displayed glass transition temperatures from –9.4 to 20.2 °C, suggesting that the polymers are rubbery at ambient and higher temperatures. The NIR rubber films exhibited excellent oil resistance with less than 2% swelling in mineral oil, good thermal stability with onset degradation temperature in the range of 361.3 to 369.9 °C, and adequate mechanical strength from 1.61 to 8.23 MPa. The synthesized NIR rubber has the potential to serve as an alternative to NBR which had been traditionally used for oil resistance applications.

Keywords: *elastomer, synthetic rubber, thermal degradation, radical polymerization, tensile testing, oil resistance*

1. Introduction

Rubbers are generally amorphous polymeric materials categorized as elastomers [1]. Depending on the origin, rubbers can be divided into natural rubber (NR) and synthetic rubber. NR is obtained from the coagulation of latex in rubber trees, and *Hevea brasiliensis* is the current dominant species for natural rubber production [2, 3], while synthetic rubber refers to those which were synthesized from monomers. Although the monomers used in rubber synthesis were mostly petroleum-derived, there are, however increasing number of initiatives to produce bio-based synthetic rubbers utilizing materials that were sourced naturally [4, 5]. According to a report by the International Rubber Study Group, the world consumption of natural and synthetic rubbers in the year 2021 was reported at 13.77 million metric tons and 15.81 million metric tons, respectively. The consumption of both rubbers is forecasted to increase by 2.8 and 2.9%, respectively, in the year 2023, and the total rubber demand is expected to grow on an average of 2.4% per annum until the year 2031. The high volume of rubber consumption is a result of a wide range of applications of rubber in various fields.

Although NR is irreplaceable in terms of mechanical strength due to its exceptionally high molecular weight, good fatigue resistance and ability to undergo stress crystallization [3, 6, 7], NR's lack of resistance to strong sunlight, oxidative and oily environment, as well as inconsistent supply of global NR stock had made the shift to synthetic rubber inevitable [2, 3, 8, 9]. Synthetic rubbers provide an extended

*Corresponding author, e-mail: desmond860108@um.edu.my
© BME-PT

range of applications on top of the applications of NR. The chemical structure of synthetic rubber can be varied using different amounts and combinations of monomers, resulting in rubbers with a vast range of properties. For example, nitrile-butadiene rubber (NBR), more commonly called nitrile rubber, is obtained through emulsion polymerization of butadiene and acrylonitrile. The most significant characteristic of NBR is its excellent oil resistance contributed by the polar nitrile group [10]. Commonly, the acrylonitrile content (ACN content) in NBR ranges from 18 to 50%, and the oil resistance property improves with the increase in ACN content [3, 10]. ACN content in NBR can also be used to tailor other properties such as mechanical properties, glass transition temperature, T_g, and processability of the rubber [3]. The presence of polar nitrile groups resists the penetration of non-polar oils into the rubber structure, resulting in lesser swelling, and allows the rubber to retain its original properties and dimensions when in contact with oil. This makes nitrile rubber an excellent material for applications such as O-rings, gaskets, and hoses in the automotive, aeronautical, oil and gas industry [11]. Besides oil-sealing purposes, NBR was also exploited to produce nitrile gloves, especially after increased public awareness about latex protein allergy from natural rubber latex gloves. Wider chemical resistance coverage, higher puncture resistance, and aging resistance are some of the additional features that make nitrile disposable gloves preferred in the medical sector, laboratories, and food industries [11, 12].

Whilst NBR is an important synthetic rubber, production of the rubber could be a highly challenging ordeal. Butadiene or 1,3-butadiene is a 4-carbon conjugated diene that is used in the synthesis of nitrile rubber. It is a colorless gas that is commercially produced through steam cracking of crude oil [13]. In addition to the extra setups necessary to operate a gaseous monomer, the production of NBR is relatively risky due to the flammability and explosive nature of butadiene when mixed with air. Incidents of fire and explosion at processing facilities related to butadiene could happen even with slight negligence. There were several reported cases in recent years, such as a chemical plant explosion in Port Neches, Texas, on November 2019, an explosion and fire at an emulsion styrene-butadiene rubber production plant in Poland on January 2021, and a major fire at a butadiene rubber plant in Malaysia on February 2022. It is therefore necessary to explore alternative diene, which is easier and less risky to operate for the production of synthetic rubber with properties similar to that of NBR, specifically its superior oil resistance.

Isoprene or 2-methyl-1,3-butadiene, is a 5-carbon conjugated diene that is widely used in the rubber industry. Isoprene is the main constituent of NR and synthetic polyisoprene (PIP). It is also used in other synthetic rubbers, such as butyl rubber (IIR) and styrene-isoprene block copolymers (SIS) [3]. Isoprene can be polymerized through various techniques, including anionic, cationic, free radical and coordination polymerizations. The coordination polymerization using Ziegler-Natta catalysts is preferred in the industrial synthesis of PIP due to the ability to produce high *cis*-1,4-polyisoprene content, enabling the rubber to exhibit properties similar to NR [3, 14]. The polymerization of isoprene is often investigated and compared alongside butadiene. This is because they are considered close analogous conjugated dienes due to their similarity in chemical structure, oftentimes resulting in similar polymerization kinetics [15, 16]. Some recent research on the polymerization of isoprene is focused on the emulsion polymerization with the objectives of improving the polymerization rate and yield, as conventional emulsion polymerization of isoprene had low yield due to low propagation rate, high termination, and side reactions [16, 17]. Different initiator systems in the emulsion polymerization of PIP were investigated by Cheong *et al.* [18] in 2004. They found the redox initiator systems allowed the low-temperature polymerization temperature at 25 °C, resulting in higher yield polymerization and produced PIP with negligible gel content. Chouytan *et al.* [19] reported the improvement in monomer conversion in miniemulsion polymerization of isoprene by controlling the ratio of surfactant-to-monomer concentration, causing an increase in number of stabilized emulsion droplets and thus the loci for polymerization reaction.

In view of the need to overcome the limitation of butadiene in nitrile rubber formulation and the lack of potential alternatives to NBR, this work details the development of poly(isoprene-*co*-acrylonitrile), NIR as a new synthetic rubber with excellent oil resistance. No gaseous monomers were used in the synthesis, and isoprene, which is a liquid diene monomer at ambient temperature, was used to produce the rubber emulsion in a simple one-pot synthesis setup.

The nitrile content of the rubber varied from 20 to 35 mol%, and the resultant properties of the emulsion and rubber films were evaluated. The chemical structure of the rubber was characterized using Fourier transform infrared spectroscopy (FTIR) and proton nuclear magnetic resonance (^{1}H-NMR), while mechanical properties and oil resistance tests were conducted on the vulcanized rubber films.

2. Experimental

2.1. Materials

Synthesis grade isoprene (CAS: 78-79-5) and acrylonitrile (CAS: 107-13-1) were obtained from Merck (Germany). Analysis grade potassium peroxodisulfate ($K_2S_2O_8$, CAS: 7727-21-1), sodium dithionite ($Na_2S_2O_4$, CAS: 7775-14-6), sodium hydroxide (NaOH) pellets (CAS: 1310-73-2) and 28–30% ammonia solution (CAS: 1336-21-6) were obtained from Merck (Germany). Isooctyl 3-mercaptopropionate (≥99%, CAS: 30374-02-7), technical grade sodium dodecylbenzenesulfonate (SDBS, CAS: 25155-30-0) and chloroform-D ($CDCl_3$) (99.8 atom% D, contains 0.03 v/v% tetramethylsilane (TMS), CAS: 865-49-6) were obtained from Sigma Aldrich (Germany). Total Quartz 5000 Future 10W-30 mineral-based engine oil was obtained from Total Oil Asia-Pacific Pte Ltd, Singapore. 50 wt% zinc dithiocarbamates (ZDBC) dispersion, 60 wt% zinc oxide (ZnO) dispersion, and 60 wt% sulphur dispersion were obtained from Aquaspersions (M) Sdn Bhd. NBR latex was purchased from Crucial (M) Sdn. Bhd. The properties of NBR used is given in Table 1. All chemicals involved in this work were used as received except for isoprene and acrylonitrile, which both were washed with 10 wt% NaOH solution and distilled water to remove inhibitors prior to usage.

2.2. Synthesis of poly(isoprene-*co*-acrylonitrile) emulsion

A series of poly(isoprene-*co*-acrylonitrile) (NIR) rubber varying in ACN content were synthesized through emulsion polymerization, and the formulations are given in Table 2. The methodology of emulsion polymerization for NIR rubber was adapted from [20, 21]. Codename NIR20 was given to NIR with 20 mol% ACN content, and the same codename format is applicable for NIR30 and NIR35. The highest ACN content in this work was fixed at 35%, as excessively high nitrile content in NIR leads to stiffer material with reduced elasticity. The polymerization was carried out at 65–70 °C in a 2 l reaction flask while being constantly stirred at 60–80 rpm with an overhead stirrer. A double condenser system attached to cold water supply was used to increase the condensation efficiency of low boiling point isoprene and enable the collection of condensates at the end of the second condenser, which was then reintroduced back into the reaction flask throughout the synthesis. The reaction setup is shown in Figure 1. SDBS was dissolved in distilled water bubbled with nitrogen gas, adjusted to pH 7–9 with ammonia solution, and then transferred to the reaction flask. The initiator, $K_2S_2O_8$, was dissolved in 200 ml of distilled water, while the activator, $Na_2S_2O_4$, was dissolved in 100 ml of distilled water. The initiator and activator solution were premixed and the mixture was then added dropwise into the flask over a period of 12 h, while the monomers mixture was added dropwise concurrently over the first 8 h. Chain transfer agent (CTA) isooctyl 3-mercaptopropionate was added into the mixture starting from the second half of the monomer addition. At the end of the synthesis, the pH of the mixtures was adjusted to pH 9–10 to preserve the stability of the emulsion.

Table 1. Properties of NBR.

Property		Quantity
Total solid content, *TSC*	[%]	45
Nitrile content	[%]	<30
Molecular weight	[·10^5 kDa]	1.45
Viscosity at 25±2 °C	[mPa·s]	38
pH		8.2

2.3. Characterization of rubber emulsions

The total solid content (*TSC*) of the rubber emulsions was measured according to ASTM D1417. A clean, dry aluminum foil dish was weighed (m_1), and approximately 2 ml of rubber emulsion was transferred

Table 2. NIR rubber formulations.

Ingredient	Formulation [g]		
	NIR20	NIR30	NIR35
Isoprene	272.500	238.400	221.400
Acrylonitrile	53.060	79.590	92.860
$K_2S_2O_8$	4.866	4.866	4.866
$Na_2S_2O_4$	3.134	3.134	3.134
CTA	4.883	4.770	4.714
SDBS	17.360	17.000	16.820
Water	308.700	296.700	290.700

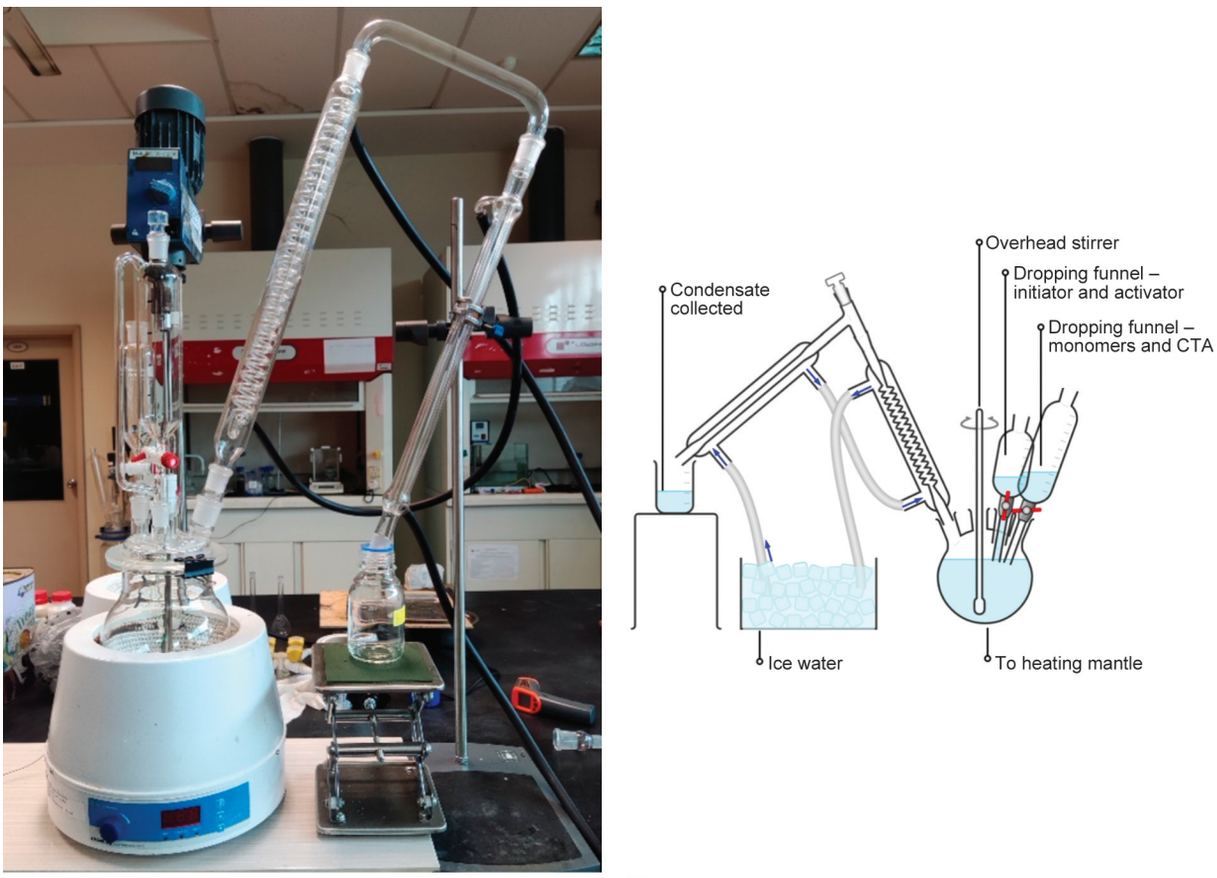

Figure 1. Apparatus setup for emulsion polymerization of NIR a) actual setup, and b) schematic diagram.

to the aluminum foil dish with a dropper and weighed (m_2). The aluminum foil dish with rubber emulsion was then heated in an oven at 170 °C for 15 min before it was removed and cooled in a desiccator. After reaching room temperature, the aluminum foil dish was weighed (m_3). *TSC* was calculated according to Equation (1):

$$TSC\,[\%] = \frac{m_3 - m_1}{m_2 - m_1} \cdot 100 \tag{1}$$

The particle size (Z-average diameter) and zeta potential of the emulsions were measured using Malvern Zetasizer NanoZS at 25 °C. Folded capillary cells D*TS*1070 were used in both measurements. The emulsion was first diluted with distilled water before analysis to weaken the scattering signal and improve the accuracy of the analysis. The viscosity of the rubber emulsions was measured using NDJ-1 digital rotary viscometer. The solid content of all emulsions was adjusted and standardized to 30 w/w% before measurement, and Rotor #1 at a spindle velocity of 60 rpm was used. The viscosity reported was from the average of 3 readings. Molecular weight measurement was carried out utilizing the static light scattering technique. A series of rubber emulsions with different concentrations were prepared through dilution with distilled water. The scattering intensities were measured using Malvern Zetasizer NanoZS at a wavelength of 632.8 nm, scattering detection angle of 173°, and temperature of 25 °C. Distilled water was used as the scattering standard and the refractive index increment (d_n/d_c) was 0.118. The molecular weight was determined from the Debye plot.

2.4. Compounding and preparation of NIR film

Compounding of the rubber emulsions was done through the addition of 2 parts per hundred parts dried rubber [phr] ZnO, 1 phr ZDBC, 1 phr sulphur and 0.5 phr ammonia solution per 100 phr NIR rubber. The mixture was stirred at high-speed using an overhead stirrer overnight, and the mixture was left for another day for maturation. The pH of the mixture was adjusted to 9–10 after compounding. Rubber film was prepared through solution casting in Petri dishes. The amount of emulsion introduced into each petri dish was calculated based on the *TSC* of the rubber emulsion. It is necessary to ensure that a comparable

amount of rubber in each dish so that uniform and comparable film thickness can be obtained across different casted films. The Petri dishes were then dried in the fume hood overnight, followed by thorough drying in a thermal oven at 120 °C. The same formulation and compounding procedure was used to prepare NBR film for comparison purposes.

2.5. Characterization of rubber film

2.5.1. Spectroscopic characterization

Fourier transform infrared (FTIR) spectra of the rubber films were recorded using Attenuated Total Reflectance (ATR)-Perkin Elmer Frontier FTIR spectrometer in the region 550 to 4000 cm^{-1} at the resolution of 4 cm^{-1}. The spectrum recorded was from an average of 16 scans. The ^{1}H-NMR spectra of rubber films dissolved in $CDCl_3$ were recorded using JEOL ECX-400 FT-NMR spectrometer with traces of TMS present in the deuterated solvent to produce an internal reference signal at 0 ppm. It is noteworthy that spectroscopic analyses were conducted on uncompounded rubber films to avoid interference from the compounding ingredients.

2.5.2. Thermal analysis

Calorimetric analysis was done using the TA Instruments DSC Q20 differential scanning calorimeter (DSC) to determine the T_g of the rubber films. The temperature scan rate was 10 °C/min in the temperature range from –40 to 100 °C, and the nitrogen gas flow rate was at 200 ml/min. Thermogravimetric analysis (TGA) of the rubber films was carried out using Perkin Elmer TGA4000 with the temperature scan rate 10 °C/min in the temperature range from 30 to 900 °C.

2.5.3. Mechanical testing

A tensile test was carried out according to ASTM D412. Dumbbell-shaped rubber film with narrow section having 4 mm width, 10 mm length, and 1 mm thick were cut from the casted rubber films. The instrument used for the test was Shimadzu AG-5kNX Universal Tester with a crosshead speed of 500 mm/min. A tear strength test was carried out according to ASTM D624. Unnicked 90° sample was stretched using the same instrument and crosshead speed as the tensile test mentioned above. Ultimate tensile strength (*TS*), elongation at break (*EB*), modulus at 100% strain (*M100*), and tear strength (T_s) were determined and reported from the average of 3 repetitions.

2.5.4. Oil resistance test

The oil resistance test of the rubber films was carried out according to ASTM D471. Total Quartz 5000 Future 10W-30, a commonly used mineral-based engine oil, was used to test the oil resistance of the rubber. NR film was included in this test together with NIR and NBR samples for comparison purposes. Rectangular samples having a dimension of 25 mm width, 50 mm length, and 0.3 mm thickness were weighed (m_4) and hung on a self-made hanger using aluminum wire. The cut rubber samples were immersed in 100 cm^3 of testing oil for 72 h in the dark at room temperature (26±2 °C), 70±2 and at 100±2 °C. After the immersion period, the samples immersed at elevated temperature were cooled down to room temperature by transferring them into cool clean portion of the engine oil for 30–60 min. The samples were then dipped quickly in acetone and blotted lightly with lint-free filter paper before being weighed (m_5). The change in the mass of the sample was used to calculate the percentage swelling, which reflects the oil resistance of the rubber (Equation (2)):

$$\text{Percentage swelling}\,[\%] = \frac{m_5 - m_4}{m_4} \cdot 100 \qquad (2)$$

The changes in the dimension (length, width, and thickness) of the rubber films from the oil immersion were measured as well. The changes in dimension and percentage swelling were calculated individually, and a repetition of 3 samples was carried out for each type of rubber.

3. Result and discussion

3.1. Characterization of rubber emulsions

The visual appearance of NIR emulsions and NBR commercial latex is shown in Figures 2a and 2b. They were milky white with no noticeable visual difference between all emulsions. The physical appearance of all the rubber films, as shown in Figure 2c, was similar too, where they are all yellowish white in color. The stability of the emulsions was investigated using particle size and zeta potential analyses, and the result is tabulated in Table 3, while the particle size distribution curve of all the rubber emulsions is shown in Figure 3. All the NIR emulsions recorded small particle sizes, in the range of 90–122 nm, comparable

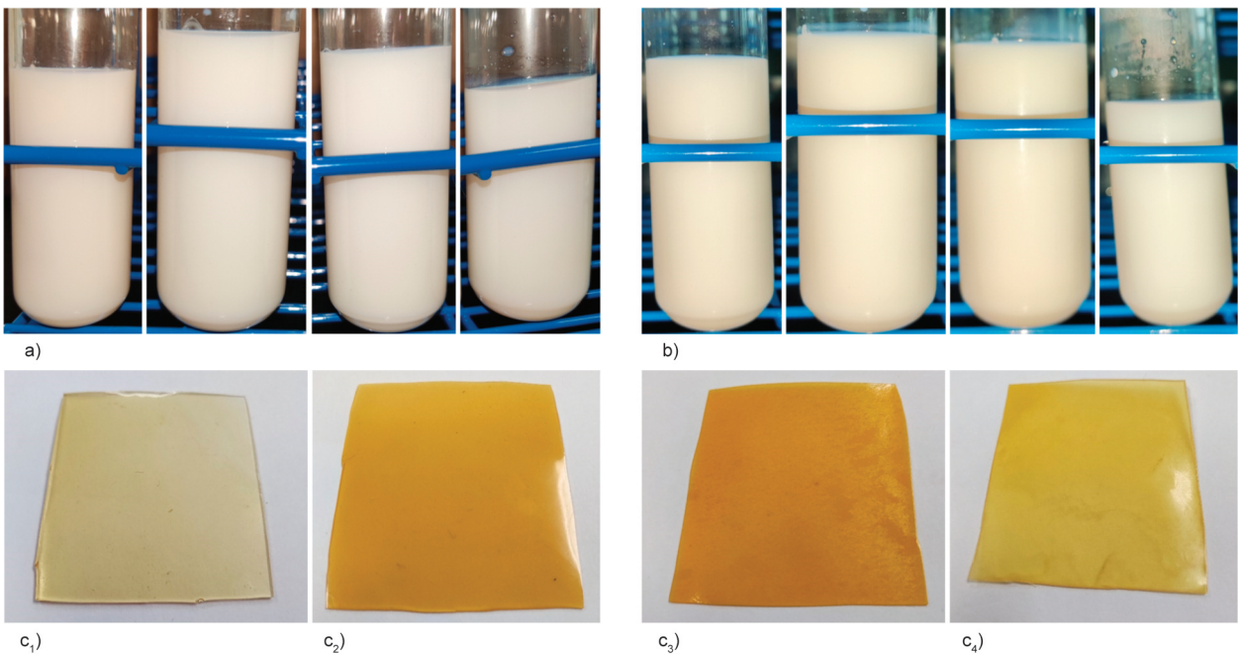

Figure 2. Physical appearance of rubber emulsions a) at freshly prepared, b) after 6 months storage (from left to right: NBR, NIR20, NIR30, NIR35), and c) vulcanized rubber films (c_1) NBR, c_2) NIR20, c_3) NIR30, c_4) NIR35).

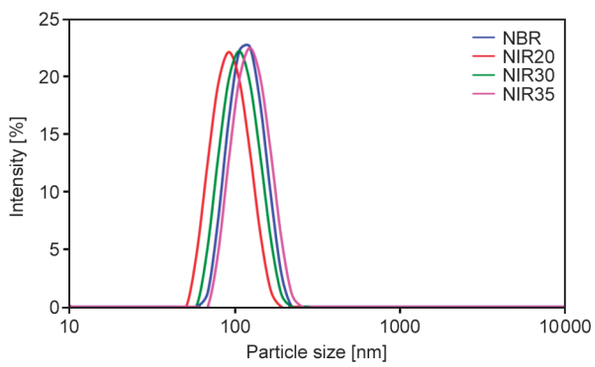

Figure 3. Particle size distribution curves of rubber emulsions.

to that of commercial NBR at 114 nm. Emulsion with smaller dispersed particle sizes was reported to be more stable as more particles can be distributed on the interface of the emulsion [22, 23]. All the NIR emulsions particles were also found to be narrowly distributed in size (monodisperse), which was evidenced by the low polydispersity index of less than 0.07 [24]. The Zeta potential of an emulsion can also be used to evaluate the stability of an emulsion, with those recording potential greater than |30 mV| usually considered sufficiently stable due to the strong electrostatic repulsion between the particles [25, 26]. NIR20 and NIR30 recorded high negative zeta potential exceeding –60 mV, while NIR35 had comparable zeta potential as the NBR at about –50 mV. The results imply that the synthesized emulsions were strongly anionic in nature and stable enough for long-term storage. The stability of the emulsions is also evidenced by the unnoticeable change in appearance after 6 months of storage, as shown in Figure 2b. The *TSC* of the NIR lattices produced was slightly less than 30%, and the concentration of all the lattices was adjusted to a uniform concentration of 30% *TSC* prior to viscosity measurement and film casting. It is noteworthy that the concentration of latex can be adjusted, for example, by removing water from the system or via centrifugation to obtain the desired concentration to suit the types of subsequent fabrication processes such as coagulant dipping, film casting, *etc*. The viscosity of all the emulsions was comparable at 5.6±0.2 mPa·s, suggesting that the molecular weight of the rubber in the emulsions may not differ significantly [27]. The molecular weight of

Table 3. Properties of NIR and NBR rubber emulsions.

Sample	Particle size [nm]	Polydispersity index	Zeta potential [mV]	Viscosity [mPa·s]	Molecular weight [·10^5 kDa]
NIR20	90.7	0.039	–63.3	5.44	3.44
NIR30	104.2	0.045	–61.0	5.44	1.53
NIR35	122.0	0.069	–50.1	5.58	0.91
NBR	113.7	0.044	–51.8	5.81	1.45

the rubber obtained from the light scattering analysis was recorded in Table 3, and NIR30 had the closest molecular weight to the commercial NBR.

3.2. Characterization of rubber films

3.2.1. Spectroscopic analysis

The FTIR spectrum of all samples is represented in Figure 4. The band at 1378 cm^{-1} represents the $–CH_3$ bending from the *cis*-1,4-polyisoprene unit, while bands that represent other microstructures, such as 890 cm^{-1} from $=CH_2$ bending of 3,4-unit and 911 cm^{-1} from $=CH_2$ bending of 1,2-unit are either very weak or not observed at all [28, 29]. It was reported that isoprene may undergo polymerization to produce 4 isomers, namely the 3,4-addition polymer, 1,2-addition polymer, *cis*-1,4 and *trans*-1,4 polyisoprene [3]. The structures of all 4 isomers are given in Figure 5. Considering that the bands of other isomers are not apparent, it could be implied that the NIR rubbers are made of predominantly 1,4 units, consistent with the results reported by others on emulsion polymerization of isoprene [17]. The band at 2250 cm^{-1} was assigned to the stretching of the nitrile group (–CN), and the intense band at 1440 cm^{-1} was assigned to the bending vibration of the methylene group ($–CH_2–$). The ratio of these two bands

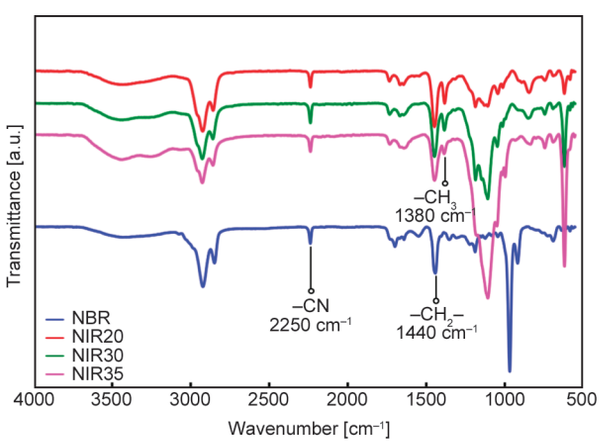

Figure 4. FTIR spectrum of NIR and NBR films.

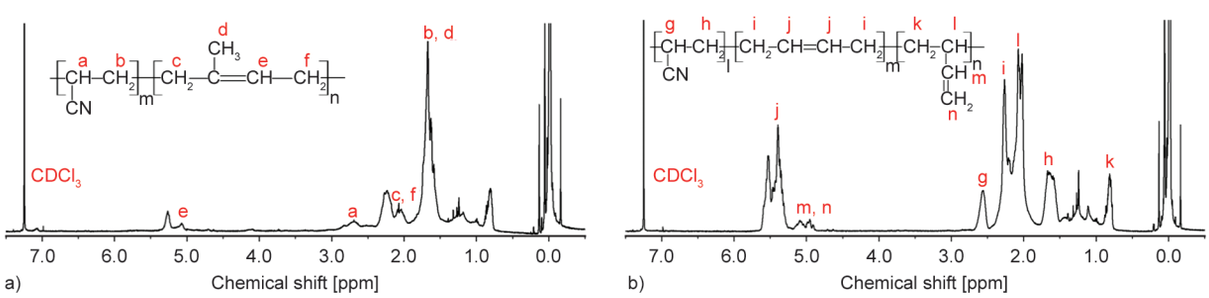

Figure 6. ^{1}H-NMR spectra of a) NIR30 and b) NBR.

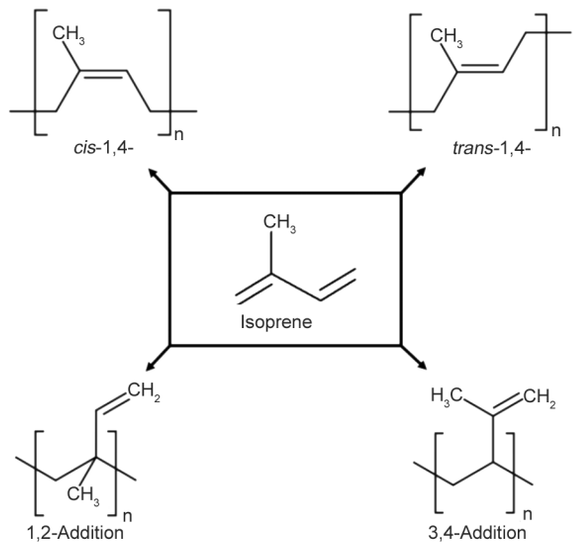

Figure 5. Chemical structure of isoprene and the respective polymerization isomers.

area, A_{2250}/A_{1440} reflects the relative amount of nitrile group present in the rubber, and values are tabulated in Table 4. The A_{2250}/A_{1440} value increased in the order of NIR20, NIR30 to NIR35, and this was well within expectation and consistent with the ACN content in the NIR rubber formulation (Table 2). The band area ratio for the NBR sample was close to those of NIR20 and NIR30, agreeing with the low nitrile grade of the NBR (Table 1).

Figure 6a shows the ^{1}H-NMR spectrum of NIR30. The chemical shift assignments are ($CDCl_3$; δ, ppm), 5.07 (=CH–, 1,4 unit) and 2.69 (CHCN, ACN). Other peaks at 2.07 and 1.67 ppm are from the resonance of protons attached to various groups, as labeled in the

Table 4. FTIR absorbance band area.

Sample	Band area		
	A_{2250}	A_{1440}	A_{2250}/A_{1440}
NIR20	64.47	499.4	0.129
NIR30	78.04	531.1	0.147
NIR35	138.70	574.2	0.242
NBR	85.55	549.1	0.156

figure. Consistent with the FTIR analysis, ^{1}H-NMR spectra of the NIR rubbers suggest that the polymer does not contain 1,2- and 3,4-microstructure units. From the ^{1}H-NMR spectrum of NBR in Figure 6b, the chemical shift assignments are (CDCl ; δ, ppm), 5.394 (=CH–, 1,4-unit), 4.953 (=CH–, 1,4-unit and $=CH_2$, 1,2-unit), 2.568 (CHCN, ACN), 2.266 ($–CH_2–$, 1,4-unit), 2.058 (>CH–, 1,2-unit), 1.639 ($–CH_2$, ACN) and 0.820 ($–CH_2–$, 1,2-unit). Like isoprene, butadiene could undergo polymerization to produce several isomers, which includes the 1,4- and 1,2-addition polymer. From the ^{1}H-NMR spectrum, it showed that the NBR contained both the isomers of polymerized butadiene.

3.2.2. Thermal analysis

DSC thermograms of the rubber films in Figure 7 show that the T_g values of NIR are –9.4 °C for NIR20, 6.2 °C for NIR30, and 20.2 °C for NIR35. T_g of NIR shifted towards higher temperatures with increasing ACN content in the rubber. At high loading of ACN, there are more nitrile groups in the rubber to yield stronger dipolar interaction, which could restrict the movement of rubber chains, and consequently increases the T_g of the rubber film. Because of the strong dipolar interaction between the nitrile groups, pure poly(acrylonitrile) is a brittle plastic with T_g around 85–110 °C, and acrylonitrile is regarded as a hard monomer. Linear poly(isoprene) with high 1,4-units, on the other hand, reported T_g of about –70 °C [19, 30, 31]. Considering that NIR is produced from the copolymerization of both the soft and hard monomers, it is reasonable to expect the T_g of the resultant NIR rubber to lie between those of poly(acrylonitrile) and poly(isoprene). Typical T_g of NBR was reported to be from –38 °C in 18% ACN content up to –2 °C in 50% ACN content [32, 33]. Overall, the T_g of NIR in this work lies within the expected region, albeit slightly higher than that of NBR. More importantly, the T_g of the rubbers, especially NIR20 and NIR30 are well below room temperature, enabling them to remain rubbery at ambient operating temperature, while NIR35, which recorded relatively high T_g, behaved more like plastic.

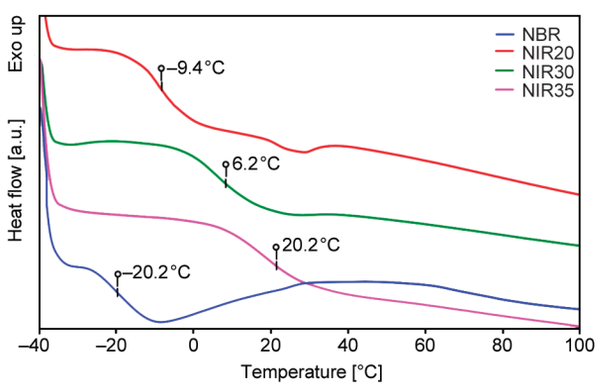

Figure 7. DSC curves of NIR and NBR.

TGA was used to determine the decomposition behavior and thermal stability of the rubber. TGA and DTG curves of all samples are shown in Figure 8. The temperature at 10% weight loss (T_{90}) was used to compare the thermal stability of the rubber samples, and the temperatures recorded for NIR20, NIR30, and NIR35 were 361.3, 366.2, 369.9 °C, respectively. The thermal stability of NIR increased with increasing ACN content, and the same trend was reported by Lee and Ha [34] on the effect of ACN content on the thermal stability of NBR. The increase in thermal stability of the NBR was attributed to the higher decomposition temperature of the nitrile unit compared to the butadiene. This could be the result of the higher energy required to break the strong dipolar interaction contributed by the nitrile group

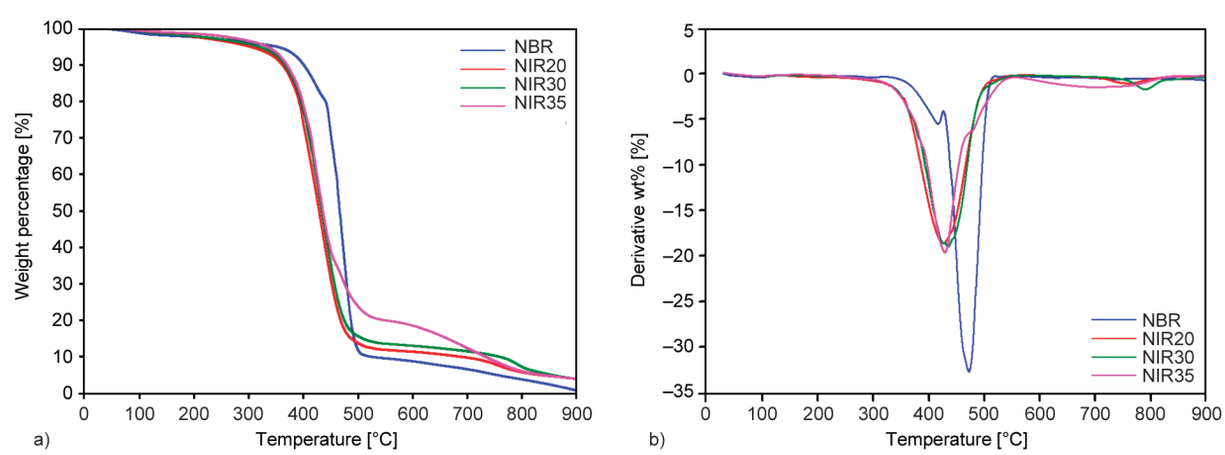

Figure 8. a) TGA curves and b) DTG curves of NIR and NBR.

Table 5. Comparison between decomposition temperature of various NIR and NBR resulted from this work to the recently reported values of NBR in the literature.

Description of sample	ACN content [%]	Decomposition temperatures [°C]			References
		T_{onset}	T_{max}	T_{90}	
NIR20	20*	376.4	426.1	361.3	
NIR30	30*	383.0	434.3	366.2	
NIR35	35*	385.4	428.7	369.9	
NBR	–	430.9	472.0	400.3	
Unfilled NBR	34	–	–	396.6	[35]
+ waste ceramic dust filler		–	–	344.3–381.8	
In situ zirconia filler	34	409.4–414.4	455.4–458.2	–	[36]
Silane-treated silica filler	34	265	445	–	[37]
Unfilled NBR	34	260	418	–	[38]
+ *In situ* silica filler		258–267	437	–	
Nano ZnO filler + disulfochloride benzene crosslinker	40	288	–	350	[39]
Sulfur nd carbon black filler	18	–	449.8	–	[34]
	28	–	453.4	–	
	34	–	456.4	–	
Silica sand nanoparticle filler	40	–	446–456	270–317	[40]
Fumed silica filler		–	450–467	264–286	
Rice bran carbon filler	34	–	461.5–479.9	–	[41]

*based on synthesis formulation

compared to the weak non-polar diene counterpart, resulting in a delay in the overall decomposition of the rubber [34]. Some of the recent reports on decomposition temperatures of NBR are summarized in Table 5, with the value varying from each other due to the differences in the composition of the rubber and its composites. In general, the reported maximum decomposition temperature (T_{max}) of NBR was within a relatively narrow range (418 to 480 °C), while the range of onset decomposition temperature (T_{onset}) and T_{90} varied greatly at 258– 414 °C and 264–396 °C, respectively. Although the thermal stability of NIR is slightly lower compared to the NBR (control) in this study, they are still well within the reported range in the literature and sufficiently high to be used for most elastomeric applications.

3.2.3. Mechanical properties of rubber films

Mechanical property is one important consideration when selecting rubber for a particular application. The mechanical properties of rubber films produced in this work were evaluated according to ASTM D412 for tensile properties and ASTM D624 for tear strength. Stress-strain curves comparison and key mechanical properties are shown in Figure 9 and Table 6, respectively. The *TS* and *EB* follow a similar trend reported in NBR [35, 42], where *TS* increased while *EB* decreased with increasing ACN content. This is attributed to the high strength of dipole interaction between nitrile groups to strengthen the rubber and, at the same time, restrict the rubber chain movement. NIR35 has very low *EB*, exhibiting the behavior of a typical plastic material with necking, as shown in its stress-strain curve. On the other hand, NIR20, NIR30, and NBR films exhibit typical elastomeric

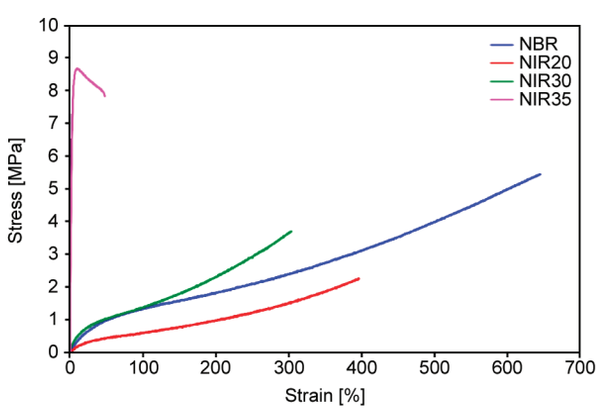

Figure 9. Stress-strain curves of NIR and NBR.

Table 6. Mechanical properties of rubber films.

Sample	*TS* [MPa]	*EB* [%]	*M100* [MPa]	T_s [kN/m]
NIR20	1.61	321	0.585	3.68
NIR30	2.83	253	1.302	7.10
NIR35	8.23	40	n/a	30.53
NBR	6.69	672	1.438	11.03

stress-strain curves. The *TS* and *EB* of NIR20 and NIR30 are, however, lower than that of NBR control films used in this study. This is possibly due to the loss of some unsaturation in the NIR rubber through the formation of crosslinking during the high-temperature emulsion polymerization, which subsequently reduces the effectiveness of the vulcanization process [18]. Although the obtained results for NIR rubber films were lower than the control, the mechanical properties of NIR30 fall well within the reported values for NBR in literature, with *TS* lying between 1.39–9.50 MPa, and *EB* between 227 to 761%, suggesting the viability of NIR to be used for many elastomeric applications [43–46]. *M100* was used to evaluate the stiffness of rubber, and the value increased in the order of NIR20 < NIR30 < NBR. This implies the low rigidity of NIR20 and NIR30 compared to NBR, which could also be attributed to the less effective vulcanization mentioned above. On the other hand, the results of *M100* indicated that *M100* increased as ACN content increased. *M100* for NIR30 is higher than NIR20. The material stiffness enhanced upon ACN content increase, resulting in an increase in modulus. At the same time, it also led to a decrease in *EB* and the *M100* of NIR35 was not measured as the *EB* was <100%. The reported *M100* value of NBR in literature lies between 0.40 to 4.80 MPa [47, 48]. Tear strength, T_s, is defined as the maximum force required to tear the test specimen per unit thickness. The T_s increase with the ACN content in NIR rubber, a trend which was also observed in NBR [42]. Similar to *TS*, the rubber was strengthened by the increased strength of dipole interactions of nitrile groups, improving the resistance of rubber to tearing force. Considering the *TS* values of the rubbers in this work, it was not surprising that NBR has higher T_s than NIR20 and NIR30.

3.2.4. Oil resistance of rubber film

Figure 10a shows the swelling percentage of the rubber film samples in mineral-based engine oil. The oil resistance of the rubber films was evaluated through the percentage of swelling of the films in the hydrocarbon oil. Higher swelling is equivalent to lower oil resistance as the large weight change of the rubber samples indicates higher penetration of oil into the rubber and reduces the entanglement between the rubber chains. Further immersion of rubber samples in oils will cause the formation of pits and cracks through chain scission from thermo-oxidative degradation at elevated temperatures, an environment that is common for oil sealing applications in the automotive industry [49]. These deformations could eventually lead to deterioration in the mechanical properties of the rubber. Hence, an oil resistance test was carried out at room temperature (26 °C) and elevated temperatures of 70 and 100 °C to mimic the usage conditions of oil sealing rubber in the automotive sector. The least oil-resistant synthetic rubber in this work was NBR, with the maximum swelling of 5.46% at 100 °C. For NIR rubber samples, the highest swelling is observed in NIR20, followed by NIR30 and NIR35. Thus, the oil resistance increases in the order from NIR20 < NIR30 < NIR35. The increase in ACN content increases the polarity of NIR rubber, enabling it to repel the penetration of non-polar oil molecules into the rubber matrix through the strong dipolar interaction between nitrile groups. The same phenomenon is also reported in other rubber or blends that exhibit improved oil resistance with increasing polarity, such as in chlorinated NBR [50], NR/dichlorocarbene modified SBR blend [51], and NR/chloroprene blend [52]. The swelling of NBR increases with the testing temperature, which agrees with the reported trend of oil resistance resulting in most rubbers [53, 54]. On the contrary, this trend was not obvious in NIR, possibly due to the minimal swelling of less than 2% in the whole NIR range. The dimension change of NBR rubber at different testing temperatures is shown in Figure 10b. Although the effect and trend from increasing oil temperature on the dimensional changes of the rubber were not that pronounced, possibly because it involves small changes only (<3%), NBR films at 100 °C experienced notably higher dimensional increase than the rest. On the other hand, there was no measurable change in the dimension of all NIR films, and this agrees with the minimal weight changes of the rubber reported in Figure 10a. The NIR and NBR have excellent oil resistance; hence the appearance of NIR20 and NBR did not change noticeably during the oil resistance test as shown in Figures 10c to 10e. NR film was included as a positive control to reflect the superior oil resistance of both synthetic rubbers (NBR and NIR) and validate the experimental protocol. From the comparison in Figures 10c to 10e, it is obvious that NR is the only sample that experienced significant dimensional change post-immersion in mineral oil. Furthermore, the NR sample recorded percentage swelling of 111 and 156% in the

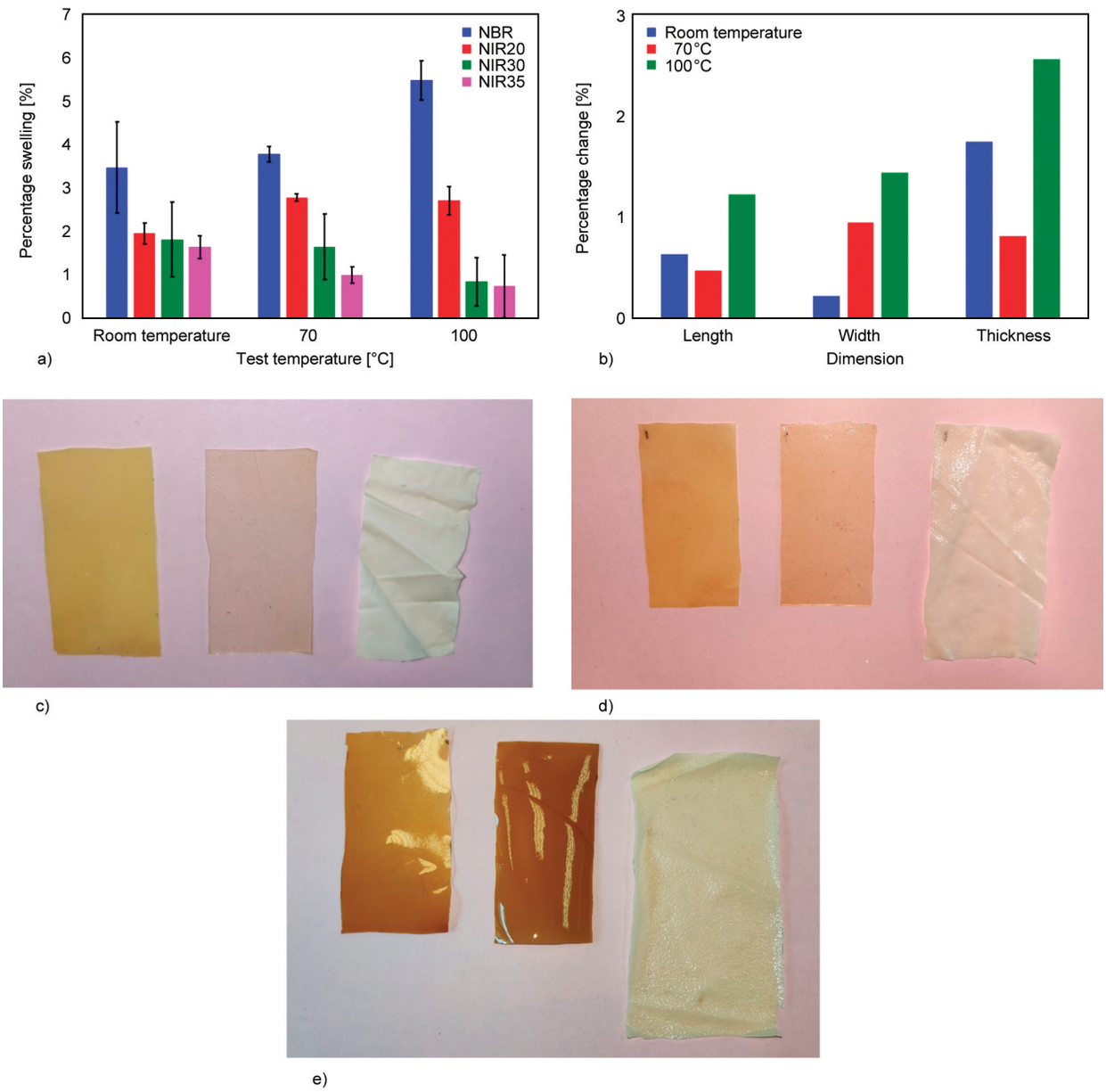

Figure 10. Oil resistance of NIR and NBR films, a) oil swelling, b) dimension change of NBR, and physical appearance of rubber films c) before, and after oil resistance test at d) room temperature and e) 100 °C (from left to right: NIR20, NBR and NR).

oil at room temperature and at 100 °C, respectively, indicating the poor oil resistance of NR compared to NBR and NIR [3]. NIR30 and NIR35 exhibited the best oil resistance with swelling of less than 2% at all testing temperatures. Considering that NIR30 has adequate mechanical properties with superior oil resistance, the rubber may potentially serve as an alternative to NBR in applications that requires good oil resistance, such as joint seals and automotive parts.

4. Conclusions

In this work, a series of poly(isoprene-*co*-acrylonitrile), NIR rubbers with varying ACN content were synthesized via free radical emulsion polymerization. NIR rubber emulsions have good stability, evidenced by the small particle size of the emulsion in the range 90.7 to 122.0 nm, monodisperse (polydispersity indices <0.07), and high magnitude of zeta potential, –63.3 to –50.1 mV. The chemical structure of the synthesized rubber was characterized using FTIR and ^{1}H-NMR, and the results indicated that the polymerization was successful, and the polymerized isoprene in the rubber was predominantly of 1,4-microstructure. The vulcanized NIR films displayed glass transition temperatures from –9.4 to 20.2 °C, of which NIR20 and NIR30 exhibit rubbery behavior

at ambient temperature while NIR35 behaved more towards plastic. The synthesized rubber also recorded good thermal stability, comparable to the control nitrile rubber used in this study. As for mechanical property, ultimate tensile strength and tear strength of the NIR rubbers increased, but elongation at break decreased with ACN content, and although the values are within the reported range in literature, it falls short compared to the NBR control used in this study. On the contrary, the oil resistance of NIR rubber films is superior to the NBR control. In conclusion, NIR has decent thermal stability, mechanical strength, and excellent oil resistance and could serve as an alternative to NBR which had been traditionally used for oil resistance applications. Using isoprene in NIR formulation instead of butadiene gas in NBR formulation could be advantageous in terms of ease of production setup and lower hazard risk.

Acknowledgements

We would like to acknowledge the financial support from the Ministry of Higher Education Malaysia through the Fundamental Research Grant Scheme, FRGS, Project number FRGS/1/2021/STG04/UM/02/4.

References

[1] Gent A. N.: Rubber elasticity: Basic concepts and behavior. in 'The science and technology of rubber' (eds.: Erman B., Mark J. E., Roland C. M.) Elsevier, Waltham, 1–26 (2022). https://doi.org/10.1016/B978-0-12-394584-6.00001-7

[2] Arias M., van Dijk P. J.: What is natural rubber and why are we searching for new sources? Frontiers for Young Minds, **7**, 100 (2019). https://doi.org/10.3389/frym.2019.00100

[3] Simpson R. B.: Rubber basics. Rapra Technology, Shrewsbury (2007).

[4] Boon Z. H., Teo Y. Y., Ang D. T-C.: Recent development of biodegradable synthetic rubbers and bio-based rubbers using sustainable materials from biological sources. RSC Advances, **12**, 34028–34052 (2022). https://doi.org/10.1039/D2RA06602E

[5] Sarkar P., Bhowmick A. K.: Sustainable rubbers and rubber additives. Journal of Applied Polymer Science, **135**, 45701 (2018). https://doi.org/10.1002/app.45701

[6] Fukahori Y.: Use of natural rubber (NR) for vibration isolation and earthquake protection of structures. in 'Chemistry, manufacture and applications of natural rubber' (eds.: Nakao T., Kohjiya S.) Elsevier, Cambridge 371–381 (2014). https://doi.org/10.1533/9780857096913.2.371

[7] Toki S.: The effect of strain-induced crystallization (SIC) on the physical properties of natural rubber (NR). in 'Chemistry, manufacture and applications of natural rubber' (eds.: Nakao T., Kohjiya S.) Elsevier, Cambridge, 135–167 (2014). https://doi.org/10.1533/9780857096913.1.135

[8] Zheng T., Zheng X., Zhan S., Zhou J., Liao S.: Study on the ozone aging mechanism of natural rubber. Polymer Degradation and Stability, **186**, 109514 (2021). https://doi.org/10.1016/j.polymdegradstab.2021.109514

[9] Ali M. F., Akber M. A., Smith C., Aziz A. A.: The dynamics of rubber production in Malaysia: Potential impacts, challenges and proposed interventions. Forest Policy and Economics, **127**, 102449 (2021). https://doi.org/10.1016/j.forpol.2021.102449

[10] Linhares F. N., Corrêa H. L., Khalil C. N., Amorim Moreira Leite M. C., Guimarães Furtado C. R.: Study of the compatibility of nitrile rubber with Brazilian biodiesel. Energy, **49**, 102–106 (2013). https://doi.org/10.1016/j.energy.2012.10.040

[11] Sisanth K. S., Thomas M. G., Abraham J., Thomas S.: General introduction to rubber compounding. in 'Progress in rubber nanocomposites' (eds.: Thomas S., Maria H. J.) Elsevier, Duxford, 1–39 (2017). https://doi.org/10.1016/B978-0-08-100409-8.00001-2

[12] Franta I.: Elastomers and rubber compounding materials: Manufacture, properties and applications. Elsevier, New York (1989).

[13] Jones M. D.: Catalytic transformation of ethanol into 1,3-butadiene. Chemistry Central Journal, 8, 53 (2014). https://doi.org/10.1186/s13065-014-0053-4

[14] Quirk R. P., Pickel D. L.: Polymerization: Elastomer synthesis. in 'The science and technology of rubber' (eds.: Erman B., Mark J. E., Roland C. M.) Elsevier, Waltham, 27–113 (2022). https://doi.org/10.1016/B978-0-12-394584-6.00002-9

[15] Hsieh H. L.: Kinetics of polymerization of butadiene, isoprene, and styrene with alkyllithiums. Part II. Rate of initiation. Journal of Polymer Science Part A: General Papers, **3**, 163–172 (1965). https://doi.org/10.1002/pol.1965.100030118

[16] Weerts P. A., Loos J. L. M., German A. L.: Initiation phenomena in the emulsion polymerization of butadiene and isoprene. Polymer Communications, **29**, 278–279 (1988).

[17] Apolinar Y., Ramos L. F., Saade H., Díaz de León R., López R. G.: Polyisoprene nanoparticles prepared by polymerization in microemulsion. Journal of Nanomaterials, **2010**, 549264 (2010). https://doi.org/10.1155/2010/549264

[18] Cheong I. W., Fellows C. M., Gilbert R. G.: Synthesis and cross-linking of polyisoprene latexes. Polymer, **45**, 769–781 (2004). https://doi.org/10.1016/j.polymer.2003.12.002

[19] Chouytan J., Beraheng S., Kalkornsurapranee E., Fellows C. M., Kaewsakul W.: Synthesis of polyisoprene *via* miniemulsion polymerisation: Effect on thermal behaviour, colloidal properties and stereochemistry. Journal of Rubber Research, **21**, 236–255 (2018). https://doi.org/10.1007/BF03449173

[20] Lima R., de Santi D.: Process for the preparation of nitrile rubbers. European Patent EP 2723776 B1, EU (2013).

[21] Tsuji S., Uchizono Y.: Unsaturated nitrile-conjugated diene copolymer, process for producing same and vulcanizable rubber composition. US5703189A, United States (1997).

[22] Rahn-Chique K., Urbina-Villalba G.: Dependence of emulsion stability on particle size: Relative importance of drop concentration and destabilization rate on the half lifetimes of O/W nanoemulsions. Journal of Dispersion Science and Technology, **38**, 167–179 (2017). https://doi.org/10.1080/01932691.2016.1149715

[23] Corcorran S., Lochhead R. Y., McKay T.: Particle-stabilized emulsions: A brief overview. Cosmetics and Toiletries, **119**, 47–52 (2004).

[24] Danaei M., Dehghankhold M., Ataei S., Hasanzadeh Davarani F., Javanmard R., Dokhani A., Khorasani S., Mozafari M.: Impact of particle size and polydispersity index on the clinical applications of lipidic nanocarrier systems. Pharmaceutics, **10**, 57 (2018). https://doi.org/10.3390/pharmaceutics10020057

[25] Joseph E., Singhvi G.: Multifunctional nanocrystals for cancer therapy: A potential nanocarrier. in 'Nanomaterials for drug delivery and therapy' (eds.: Grumezescu A. M.) Elsevier, Oxford, 91–116 (2019). https://doi.org/10.1016/B978-0-12-816505-8.00007-2

[26] Gumustas M., Sengel-Turk C. T., Gumustas A., Ozkan S. A., Uslu B.: Effect of polymer-based nanoparticles on the assay of antimicrobial drug delivery systems. in 'Multifunctional systems for combined delivery, biosensing and diagnostics' (eds.: Grumezescu A. M.) Elsevier, Oxford, 67–108 (2017). https://doi.org/10.1016/B978-0-323-52725-5.00005-8

[27] Daik R., Bidol S., Abdullah I.: Effect of molecular weight on the droplet size and rheological properties of liquid natural rubber emulsion. Malaysian Polymer Journal, **2**, 29–38 (2007).

[28] He A., Wang G., Zhao W., Jiang X., Yao W., Sun W-H.: High *cis*-1,4 polyisoprene or *cis*-1,4/3,4 binary polyisoprene synthesized using 2-(benzimidazolyl)-6-(1-(arylimino)ethyl)pyridine cobalt(II) dichlorides. Polymer International, **62**, 1758–1766 (2013). https://doi.org/10.1002/pi.4490

[29] Chen D., Shao H., Yao W., Huang B.: Fourier transform infrared spectral analysis of polyisoprene of a different microstructure. International Journal of Polymer Science, **2013**, 937284 (2013). https://doi.org/10.1155/2013/937284

[30] Howard W. H.: The glass temperatures of polyacrylonitrile and acrylonitrile–vinyl acetate copolymers. Journal of Applied Polymer Science, **5**, 303–307 (1961). https://doi.org/10.1002/app.1961.070051509

[31] Kow C., Morton M., Fetters L. J., Hadjichristidis N.: Glass transition behavior of polyisoprene: The influence of molecular weight, terminal hydroxy groups, microstructure, and chain branching. Rubber Chemistry and Technology, **55**, 245–252 (1982). https://doi.org/10.5254/1.3535872

[32] Makhiyanov N., Temnikova E. V.: Glass-transition temperature and microstructure of polybutadienes. Polymer Science Series A, **52**, 1292–1300 (2010). https://doi.org/10.1134/S0965545X10120072

[33] Ambler M. R.: Studies on the nature of multiple glass transitions in low acrylonitrile, butadiene–acrylonitrile rubbers. Journal of Polymer Science: Polymer Chemistry Edition, **11**, 1505–1515 (1973). https://doi.org/10.1002/pol.1973.170110704

[34] Lee Y. S., Ha K.: Effects of acrylonitrile content on thermal characteristics and thermal aging properties of carbon black-filled NBR composite. Journal of Elastomers and Plastics, **53**, 402–416 (2021). https://doi.org/10.1177/0095244320941243

[35] El-Nemr K. F., El-Naggar M. Y., Fathy E. S.: Waste ceramic dust activated by gamma radiation and coupling agents as reinforcement for nitrile rubber. Journal of Vinyl and Additive Technology, **24**, 37–43 (2018). https://doi.org/10.1002/vnl.21515

[36] Ambilkar S. C., Bansod N. D., Kapgate B. P., Das A., Formanek P., Rajkumar K., Das C.: *In situ* zirconia: A superior reinforcing filler for high-performance nitrile rubber composites. ACS Omega, **5**, 7751–7761 (2020). https://doi.org/10.1021/acsomega.9b03495

[37] Kapgate B. P., Das C., Basu D., Das A., Heinrich G.: Rubber composites based on silane-treated stöber silica and nitrile rubber. Journal of Elastomers and Plastics, **47**, 248–261 (2015). https://doi.org/10.1177/0095244313507807

[38] Kapgate B. P., Das C., Basu D., Das A., Heinrich G., Reuter U.: Effect of silane integrated sol-gel derived *in situ* silica on the properties of nitrile rubber. Journal of Applied Polymer Science, **131**, 40531 (2014). https://doi.org/10.1002/app.40531

[39] Mammadov S. M., Khankishiyeva R. F., Ramazanov M. A., Akbarov O. H., Akhundzada H. N.: Influence of gamma irradiation on structure and properties of nitrile-butadien rubber in presence of modified nano metals. American Journal of Polymer Science, **7**, 23–29 (2017). https://doi.org/10.5923/j.ajps.20170702.01

[40] Eyssa H. M., Abulyazied D. E., Abdulrahman M., Youssef H. A.: Mechanical and physical properties of nanosilica/nitrile butadiene rubber composites cured by gamma irradiation. Egyptian Journal of Petroleum, **27**, 383–392 (2018). https://doi.org/10.1016/j.ejpe.2017.06.004

[41] Li M-C., Zhang Y., Cho U. R.: Mechanical, thermal and friction properties of rice bran carbon/nitrile rubber composites: Influence of particle size and loading. Materials and Design, **63**, 565–574 (2014). https://doi.org/10.1016/j.matdes.2014.06.032

[42] Yasin T., Ahmed S., Yoshii F., Makuuchi K.: Effect of acrylonitrile content on physical properties of electron beam irradiated acrylonitrile–butadiene rubber. Reactive and Functional Polymers, **57**, 113–118 (2003). https://doi.org/10.1016/j.reactfunctpolym.2003.08.004

[43] Ruan M., Yang D., Guo W., Zhang L., Li S., Shang Y., Wu Y., Zhang M., Wang H.: Improved dielectric properties, mechanical properties, and thermal conductivity properties of polymer composites via controlling interfacial compatibility with bio-inspired method. Applied Surface Science, **439**, 186–195 (2018). https://doi.org/10.1016/j.apsusc.2017.12.250

[44] Bova T., Tran C. D., Balakshin M. Y., Chen J., Capanema E. A., Naskar A. K.: An approach towards tailoring interfacial structures and properties of multiphase renewable thermoplastics from lignin–nitrile rubber. Green Chemistry, **18**, 5423–5437 (2016). https://doi.org/10.1039/C6GC01067A

[45] Marzec A., Laskowska A., Boiteux G., Zaborski M., Gain O., Serghei A.: The impact of imidazolium ionic liquids on the properties of nitrile rubber composites. European Polymer Journal, **53**, 139–146 (2014). https://doi.org/10.1016/j.eurpolymj.2014.01.035

[46] Szadkowski B., Marzec A., Rybiński P.: Silane treatment as an effective way of improving the reinforcing activity of carbon nanofibers in nitrile rubber composites. Materials, **13**, 3481 (2020). https://doi.org/10.3390/ma13163481

[47] Gill Y. Q., Irfan M. S., Saeed F., Nadeem M., Ehsan H.: Silanized silica compatibilization of NBR/gelatin blends for the production of green rubber products. Journal of Elastomers and Plastics, **51**, 457–472 (2019). https://doi.org/10.1177/0095244318798142

[48] Senthivel K., Manikandan K., Prabu B.: Studies on the mechanical properties of carbon black/halloysite nanotube hybrid fillers in nitrile rubber nanocomposites. Materials Today: Proceedings, **2**, 3627–3637 (2015). https://doi.org/10.1016/j.matpr.2015.07.118

[49] Lou W., Zhang W., Wang H., Jin T., Liu X.: Influence of hydraulic oil on degradation behavior of nitrile rubber O-rings at elevated temperature. Engineering Failure Analysis, **92**, 1–11 (2018). https://doi.org/10.1016/j.engfailanal.2018.05.006

[50] Nihmath A., Ramesan M. T.: Synthesis, characterization, processability, mechanical properties, flame retardant, and oil resistance of chlorinated acrylonitrile butadiene rubber. Polymers for Advanced Technologies, **29**, 2165–2173 (2018). https://doi.org/10.1002/pat.4324

[51] Ramesan M. T., Alex R., Khanh N. V.: Studies on the cure and mechanical properties of blends of natural rubber with dichlorocarbene modified styrene–butadiene rubber and chloroprene rubber. Reactive and Functional Polymers, **62**, 41–50 (2005). https://doi.org/10.1016/j.reactfunctpolym.2004.08.002

[52] Tanrattanakul V., Wattanathai B., Tiangjunya A., Muhamud P.: *In situ* epoxidized natural rubber: Improved oil resistance of natural rubber. Journal of Applied Polymer Science, **90**, 261–269 (2003). https://doi.org/10.1002/app.12706

[53] Zielińska M., Seyger R., Dierkes W. K., Bielinski D., Noordermeer J. W.: Swelling of EPDM rubbers for oil-well applications as influenced by medium composition and temperature. Part I. Literature and theoretical background. Elastomery, **20**, 6–17 (2016).

[54] Lou W., Zhang W., Jin T., Liu X., Dai W.: Synergistic effects of multiple environmental factors on degradation of hydrogenated nitrile rubber seals. Polymers, **10**, 897 (2018). https://doi.org/10.3390/polym10080897

Express Polymer Letters Vol.17, No.10 (2023) 1056–1069
Available online at www.expresspolymlett.com
https://doi.org/10.3144/expresspolymlett.2023.79

Research article

Influence of epoxide content and blend ratios on strength and damping properties of thermoplastic vulcanizates based on epoxidized natural rubber and poly(ether-block-amide) copolymer blends

Azizon Kaesaman[1], *Rawviyanee Romin*[1], *Charoen Nakason*[2*]

[1]Faculty of Science and Technology, Prince of Songkla University, Pattani, Thailand
[2]Faculty of Science and Industrial Technology, Prince of Songkla University, Surat Thani, Thailand

Received19 May 2023; accepted in revised form 11 July 2023

Abstract. Epoxidized natural rubber (ENR) with varying levels of epoxide groups ranging from 10 to 50 mol% was prepared and dynamically phenolic vulcanized by blending it with poly(ether-block-amide) copolymer (PEBA). The results indicate that the thermoplastic vulcanizates (TPVs) of ENR/PEBA blends display a sea-island morphology and enhance a number of properties. Specifically, increasing the epoxide content and PEBA proportion enhances strength properties, including higher Young's modulus (stiffness), toughness, tensile properties, and hardness, along with smaller vulcanized ENR domains dispersed in the PEBA matrix. Moreover, the decrease in tension set values indicates an improvement in the elastic properties. The attributed cause of this is the interaction between the polar groups present in the phenolic-cured ENR domains and the PEBA molecules. As a result, interfacial adhesion between the ENR domains and PEBA interfaces improved, contributing to the observed enhancements in the strength and elastic properties of the TPVs with smaller ENR domains. Furthermore, an increase in the epoxide content was found to be correlated with a decrease in tan δ and tension set, which further supported the observed improvements in strength and elasticity. Additionally, the ENR/PEBA blends showed a single glass transition temperature (T_g), while pure PEBA exhibited two T_gs. The presence of a single T_g in the ENR/PEBA blend is attributed to the overlapping of the T_g of the ENR and PEBA immiscible blend components.

Keywords: *polymer blends and alloys, epoxidized natural rubber (ENR), poly(ether-block-amide) copolymer (PEBA), sea-island morphology, damping property*

1. Introduction

Natural rubber (NR) is a bio-based polymer that is derived from the latex sap of the H*evea Brasiliensis* tree. Due to its renewable resource origin, NR is considered a more eco-friendly alternative to synthetic rubbers made from petroleum-based feedstocks [1, 2]. NR possesses unique mechanical properties such as strength, toughness, elasticity [3], and damping ability [4], making it suitable for various industrial applications. Also, its highly flexible polymer chains enable NR to stretch and recoil easily, providing excellent elasticity and resilience. Therefore, NR finds applications in products such as tires, hoses, balls, cushions, and gloves [5]. In addition to its elasticity, NR also exhibits excellent damping properties or damping factors, which means it can absorb and dissipate mechanical energy in the form of heat during vibration or oscillation. This is because NR has low internal friction due to the interaction between its polymer chains, which allows it to convert mechanical energy into heat [6]. This property makes NR particularly useful

*Corresponding author, e-mail: charoen.nakason@gmail.com
© BME-PT

in applications where vibration damping is important, such as in suspension systems for vehicles or in the construction of buildings and bridges along with shock absorbers (anti-vibration) [7]. While NR has several advantages, it also has some limitations due to its highly unsaturated polymeric backbone. This results in poor resistance to heat, oil, oxygen, and ozone, which can limit its use in certain industrial applications [5]. To overcome these limitations, chemical modifications of the NR molecules have been explored to develop NR derivatives with improved properties and a better balance of characteristics [8]. Epoxidized natural rubber (ENR) is a favored candidate for addressing the limitations of NR because it has a high polarity that provides excellent resistance to oils and non-polar solvents, as well as high impermeability to gases and oils [9]. ENR is also compatible with polar polymers and fillers while retaining the unique mechanical properties of NR, including strength and toughness due to strain-induced crystallization and elasticity, especially its damping properties [10, 11].

Polyether block amide (PEBA) copolymer, also known as Pebax®, is a semi-crystalline polymer with a multiblock structure composed of two types of segments: rigid crystalline polyamide (PA) and amorphous flexible polyether. PEBA is commonly produced through a polycondensation reaction between a carboxylic acid polyamide (such as PA6, P11, or P12) and an alcohol-terminated polyether, which can be either polytetramethylene glycol (PTMG) or polyethylene glycol (PEG) [12, 13]. PEBA exhibits superior mechanical properties, including high flexibility, impact resistance, and fatigue resistance, as well as excellent resistance against a wide range of chemical substances. Compared with common thermoplastic elastomers (TPEs), such as thermoplastic polyolefin elastomer (TPO) and thermoplastic polyurethane (TPU), PEBA exhibits a lower material density and energy loss factor, a higher moisture vapor transfer rate, biocompatibility, and a relatively wide service temperature range, especially at low temperatures [14]. While PEBA already possesses good elasticity and reasonable damping properties, these characteristics can be further improved by blending it with other polymers, such as ENR, that possess outstanding damping properties [15]. PEBA is a versatile polymer that exhibits the ability to blend with various other polymers, such as poly(amide-*co*-poly (propylene glycol)) random copolymer for CO_2/N_2 separation [16] and thermoplastic polyurethane for biomedical applications [17].

In this work, the blending of PEBA and ENR was conducted via dynamic phenolic vulcanization, using various types of ENR with different epoxide groups in their molecules and different ENR proportions in the dynamically cured ENR/PEBA blends. The phenolic-cured system was chosen for its ability to provide the ENR blend with exceptional mechanical and set properties [18]. The main objective was to identify a material that offers a good balance of mechanical properties, along with outstanding damping properties, for use in specific industrial applications. Furthermore, incorporating sustainable green polymers such as natural rubber into engineering materials is an alternative approach to creating materials that are capable of slow biodegradation at the end of their usage life.

2. Experimental

2.1. Materials

Epoxidized natural rubber was synthesized using high ammonia (HA) concentrated latex as the raw material through performic epoxidation. The HA latex was manufactured by Yala Latex Co., Ltd. (Yala, Thailand) and had a dried rubber content (DRC) of approximately 60 wt%, along with an ammonia preservative content of 0.7 wt%. Performic acid was in-situ prepared using formic acid and hydrogen peroxide from Honeywell Specialty Chemicals Seelze GmbH (Seelze, Germany). It was used to react with natural rubber molecules to form ENR with varying levels of epoxide groups. To stabilize the latex during performic epoxidation, a non-ionic surfactant called Teric N30 (Alkylphenol ethoxylate) from Huntsman Corporation Australia Pty Limited (Brooklyn, Australia) was used. Methanol from J.T. Baker Chemicals (Phillipsburg, USA) was utilized to coagulate the ENR latex after performic epoxidation. Thermoplastic vulcanizates (TPVs) were prepared through dynamic vulcanization of Epoxidized Natural Rubber (ENR) and Pebax® 3533, a poly(ether-block-amide) copolymer manufactured by Arkema (Colombes, France). Pebax® 3533 is available in pellet form, comprising 75 wt% poly(tetramethylene oxide) (PTMO) and 25 wt% aliphatic polyamide (PA12), with a melting temperature of approximately 144 °C. Hydroxymethyl (methylol) phenolic resin, HRJ-10518 is a hydroxymethyl (methylol) phenolic resin produced by reacting octylphenol with formaldehyde, and it was used as a vulcanizing agent for

the dynamic vulcanization of ENR/PEBA blends. This resin was manufactured by Akrochem Corporation, (Akron, USA).

2.2. Synthesis of epoxidized natural rubber (ENR)

The synthesis of epoxidized natural rubber (ENR) followed the experimental and characterization methods previously described [19–21]. In brief, 60% DRC HA latex was added into a reactor, and distilled water was added to reduce the DRC to 20%. Next, a non-ionic surfactant, Teric N30, was added to the mixture and then continuously stirred at room temperature for 25 min. Formic acid and hydrogen peroxide were then dropwise added simultaneously into the reactor at a controlled temperature of 50 °C for about 30 min. The reaction mixture was sampled at reaction times of 0, 0:30, 1:00, 1:20, 2:10, 2:40, 4:10, 5:50, and 7:30 h. Excess methanol was added to the latex sample to coagulate it, and then the rubber coagulum was sheeted out and washed thoroughly with clean water until the pH was around 7.0. The rubber sheet was eventually dried in an oven at 60 °C. A proton nuclear magnetic resonance spectroscopy (^{1}H-NMR), Varian Unity Inova 500 MHz Spectrometer (Varian, Griesheim, Germany) was then used to characterize molecular characteristics of the rubber molecules. Finally, the epoxide content was quantified using the Equation (1) [22]:

$$\text{Epoxide contetnt}\,[\text{mol}\%] = \frac{A_{2.70}}{A_{2.70} + A_{5.10}} \cdot 100 \quad (1)$$

where $A_{2.70}$ is the area under the signal at a chemical shift of 2.70 ppm, which indicates resonance of the methine hydrogen of the epoxirane ring, $A_{5.10}$ is the area under the signal at a chemical shift of 5.10 ppm, which indicates olefin hydrogen of cis-1,4-polyisoprene.

2.3. Compounding of ENR by phenolic vulcanization

ENRs with different epoxide group contents of 10, 20, 30, 40, and 50 mol% were firstly dried in a hot air oven at 70 °C for a minimum of 3 h. The dried rubber was then compounded with various chemical ingredients according to the formulation and mixing schedule outlined in Table 1. The compounding was conducted using an internal mixer, a Brabender® Measuring Mixer, model 50EHT 3Z, Brabender GmbH & Co.KG (Duisburg, Germany), at 40 °C, a fill factor of 0.8, and a rotor speed of 60 rpm. At the end of the compounding process, the ENR compound was removed from the mixing chamber and conditioned in a closed container for at least 24 h at room temperature.

Table 1. Compounding formulation and mixing schedule for preparation of ENR compounds.

Chemicals	Quantity [phr]	Mixing time [min]
ENR	100	3
Stearic acid	1	1
ZnO	5	1
Wingstay L	1	1
Phenolic resin	9	3

2.4. Preparation of dynamically cured ENR/PEBA blends

Epoxidized natural rubber (ENR) and poly(ether-block-amide) copolymer at a 50/50 wt% ratio as blended in an internal mixer, a Brabender® Measuring Mixer, model 50EHT 3Z, Brabender GmbH & Co. KG (Duisburg, Germany), at 160 °C. Prior to blending with the ENR compound, the PEBA copolymer was dried at 80 °C for at least 3 h, cooled to room temperature, and conditioned for approximately 3 h. During dynamic vulcanization, the ENR compound was initially incorporated into the mixing chamber at a rotor speed of 60 rpm and mixed for approximately 2 min before adding the PEBA component. The mixture was then continuously mixed for an additional 10 min to achieve a total mixing time of 12 min. Real-time monitoring of mixing torque and temperature was captured during the process. The resulting ENR/PEBA TPVs were subsequently formed into a thin sheet with a thickness of 2 mm using two-roll mills and then compression molded at 160 °C under high pressure for approximately 5 min. The mold was then cooled down by a circulating water system. This work investigated the influence of epoxide contents (10, 20, 30, 40, and 50 mol%) in 50/50 ENR/PEBA TPVs. Additionally, the effect of different blend ratios was studied using ENR-30, with various ENR-30/PEBA ratios of 20/80, 30/70, 40/60, 50/50, 60/40, and 70/30.

2.5. Characterization of ENR/ PEBA TPVs

2.5.1. Mechanical properties

The tensile properties of the TPV specimens were evaluated in terms of tensile strength, modulus, and

elongation at break, following the guidelines of ASTM D412. A Hounsfield universal testing machine, Hounsfield Test Equipment (Surrey, England) was used to conduct the tests at room temperature with a crosshead speed of 500±50 mm/min. The test was performed until the failure of the specimens, and three replicates were tested for each sample. Additionally, the tension set was quantified following the guidelines of ASTM D412. For this, two marks were placed precisely at the ends of the gauge length of the dumbbell-shaped specimens. The initial length between these marks was measured for each sample, and the sample was then extended to a specified elongation at 100% and held at this condition for 10 min. After that, the tension stress was released, and the sample was conditioned at room temperature for another 10 min to allow the relaxation of the TPV specimen. The tension set was then calculated using the Equation (2):

$$\text{Tension set}\,[\%] = \frac{L - L_0}{L_0} \cdot 100 \tag{2}$$

where L_0 is the initial length between the marks before extension and L is the length between the marks after the relaxation of the specimen.

The hardness of the TPV specimen was measured in accordance with ASTM 2240. The test was conducted using a Shore durometer manufactured by Toyo Seiki Seisaku-Sho, Ltd (Tokyo, Japan) and reported in a Shore A unit.

2.5.2. Dynamic properties

The viscoelastic properties of the TPV materials were evaluated using the RheoTech MDpt Moving Die Processability Tester, Tech Pro Inc (Cuyahoga Falls, USA). A frequency sweep test was conducted at 150 °C over a range of 1–25 Hz, using a fixed oscillating strain amplitude of 3%. The dynamic properties, including storage modulus (G'), loss modulus (G''), and tanδ were quantified.

2.5.3. Thermal properties

The TPV specimen was subjected to dynamic mechanical thermal analysis (DMTA) using the DMTA V Dynamic Mechanical Thermal Analyzer, Rheometric Scientific Ltd (Piscataway, USA). The analysis was conducted in dual cantilever mode, with a frequency of 1 Hz, over a temperature range of –100 to 100 °C with a heating rate of 5 °C/min with a normal strain amplitude of 20 µm. This study reports the DMTA thermograms in terms of the relationship between tan δ *versus* the temperature of the TPV specimen.

2.5.4. Morphological characterization

The morphological properties of ENR/PEBA TPVs were examined using a Quanta 400 scanning electron microscope (SEM), FEI Company (Hillsboro, USA), with a magnification of 5000×. The specimen was first cryogenically fractured in liquid nitrogen to create new surfaces and prevent any phase deformation. The PEBA phase was then preferentially extracted by immersing the fractured surface into boiling dimethyl sulfoxide (DMSO) for approximately 20 min. Subsequently, the samples were dried in a vacuum oven at 40 °C for 12 h to eliminate solvent contamination. Prior to imaging with SEM, the dried surfaces were gold-coated. The size of vulcanized rubber domains dispersed in the PEBA matrix was eventually quantified in terms of the number-average (D_n) domain diameters by the Equation (3) [23]:

$$D_n = \frac{\sum N_i D_i}{\sum N_i} \tag{3}$$

where N_i is the number of particles with diameter D_i.

3. Results and discussion

3.1. Synthesis and characterization of epoxidized natural rubber

Epoxidized natural rubber (ENR) was synthesized to gain various levels of epoxide groups (10, 20, 30, 40, and 50 mol%) based on the analyzed results from ^{1}H-NMR spectroscopy, as shown in Figure 1. It can

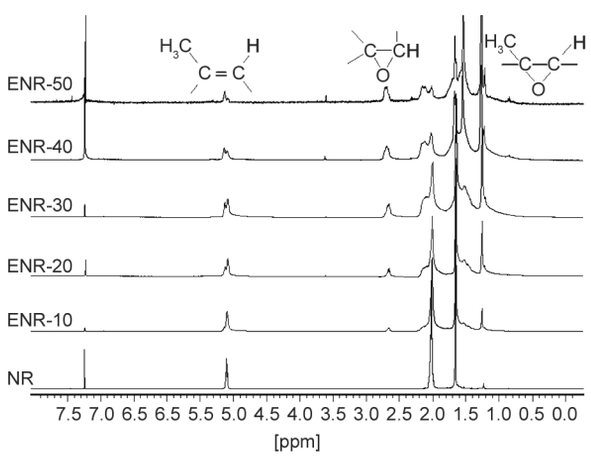

Figure 1. ^{1}H-NMR spectra of epoxidized natural rubber with varying levels of epoxide groups compared with unmodified natural rubber.

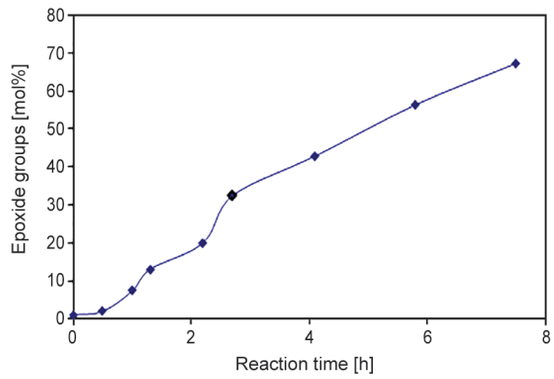

Figure 2. Relationship between reaction time and the level of epoxide groups present in ENR molecules during performic epoxidation.

be seen that the characteristic ^{1}H-NMR signals of ENR were observed at chemical shifts of 2.70, 1.20, and 3.60 ppm (for only ENR-40 and ENR-50), which correspond to the methine hydrogen of epoxide rings, methyl proton of the epoxide rings, and furan or diol proton from the opened epoxirane ring products, respectively [22, 24]. To determine the epoxidation content of the ENR samples, the area ratio of the signals at 2.70 and 5.10 ppm (indicating the olefin hydrogen of cis-1,4-polyisoprene) was calculated using Equation (1). The resulting epoxidation contents were found to be about 10, 20, 30, 40, and 50 mol%, as indicated in Figure 1. The level of epoxidation in natural rubber molecules was influenced by the epoxidation time, as illustrated in Figure 2. The relationship between reaction time and the level of epoxide groups indicates that longer reaction times lead to a higher level of epoxidation. Hence, the reaction time can be used as a parameter to determine the epoxide content in ENR molecules.

3.2. Mixing torque-time and temperature-time profiles for dynamically cured ENR/PEBA blends

Figure 3 displays the mixing torque-time and mixing temperature-time profiles of dynamically cured ENR/PEBA blends with varying levels of epoxide groups in ENR molecules (Figure 3a) and different blend proportions (Figure 3b). Initially, upon adding ENR compounds, there is a rapid decrease in mixing torque and temperature due to the softening of the rubber compound at high temperatures. In contrast, the neat PEBA component (Figure 3b) exhibits an abrupt increase in torque before rapidly decreasing within 1 min of mixing, which is attributed to the stiffness of the PEBA before melting, and the torque subsequently gradually decreases until the end of mixing. However, the torque of ENR/PEBA blends remains nearly constant until the PEBA component is added at a mixing time of around 2 min. This results in the establishment of the initial mixing range, where the mixing torque rises with an increase in epoxide content (Figure 3a) and ENR-30 content in ENR-30/PEBA blends (Figure 3b). After the addition of the PEBA component at 2 min, the mixing torque of the blends abruptly increases while the temperature declines due to the stiffness and starting temperature of PEBA. In Figure 3a, the torque subsequently decreases until the mixing time of approximately 6 min, where a gradually increasing torque is observed until the mixing time of 10 min, where the maximum torque is reached. This is attributed to the dynamic vulcanization of ENR molecules by the phenolic-cured system. The mixing torque at a given mixing time in this range also increases with

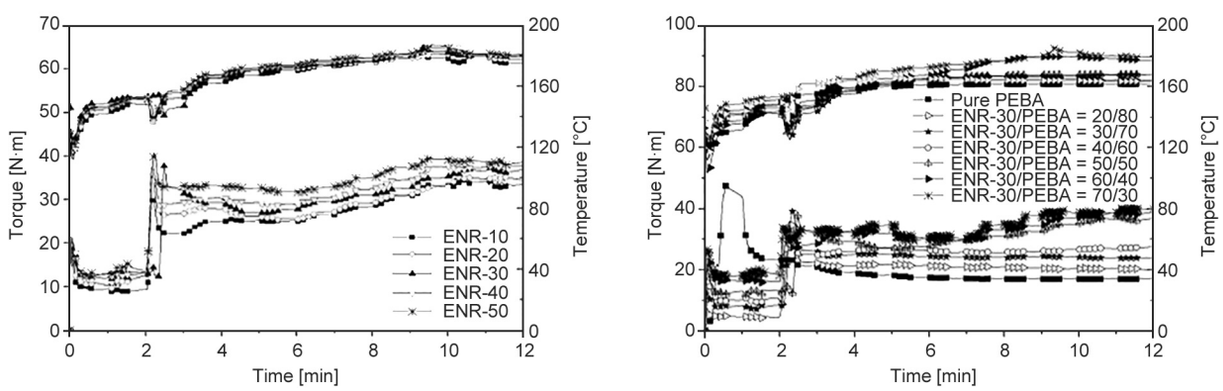

Figure 3. Mixing torque-time and mixing temperature-time profiles for dynamically cured ENR/PEBA blends. a) Blends with various levels of epoxide groups in ENR molecules. b) Blends with various ratios of ENR-30/PEBA compared to pure PEBA.

increasing levels of epoxide groups in ENR molecules. On the other hand, in Figure 3b, after a mixing time of 5 min, only ENR-30/PEBA blends with an ENR content higher than 40 wt% (*i.e.*, ENR-30/PEBA = 50/50, 60/40, and 70/30) exhibit a highly increasing trend of mixing torque. This is due to a higher degree of vulcanization and self-crosslinking of ENR molecules [25, 26], together with a higher chemical interaction between the ENR and PEBA phases. However, ENR-30/PEBA blends with an ENR content lower than 40 wt% exhibit only marginal increases in mixing torque until the end of mixing. The reason for the increased torque is due to the chemical interaction between the vulcanizing ENR and the PEBA phases, as proposed reaction mechanisms described in Figure 4. It is seen that the crosslinking of ENR with phenolic resin takes place first (reaction 1), followed by the capability of the vulcanizing ENR networks to interact with PEBA molecules via chemical interaction through their polar functional groups (reaction 2). Therefore, the polar groups in the phenolic cured ENR domain and PEBA can form intermolecular bonds such as hydrogen bonds, dipole-dipole interactions, and van der Waals forces.

These interactions can lead to a reduction in the size of the ENR domains in the TPV, which can improve the interfacial adhesion between the two phases. After a mixing time of 10 min, the mixing torque remains almost constant until the end of dynamic vulcanization at the final mixing time of 12 min due to the completion of the dynamic vulcanization and chemical reaction between ENR molecules and between the ENR and PEBA phases. It is evident in Figure 3 that the final mixing torque and temperature increased as the epoxide content in ENR molecules (Figure 3a) and the proportion of ENR-30 increased (Figure 3b). This can be attributed to the increased interaction between the polar functional groups in phenolic-cured ENR and the polar groups in the PEBA, as described in reaction (2) in Figure 4. Furthermore, a higher content of epoxide groups and a higher proportion of ENR phase in ENR/PEBA blends resulted in a higher degree of chemical interaction between the two components. This leads to a higher shearing force required to mix the ENR/PEBA blends (at a fixed rotor speed) during dynamic vulcanization and, thus, higher shear heating, which raises the mixing temperature.

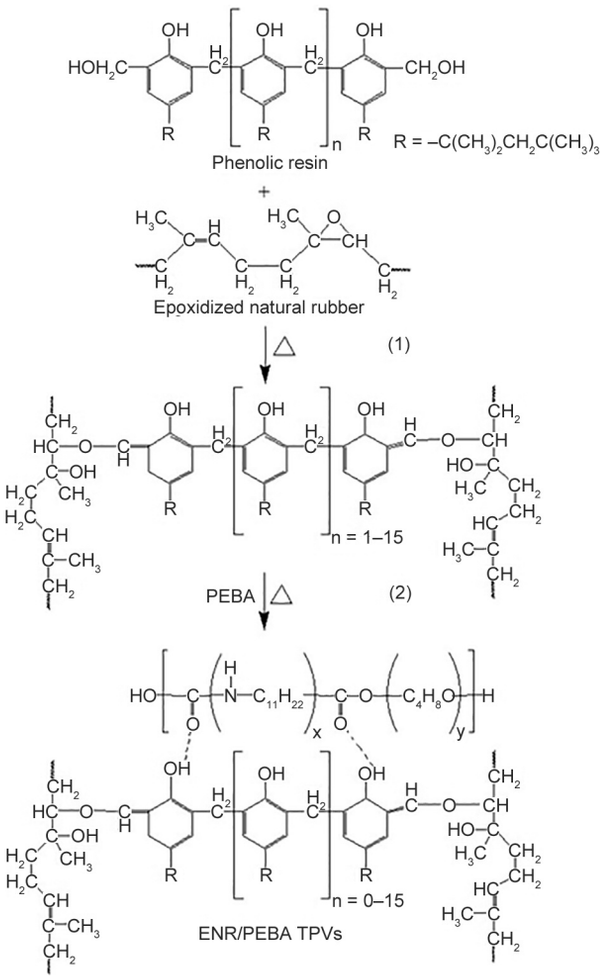

Figure 4. Proposed reaction mechanisms for dynamic vulcanization of ENR/PEBA blends. (1) Reaction of ENR molecules with phenolic curing agent. (2) Chemical interaction between phenolic-cured ENR and PEBA molecules.

3.3. Morphological properties of ENR/PEBA TPVs

Figures 5 and 6 display SEM micrographs of dynamically cured ENR/PEBA blends with different levels of epoxide groups in ENR molecules and different blend ratios of ENR and PEBA, respectively. The micrographs clearly show the sea-island morphology of vulcanized ENR domains dispersed in the continuous PEBA matrix. Notably, the PEBA phase was preferentially dissolved by dimethyl sulfoxide (DMSO) extraction of the fractured surface of the ENR/PEBA TPV specimens. Therefore, only the spherical ENR domains are seen to adhere at the TPV surfaces. In Figure 6, large clusters of rubber domains are clearly visible in TPVs with ENR and PEBA-rich phases (*i.e.*, ENR-30/PEBA = 20/80 and 70/30, respectively). However, In Figure 5, in the blend with a fixed

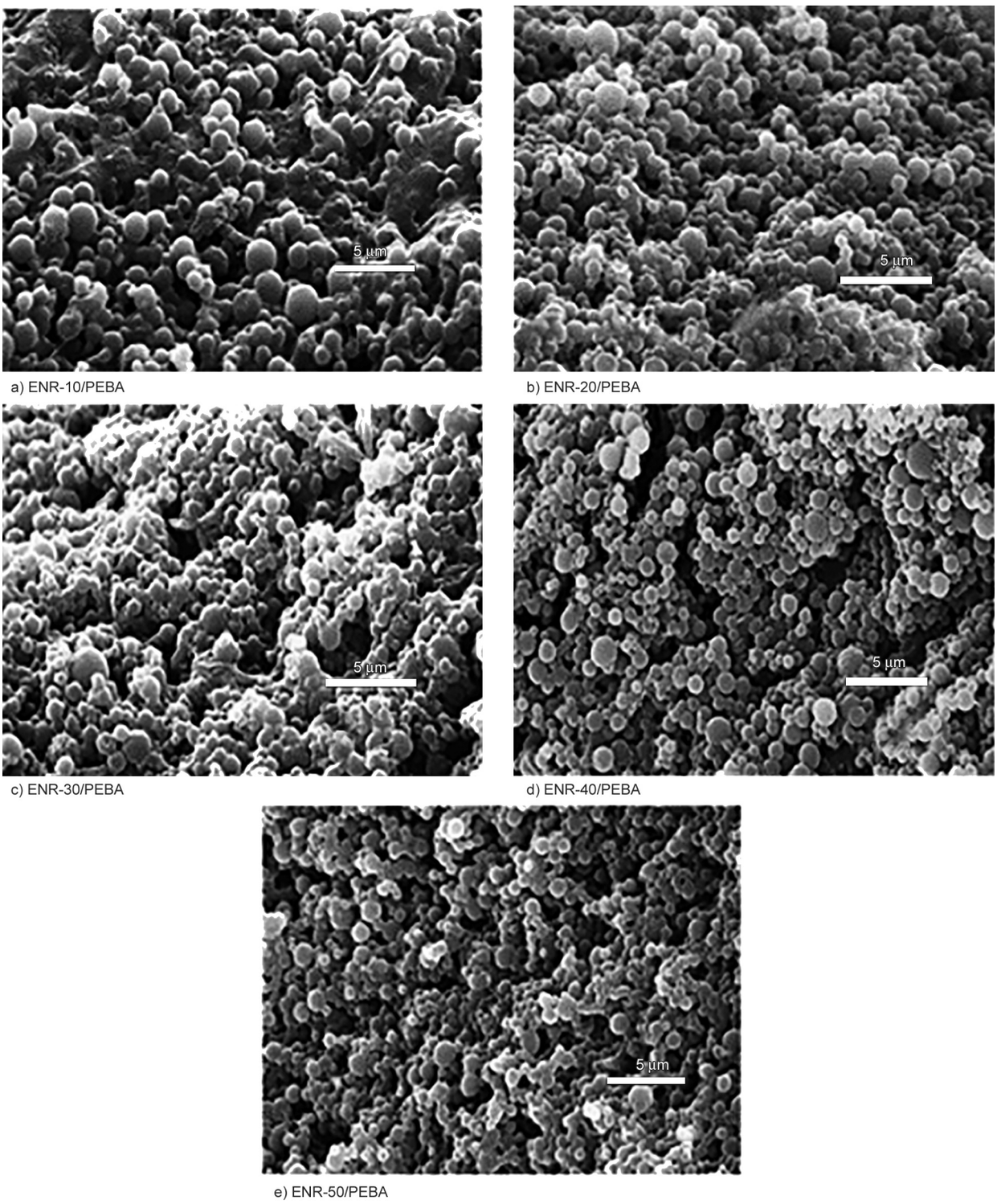

Figure 5. SEM micrographs of dynamically cured 50/50 ENR/PEBA blends with different levels of epoxide groups in ENR molecules. a) ENR-10/PEBA, b) ENR-20/PEBA, c) ENR-30/PEBA, d) ENR-40/PEBA, e) ENR-50/PEBA.

blend ratio ENR/PEBA = 50/50, it can be observed that the size of spherical ENR domains decreased as the level of epoxide groups in the ENR molecules increased. This is also clearly evident from the number-average (D_n) domain diameters of dynamically cured ENR/PEBA blends, which are shown in Table 2. This phenomenon can be attributed to the presence of a phenolic vulcanizing ENR phase (as shown in Figure 4), which results in an increase in shear viscosity during blending. This caused the blend morphology to transform from a co-continuous structure to a dispersed morphology with a severely broken down of the ENR phase into micron-scale vulcanized domains [27]. As a result, an

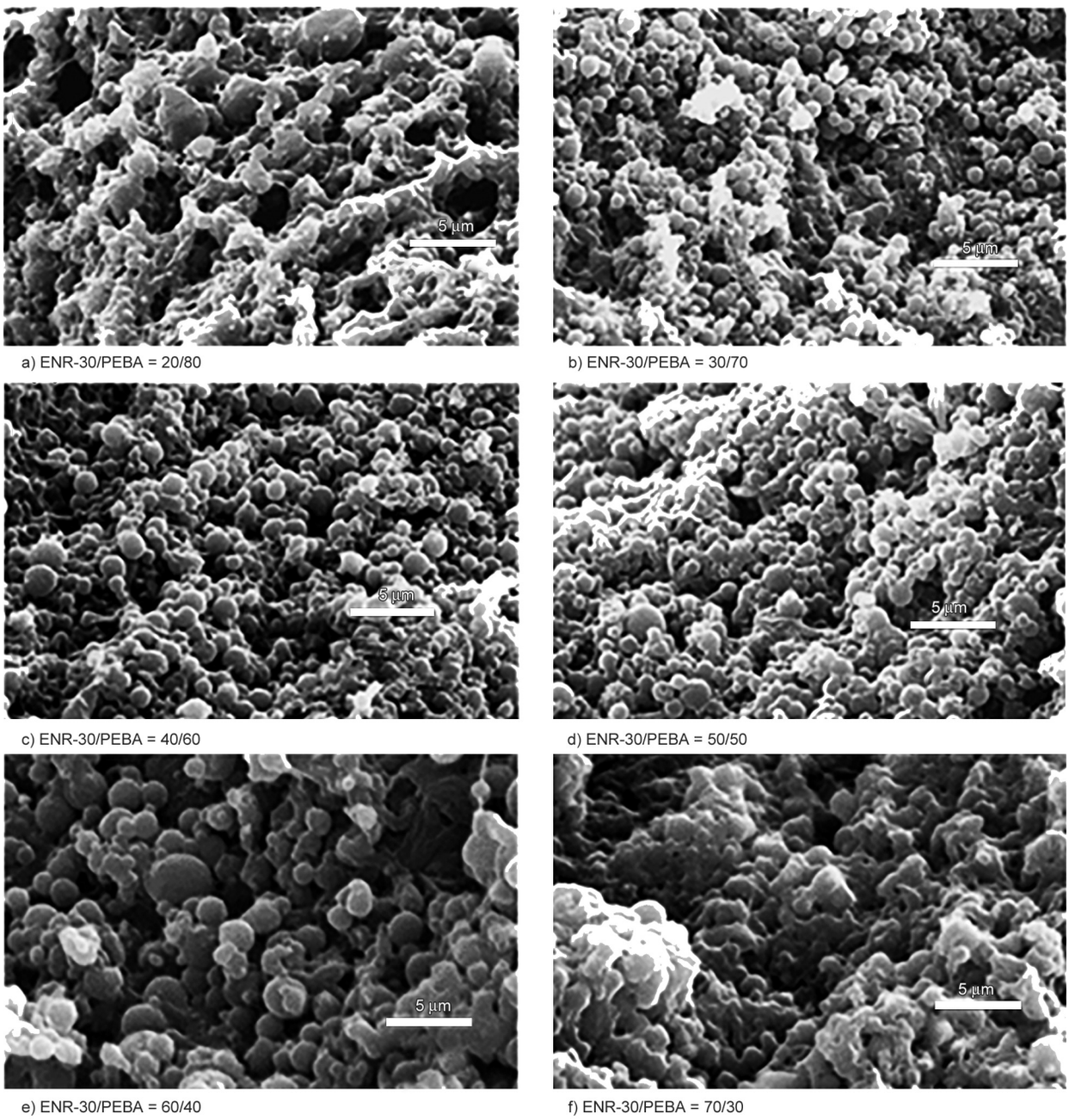

Figure 6. SEM micrographs of dynamically cured ENR/PEBA blends with different ENR-30/PEBA blend ratios. a) ENR-30/PEBA = 20/80, b) ENR-30/PEBA = 30/70, c) ENR-30/PEBA = 40/60, d) ENR-30/PEBA = 50/50, e) ENR-30/PEBA = 60/40, f) ENR-30/PEBA = 70/30.

increase in epoxide content leads to increased mixing torque and shear viscosity during mixing, causing the vulcanizing ENR phase to break down into smaller domains dispersed in the PEBA matrix.

In Figure 6, clear spherical rubber domains are visible in the blends with ENR/PEBA ratios ranging from 30/70 to 60/40 (*i.e.*, Figure 6b to 6e). However, for the blend with one rich phase, large clusters of rubber domains are visible in Figures 6a and 6f. This can be attributed to the influence of the viscosity ratio between the blend components, which leads to a phase inversion from a co-continuous phase to a sea-island morphology via a lamellar mechanism [28]. Therefore, the smaller average size of rubber domains (about 0.7 µm) is seen in ENR-30/PEBA blends with blend ratios ranging from 30/70 to 50/50 (Figure 6b to 6d) and Table 2). However, in the 60/40 ENR/PEBA blend, larger rubber domains at about 1.7 µm are visible (Figure 6e and Table 2), indicating an imbalance of blend proportion (or viscosity ratio)

Table 2. Number-average (D_n) domain diameters of vulcanized ENR domains in dynamically cured ENR/PEBA blends with different levels of epoxide groups in ENR molecules and different ENR-30/PEBA blend ratios.

Epoxide level [mol%]	ENR-30/PEBA blend ratio	Average particle size [μm]
10	–	1.2±0.3
20	–	0.8±0.1
30	–	0.7±0.2
40	–	0.6±0.3
50	–	0.5±0.2
–	20/80	*
–	30/70	0.7 ± 0.2
–	40/60	0.8 ± 0.1
–	50/50	0.7 ± 0.2
–	60/40	1.7 ± 0.1
–	70/30	*

where increased ENR content to 70/30 results in larger and coalescent domains forming large clusters of ENR domains (Figure 6f).

3.4. Mechanical and dynamic properties

Figure 7 illustrates the stress-strain behaviors of dynamically cured ENR/PEBA blends, which exhibit a combination of thermoplastic and elastomeric characteristics. Moreover, in Figure 7a, an increase in the level of epoxide group in ENR molecules leads to an increase in both Young's modulus (determined from the slope of the initial straight line of the stress-strain curve) and toughness (estimated from the area under the curve). This can be attributed to the enhanced interaction between polar functional groups at the interface of the vulcanized ENR domains and PEBA components (Figure 4). However, Figure 7b demonstrates a decrease in Young's modulus as the ENR proportion in the ENR/PEBA blend is increased. This is because Young's modulus is a measure of a material's resistance to deformation under an applied force. It is worth noting that increasing the amount of the elastomeric component (ENR) decreases this resistance or ability to resist deformation.

Table 3 summarizes the mechanical properties of dynamically cured ENR/PEBA blends with varying levels of epoxide groups and blend ratios, including tensile strength, elongation at break, hardness, and tension set. The relationship between stiffness, as determined by Young's modulus, and toughness, as measured by the area under the stress-strain curve, with the tensile strength, elongation at break, and hardness of 50/50 ENR/PEBA TPVs is apparent. Specifically, these properties increase with higher epoxide contents in ENR molecules. The observed phenomenon can be explained by the enhanced interaction between the two phases (Figure 4), which results in a reduction in the size of the spherical vulcanized ENR domains (Figure 5) and an increase in interfacial areas. This, in turn, leads to an improvement in interfacial adhesion between the ENR and PEBA phases. However, as the proportion of ENR-30 in the ENR-30/PEBA blends increases, the tensile strength, elongation at break, and hardness decrease due to the reduced thermoplastic component content, resulting in a reduction in strength and hardness properties. In contrast, it is generally expected that the elongation of the blends will increase as the rubber component content increases. The opposite trend observed in this case suggests the presence of other contributing factors that require further investigation. However, as shown in Table 3, blending PEBA with ENR offers the advantage of reducing hardness and creating a softer material with lower set properties (*i.e.*, high elasticity). Notably, thermoplastic vulcanizates (TPVs) that exhibit low tension sets indicate

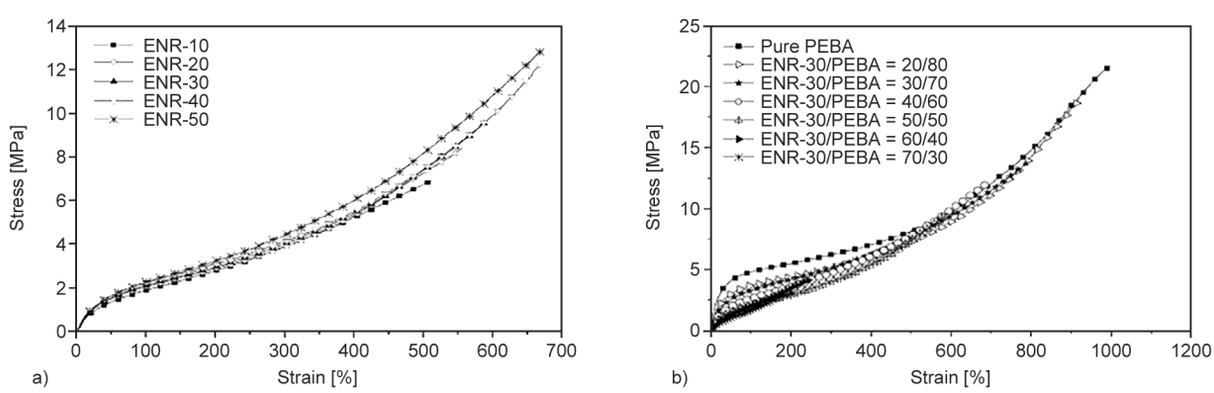

Figure 7. Stress-strain curves for dynamically cured ENR/PEBA blends. a) Blends with different levels of epoxide groups in ENR molecules. b) Blends with different ENR-30/PEBA blend ratios compared to pure PEBA.

Table 3. Mechanical properties of dynamically cured ENR/PEBA blends in terms of tensile strength, elongation at break, hardness, and tension set with different levels of epoxide groups in ENR molecules and ENR-30/PEBA blend ratios.

Epoxide level [mol%]	ENR content [wt%]	Tensile strength [MPa]	Elongation at break [%]	Hardness [Shore A]	Tension set [%]
10	–	6.8±0.2	462±30	55.5±0.5	6.1±0.4
20	–	8.4±0.3	556±25	57.5±0.5	6.0±0.5
30	–	9.6±0.4	593±14	63.5±0.6	5.8±0.3
40	–	12.3±0.3	669±26	64.5±0.5	5.8±0.6
50	–	12.9±0.1	673±04	65.0±0.9	5.6±0.5
–	Pure PEBA	21.6±0.3	999±28	77.0±0.6	13.8±0.3
–	20	19.1±0.1	923±16	75.0±0.5	11.0±0.3
–	30	13.7±0.4	789±10	72.0±0.3	10.3±0.2
–	40	12.3±0.2	685±25	68.0±0.8	9.3±0.1
–	50	9.6±0.4	593±14	64.0±0.6	5.8±0.3
–	60	4.2±0.1	248±14	55.0±0.8	5.0±0.1
–	70	3.1±0.1	203±29	44.0±1.0	4.6±0.3

superior elastic recovery properties, enabling the material to regain its original shape after being stretched. On the other hand, high tension set suggests that the material may undergo permanent deformation and may not recover its original shape. For applications where repeated deformation and recovery cycles are needed, such as in gaskets or seals, a material with a low tension set is preferred as it can maintain its functional properties over time.

As shown in Table 3, the ENR/PEBA TPVs exhibit lower tension set than pure PEBA, and the set decreases as the epoxide and ENR contents increase. This trend is consistent with the behavior of the loss tangent (tan δ), as illustrated in Figure 8. This clearly indicates that the loss tangent decreases as the epoxide group and ENR proportion increase in the TPVs (Figures 8a and 9b, respectively). It is worth noting that the loss tangent (tan δ) is a measure of a material's energy dissipation properties under cyclic deformation. The loss tangent is associated with the material's damping properties and its capacity to absorb and dissipate energy when subjected to cyclic loading. Thus, a lower tan δ value in TPVs indicates that the material has reduced energy dissipation properties and is more elastic in nature. This property can be advantageous in applications where high elasticity is essential, such as in seals, gaskets, and other engineering elastomeric articles.

Figure 9 illustrates the storage modulus of dynamically cured ENR/PEBA blends as a function of oscillating frequency, with varying levels of epoxide groups in ENR molecules and blend ratios. The results show a clear correlation between the storage moduli of TPVs with different epoxide contents (Figure 9a) and blend ratios (Figure 9b), as determined from dynamic testing with a fixed oscillating strain amplitude of 3% at 150 °C, and other mechanical properties such as Young's modulus (Figure 7), tensile strength, and hardness (Table 3). This suggests that the interaction between the ENR and PEBA phases remains. However, it should be noted that under dynamic testing conditions at 150 °C, the properties of both ENR and PEBA may be affected, and the interaction between them could potentially

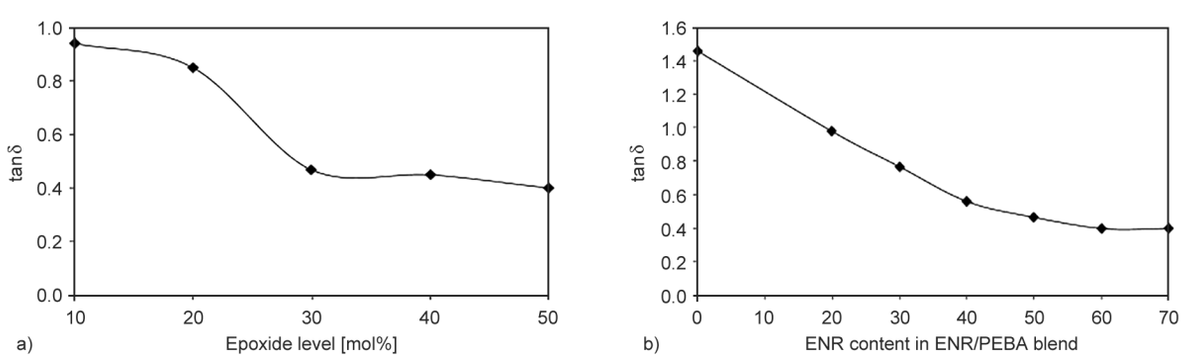

Figure 8. Tan δ *versus* epoxide level (a) and tan δ *versus* epoxide content (proportion) (b) in dynamically cured ENR/PEBA blends at a fixed oscillating frequency of 25 Hz, strain amplitude of 3% at 150 °C.

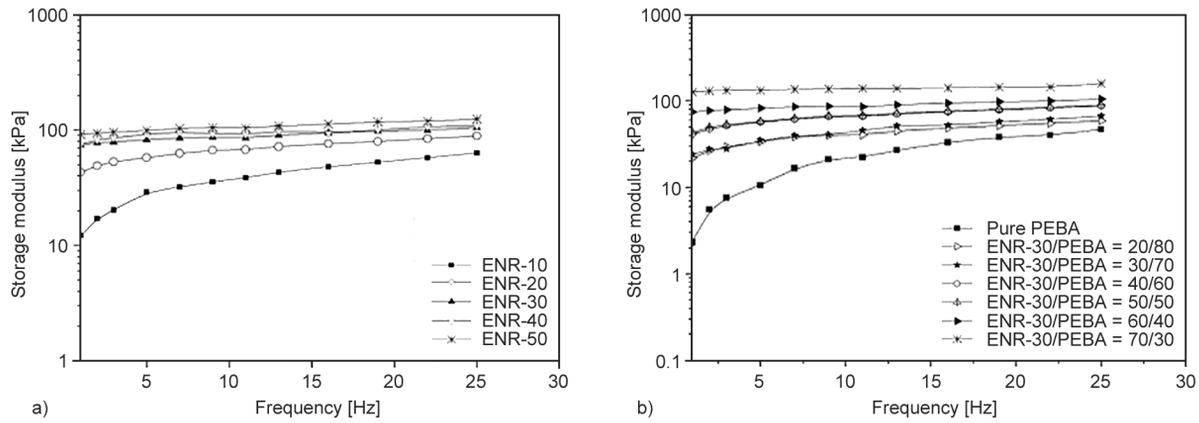

Figure 9. Storage modulus as a function of oscillating frequency for dynamically cured ENR/PEBA blends. a) Blends with different levels of epoxide groups in ENR molecules. b) Blends with different ENR-30/PEBA blend ratios.

change. For instance, the crosslinks in the vulcanized ENR may start to break down, or the PEBA matrix may soften or degrade. Therefore, the specific nature of the interaction between vulcanized ENR domains and the PEBA matrix under dynamic testing conditions at 150 °C would depend on various factors such as the materials' specific chemical composition and properties, the testing conditions, and the type of dynamic testing being performed. In Figure 9b, the storage modulus of pure PEBA displays different trends compared to the properties of the ENR/PEBA TPVs in Figure 7 and Table 3. This can be attributed to the fact that a material can have a high modulus in a stress-strain test performed at room temperature but a lower dynamic storage modulus at elevated temperatures. This variation in behavior can be attributed to the different testing conditions and mechanisms that control the material's response under those conditions. In a stress-strain test, the material is usually deformed at a constant rate and at room temperature. This test is commonly used to assess a material's stiffness or its resistance to deformation, and the modulus value obtained from the test is an indicator of the material's overall rigidity. On the other hand, dynamic testing is utilized to measure the viscoelastic properties of a material under oscillatory deformation at various frequencies. The dynamic storage modulus obtained from this test is an indicator of the material's ability to store elastic energy and resist deformation. At elevated temperatures, the mobility of the polymer chains increases, which can result in a lower storage modulus since the polymer chains are more flexible. Therefore, even if a material has a high modulus at room temperature in a stress-strain test, it may exhibit a lower dynamic storage modulus at 150 °C due to the increased mobility of the polymer chains.

3.5. Thermal properties

Figure 10 displays the results of dynamic mechanical thermal analysis (DMTA). Figure 10a shows the tan δ curves as a function of tested temperature for

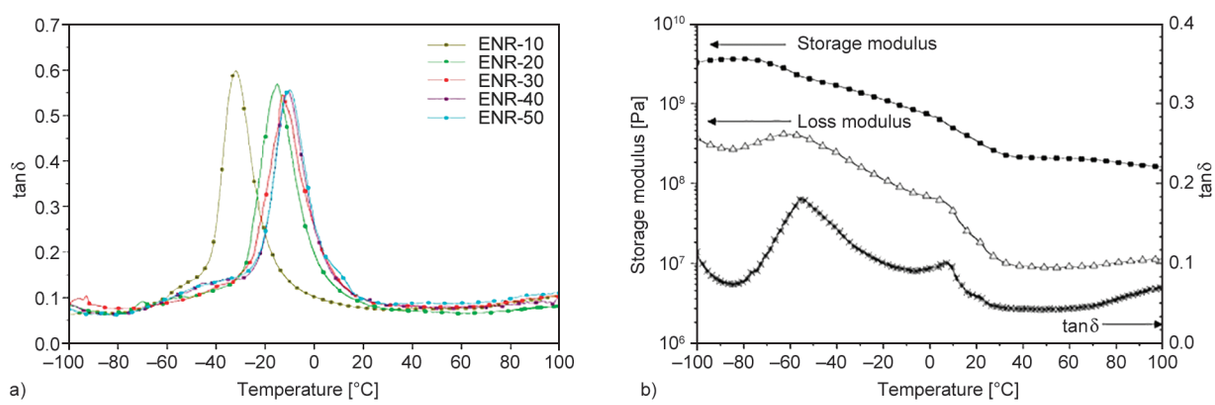

Figure 10. DMTA thermograms of ENR/PEBA TPVs with different levels of epoxide groups in ENR molecules. a) Representative tan δ curves as a function of temperature. b) Thermograms for pure PEBA in terms of storage and loss moduli, along with tan δ curves as a function of tested temperature.

dynamically cured ENR/PEBA blends with varying levels of epoxide groups in ENR molecules. On the other hand, Figure 10b presents the thermograms for pure PEBA, including the storage and loss moduli as well as tan δ curves as a function of tested temperature. It is obvious that the area under the tan δ-temperature curve of ENR/PEBA TPVs decreases as the epoxide content in ENR molecules increases (Figure 10a). This trend suggests that the material's total energy dissipation or loss factor during cyclic deformation is decreasing. It is noted that the loss factor is quantified as the ratio of the energy dissipated to the energy stored in a material during dynamic deformation. This observation is consistent with the decreasing trends of tension set in Table 3 and tan δ in Figure 8, which indicate an increasing trend of viscoelasticity in terms of elasticity for ENR/PEBA blends. These properties can serve as useful indicators of the quality and performance of the material in various applications. Furthermore, Figure 10a and Table 4 show that a single glass transition temperature (T_g) was determined from the peak of the tan δ curve, in contrast to the double T_gs observed in Figure 10b for the pure PEBA component at approximately –55 and 10 °C. The presence of a single T_g in the ENR/PEBA blends may be due to the overlapping of the T_g values of the immiscible blend components. In addition, it was observed that the T_g of the blends increased as the epoxide content in ENR molecules increased, which is contrary to the decreasing trend observed for the set and damping properties (as shown in Table 3 and Figure 8). Increasing the epoxide content in ENR molecules increases the glass transition temperature because it leads to a higher crosslink density, which restricts the mobility of the polymer chains and reduces the free volume in the material, which leads to a higher T_g.

Table 4. Glass transition temperature (T_g) of dynamically cured ENR/ PEBA blends with different levels of epoxide group in ENR.

Epoxide level [mol%]	Glass transition temperature [°C]
10	–30
20	–13
30	–11
40	–10
50	–9

4. Conclusions

Epoxidized natural rubber (ENR) with varying levels of epoxide groups incorporated into its molecular structure was *in-house* synthesized and used to prepare dynamic vulcanizates (DVs) or TPVs based on ENR/PEBA blends, with the primary objective of improving the damping properties of PEBA. The study examined two critical parameters: the effect of the epoxide group content in ENR molecules and the impact of blend ratios in ENR-30/PEBA blends on various TPV properties. The results showed that an increase in the content of epoxide groups in the range of 10 to 50 mol% and the ENR proportion in ENR/PEBA TPVs resulted in improvements in the final mixing torque, tensile strength, hardness, storage modulus, and Young's modulus. This enhancement is attributed to the improved chemical interaction between the polar functional groups in the phenolic vulcanized ENR domains and the PEBA molecules at the interface, which also led to a reduction in the size of the ENR domain dispersed in the PEBA phase of the sea-island morphology. The significant discovery of this study is that combining ENR with PEBA improved the elastic properties, particularly set properties and damping factor. Furthermore, the properties were further enhanced with higher epoxirane ring contents and increased levels of ENR proportion in the blends. Therefore, incorporating sustainable green polymers, such as natural rubber, into engineering materials like PEBA creates a possibility to develop materials with superior elasticity. This approach also offers an alternative way to create materials that can biodegrade slowly at the end of their usage life.

Acknowledgements

The authors would like to express their gratitude for the financial support provided by the Higher Education Research Promotion and National Research University Project of Thailand, Office of the Higher Education Commission (Contract No. SAT540523M)

References

[1] Ren X., Barrera C. S., Tardiff J. L., Gil A., Cornish K.: Liquid guayule natural rubber, a renewable and crosslinkable processing aid in natural and synthetic rubber compounds. Journal of Cleaner Production, **276**, 122933 (2020). https://doi.org/10.1016/j.jclepro.2020.122933

[2] Shah A. L., Hasan F., Shah Z., Kanwal N., Zeb S.: Biodegradation of natural and synthetic rubbers: A review. International Biodeterioration and Biodegradation, **83**, 145–157 (2013). https://doi.org/10.1016/j.ibiod.2013.05.004

[3] Qi X., Wang L., Zhang Y., Jia M., Zhang L., Yue D.: Second natural rubber with self-reinforcing effect based on strain-induced crystallization. Macromolecules, **55**, 2758–2767 (2022). https://doi.org/10.1021/acs.macromol.1c02646

[4] Ghrewati B. E., Kurdi K. E. T., Jena T.: Developing local rubber mixture for seismic base isolation system type high damping rubber bearing. Materials Today: Proceedings, **74**, 881–888 (2023). https://doi.org/10.1016/j.matpr.2022.11.274

[5] Lee S-H., Park S-Y., Chung K-H., Jang K. S.: Phlogopite-reinforced natural rubber (NR)/ethylene-propylene-diene monomer rubber (EPDM) composites with aminosilane compatibilizer. Polymers, **13**, 2318 (2021) https://doi.org/10.3390/polym13142318

[6] Anas K., David S., Babu R. R., Selvakumar M., Chattopadhyay S.: Energy dissipation characteristics of crosslinks in natural rubber: An assessment using low and high-frequency analyzer. Journal of Polymer Engineering, **38**, 723–729 (2018). https://doi.org/10.1515/polyeng-2016-0425

[7] Cho H., Lee S.: Study on the long-term aging-resistance of anti-vibration rubber in the vehicle. in 'SAE 2002 World Congress and Exhibition, Detroit, USA' Technical Paper 2002-01-0725 (2022). https://doi.org/10.4271/2002-01-0725

[8] Phinyocheep P.: Chemical modification of natural rubber (NR) for improved performance. in 'Chemistry, manufacture and applications of natural rubber' (eds.: Kohjiya S., Ikeda Y.) Woodhead, Sawston, 68–118 (2014). https://doi.org/10.1533/9780857096913.1.68

[9] Tanjung F. A., Hassan A., Hasan M.: Use of epoxidized natural rubber as a toughening agent in plastics. Journal of Applied Polymer Science, **132**, 42270 (2015). https://doi.org/10.1002/app.42270

[10] Sarkawi S. S., Aziz A., K. C., Rahim R. A., Ghani R. A., Kamaruddin A. N.: Properties of epoxidized natural rubber tread compound: The hybrid reinforcing effect of silica and silane system. Polymers & Polymer Composites, **24**, 775–782 (2016). https://doi.org/10.1177/096739111602400914

[11] Imbernon L., Pauchet R., Pire M., Albouy P-A., Tencé-Girault S., Norvez S.: Strain-induced crystallization in sustainably crosslinked epoxidized natural rubber. Polymer, **93**, 189–197 (2016). https://doi.org/10.1016/j.polymer.2016.04.023

[12] Peyravi M., Babaluo A. A., Ardestani M. A., Aghjeh M. K. R., Pishghadam S. R., Hadi P.: Study on the synthesis of poly(ether-block-amide) copolymer based on nylon6 and poly(ethylene oxide) with various block lengths. Journal of Applied Polymer Science, **118**, 1211–1218 (2010). https://doi.org/10.1002/app.32358

[13] Clarizia G., Bernardo P.: Polyether block amide as host matrix for nanocomposite membranes applied to different sensitive fields. Membranes, **12**, 1096 (2022). https://doi.org/10.3390/membranes12111096

[14] Xu Z., Wang G., Zhao J., Zhang A., Zhao G.: Super-elastic and structure-tunable poly(ether-block-amide) foams achieved by microcellular foaming. Journal of CO_2 Utilization, 55, 101807 (2022). https://doi.org/10.1016/j.jcou.2021.101807

[15] Metherell C.: Epoxidized natural rubber for controlled damping applications. Progress in Rubber and Plastics Technology, **9**, 237–251 (1993).

[16] Zhu T., Yang X., Zheng Y., He X., Chen F., Luo J.: Preparation of poly(ether-block-amide)/poly(amide-*co*-poly(propylene glycol)) random copolymer blend membranes for CO_2/N_2 separation. Polymer Engineering and Science, **59**, E14–E23 (2019). https://doi.org/10.1002/pen.24828

[17] Xue Y., Tang Z., Qin M., Yu M., Li Z.: Improved toughness of poly(ether-block-amide) *via* melting blending with thermoplastic polyurethane for biomedical applications. Journal of Applied Polymer Science, **136**, 47397 (2019). https://doi.org/10.1002/app.47397

[18] Romin R., Nakason C., Thitithammawong A.: Influence of curing systems on mechanical, dynamic, and morphological properties of dynamically cured epoxidized natural rubber/ copolyamide blends. in 'Advanced Materials Research' (eds.: Nakason C., Thitithammawong A., Wisunthorn S.) Trans Tech Publications, Bäch, Vol. 844, 81–84 (2013). https://doi.org/10.4028/www.scientific.net/amr.844.81

[19] Jarnthong M., Peng Z., Lopattananon N., Nakason C.: The influence of pre-compounding techniques and surface modification of nano-silica on the properties of thermoplastic natural rubber. Express Polymer Letters, **15**, 1135–1147 (2021). https://doi.org/10.3144/expresspolymlett.2021.92

[20] Derouet D., Mulder-Houdayer S., Brosse J-C.: Comparative study of the epoxidation of natural and synthetic rubber latices. Journal of Rubber Research, **9**, 1–20 (2006).

[21] Heping Y., Sidong L., Zheng P.: Preparation and study of epoxidized natural rubber. Journal of Thermal Analysis and Calorimetry, **58**, 293–299 (1999). https://doi.org/10.1023/a:1010199013587

[22] da Silva V. M., Nunes R. C. R., de Sousa A. M. F.: Epoxidized natural rubber and hydrotalcite compounds: Rheological and thermal characterization. Polímeros, **27**, 208–212 (2017). https://doi.org/10.1590/0104-1428.03416

[23] Grestenberger G., Potter G., Grein C.: Polypropylene/ethylene-propylene rubber (PP/EPR) blends for the automotive industry: Basic correlations between EPR-design and shrinkage. Express Polymer Letters, **8**, 282–292 (2014). https://doi.org/10.3144/expresspolymlett.2014.31

[24] Klinklai W., Kawahara S., Mizumo T., Yoshizawa M., Sakdapipanich J. T., Isono Y., Ohno H.: Depolymerization and ionic conductivity of enzymatically deproteinized natural rubber having an epoxy group. European Polymer Journal, **39**, 1707–1712 (2003). https://doi.org/10.1016/S0014-3057(03)00060-0

[25] Zhang P., Huang G., Qu L., Nie Y., Weng G.: Study on the self-crosslinking behavior based on polychloroprene rubber and epoxidized natural rubber. Journal of Applied Polymer Science, **125**, 1084–1090 (2012). https://doi.org/10.1002/app.34508

[26] Manoj N. R., De S. K., De P. P., Peiffer D. G.: Thermally induced crosslinking in the immiscible blend of zinc sulfonated ethylene-propylene-diene monomer rubber and epoxidized natural rubber. Polymer, **34**, 2128–2134 (1993). https://doi.org/10.1016/0032-3861(93)90740-2

[27] Faibunchan P., Pichaiyut S., Kummerlöwe C., Vennemann R., Nakason C.: Green biodegradable thermoplastic natural rubber based on epoxidized natural rubber and poly(butylene succinate) blends: Influence of blend proportions. Journal of Polymer and Environment, **28**, 1050–1067 (2020). https://doi.org/10.1007/s10924-020-01655-5

[28] Machado A. V., Antunes C. F., van Duin M.: Phase inversion of EPDM/PP blends: Effect of viscosity ratio. AIP Conference Proceedings, **1375**, 240–247 (2011). https://doi.org/10.1063/1.3604484

Express Polymer Letters Vol.17, No.10 (2023) 1070–1080
Available online at www.expresspolymlett.com
https://doi.org/10.3144/expresspolymlett.2023.80

Research article

Kinetic studies on the transport behavior of hybrid filler incorporated natural rubber (NR)

Vakkoottil Sivadasan Abhisha[1], *Krishanagegham Sidharathan Sisanth*[2], *Sabu Thomas*[2,3], *Ranimol Stephen*[1*]

[1]Department of Chemistry, St. Joseph's College (Autonomous), Devagiri, Affiliated to University of Calicut, 673008 Calicut, Kerala, India
[2]International and Inter University Centre for Nanoscience and Nanotechnology (IIUCNN), Mahatma Gandhi University, P.D. Hills, 686560 Kottayam, Kerala, India
[3]School of Energy Materials, Mahatma Gandhi University, P.D. Hills, 686560 Kottayam, Kerala, India

Received 5 April 2023; accepted in revised form 11 July 2023

Abstract. Conductive carbon black (CCB), carbon nanotubes (CNT) and its hybrids are introduced into the natural rubber (NR) matrix aiming to explore the effect of filler ratio on the transport properties. Solvent transport of NR is found to decrease for hybrid filler systems as compared to single filler incorporated systems. Kinetic parameters of solvent transport behavior of filled NR systems are analyzed using various kinetic models. Upon the computation of kinetic parameters of transport data, it is found that the Peppas-Sahlin model is in good agreement with experimental observations, which suggests that the transport mechanism is diffusion controlled. Rubber–filler interaction parameters are computed and analyzed from the swelling experiments using Kraus, Cunneen-Russel, and Lorenz-Park equations.

Keywords: *crosslinking, curing, elastomer, filler, natural rubber, vulcanization, carbon black, transport properties*

1. Introduction

The role of polymer composites in the field of membrane technology demands a comprehensive understanding and in-depth knowledge of the transport behavior of solvents in the composite matrix. The transport properties of solvents in polymer composites are related to the distribution and reinforcement of fillers in the matrix. Polymer composites are widely used as food packaging materials owing to their intrinsic qualities such as corrosion resistance, lightweight, enhanced mechanical properties, and thermal properties [1]. Polymer composites containing chemically modified fillers empower the production of highly efficient membranes for pervaporation, ultrafiltration, reverse osmosis, and gas separation [2–8].

The solvent uptake of polymer composites depends on the characteristics of fillers, temperature, morphology, type of solvent, free volume, and processing conditions [9]. The transport of solvents in polymers is also affected by crosslink density, free volume, and structure of the polymer. Polymer chain segmental motions have a crucial influence on the processes associated with the diffusion of molecules through the polymer matrix. Variation in polymer composition and structure directly affects the free volume content and distribution, which in turn affects the transport of matter. The transport processes are interdependent with the polymeric structure and segmental motion of polymer chains [10].

Natural rubber (NR) based polymer composites are widely used in the automotive, construction, and electrical industries and for various engineering applications. Modification of the rubber matrix by the addition of various fillers generates interesting changes

*Corresponding author, e-mail: ranistephen@gmail.com
© BME-PT

in the properties of composites, including transport properties. Carbonaceous fillers such as carbon nanotubes (CNT), graphene, carbon black (CB), carbon fibers, *etc.*, are extensively used fillers in NR. Among the carbon nanofillers, graphene and its derivatives can refine the barrier characteristics of elastomer composites. Graphene-loaded fluoroelastomer shows decreased swelling rates in acetone compared to CB-filled fluoroelastomer composite [11]. Similarly hybrid filler combination of graphene with zinc oxide in NR shows the capacity to resist chemical attack. The mol% uptake for hybrid filler composites shows a remarkable decrease of 41.7% for kerosene, 4.4% decrease for diesel, and 50% for polymethylsilane (PMS) and water, respectively, when compared to CB-filled NR as control [12]. CNT is commonly used as reinforcing fillers in NR due to its high strength and stiffness, exceptional electrical conductivity and high thermal conductivity, which can upgrade the properties of NR. The incorporation of a hybrid filler system is effective in restraining solvent penetration through the polymer matrix [13]. CNT/clay hybrid filler system improves the crosslink density of nitrile rubber (NBR)/NR blends [14]. Conductive carbon black (CCB), also known as electrically conductive black, is used as a reinforcement agent in the manufacture of electrical components such as electromagnetic interference (EMI) shielding shielding agents, static dissipative products and antistatic products [15–17].

The present study focuses on the solvent transport properties of single filler (CCB) and hybrid filler (CCB/CNT) reinforced NR composites as a function of filler concentration and its comparison. Experimentally obtained transport data are evaluated using different kinetic models such as first-order kinetics, Higuchi, Korsemayer-Peppas, and Peppas-Sahlin models. Theoretical understanding of the transport phenomena in rubber composites is beneficial in advanced research as well as in the fabrication of composite membranes. Empirical and semi-empirical mathematical models give a theoretical perspective of experimental transport data. This helps to elucidate the transport mechanism of solvents through the rubber matrix. Matrix-filler interactions are obtained from swelling studies and are evaluated using Kraus, Cunnen-Russel and Lorenz-Park plots. The combination of exploring a hybrid filler system, investigating the effects of filler ratio, applying kinetic modeling, and analyzing rubber-filler interactions contributes to the novelty and importance of the present study. The research gap in the reported work lies in the specific investigation of the synergistic effect of hybrid filler (CCB/CNT) on the transport properties of NR and its theoretical comparison as a function of filler concentration. This aspect has not been extensively studied before, and understanding the transport behavior in these composite systems is crucial for various applications in membrane technology.

2. Experimental

2.1. Materials

Natural rubber (NR) of grade ISNR 20 was purchased from the Rubber Research Institute of India (RRII), Kottayam, Kerala. All the compounding ingredients used were of commercial grade. Conductive carbon black (CCB) was provided by Continental Carbon India Limited (CCIL), Uttar Pradesh, India. The iodine number of CCB is 240±10 mg/g; Brunauer–Emmett–Teller surface area (BET) surface area is 260±10 m^2/g; ash content <0.60 wt% and density is 320±20 kg/m^3. Multiwall Carbon nanotubes (CNT) with ~99% purity were purchased from Adnano Technologies, India. CNT has a high aspect ratio; its diameter is ~5–15 nm, length ~10 μm, surface area ~260 m^2/g, and bulk density of 0.14 g/cm^3. Toluene obtained from Thermo Fisher Scientific Inc. (USA) (molecular weight: 92.14 g/mol, density: 0.866 g/cm^3 and solubility parameter 18.3 $MPa^{1/2}$) was employed for the diffusion studies of rubber composites.

2.2. Preparation of rubber composites

NR/CCB and NR/CCB/CNT composites were prepared by mixing NR and fillers in a Brabender plastograph for 8 min at 100 °C and 60 rpm. Amount of CCB is varied from 5 to 20 phr in NR/CCB composites and all NR/CCB/CNT composites contains 20 phr CCB. The amount of CNT is varied from 0.5 to 5 phr. Curatives were added in an open two-roll mill at room temperature for a total mixing time of 15 min. Preparation method of NR/CCB composites is reported in our previous work [18]. All the prepared NR composites contain 5 g – zinc oxide, 3 g – stearic acid, 1.3 g – *N*-cyclohexyl-2-benzothiazolesulfenamide (CBS), 0.1 g – 2-mercaptobenzothiazole (MBT), and 2.8 g sulfur corresponding to 100 phr NR. The samples were moulded in an electrically heated hydraulic press at 150 °C under a pressure of about 120 bar to the optimum cure time determined

from Moving Die Rheometer ASTM D5289. The NR/CCB samples are coded as NBx and NR/CCB/CNT samples are coded as NBxCy where 'N' represents natural rubber, 'B' represents conductive carbon black (CCB), 'x' represents the quantity of CCB [phr], 'C' represents carbon nanotubes (CNT), and 'y' represents the quantity of CNT [phr].

2.3. Characterization methods

2.3.1. Transport studies

The transport behavior of samples in toluene was studied at room temperature. Circular-shaped samples were immersed in 20 ml toluene and taken in closed diffusion bottles. The weight and thickness of the samples before immersing in a solvent were measured and recorded. The weight of the samples was taken in specific intervals until equilibrium swelling was reached. Each weighing was completed within 30 s to minimize the error due to the evaporation of solvent during weighing. The solvent uptake Q_t [%] of the samples was computed using the Equation (1) [19]:

$$Q_t = \frac{\frac{m_t - m_0}{M_S}}{m_0} \cdot 100 \quad (1)$$

where m_t is the mass of the sample at the time t of immersion and m_0 is the mass of the sample before immersion in the solvent. M_S is the molecular mass of solvent. Here, the molecular mass of toluene is 92.14 g/mol.

2.3.2. High-resolution transmission electron microscopy (HRTEM)

The distribution of CCB in the NR was analyzed through transmission electron microscopy (TEM) using JEOL-JEM 2100, Japan, and operated at 200 kV. The ultra-microtome (Leica, Ultracut UCT) was employed to crosscutting of specimens into ultrathin sections and sited on 300 mesh Cu grids at room temperature.

2.3.3. Swelling studies and crosslink density measurements

The swelling index indicates the swelling resistance of the rubber composites and is obtained using Equation (2) [20],

$$\text{Swelling index} = \frac{W_1 - W_0}{W_0} \cdot 100 \quad (2)$$

where W_1 and W_0 are the weight of the samples after swelling and before swelling in toluene. The swelling behavior of rubber composites can also be analyzed from the swelling coefficient value (α), which is an index of the ability with which the samples swell and is given by the Equation (3) [20]:

$$\alpha = \frac{W_\infty - W_0}{W_0} \cdot \frac{1}{\rho_S} \quad (3)$$

where W_∞ is the weight of the sample at equilibrium swelling in the solvent, W_0 is the weight of the samples before swelling and ρ_S is the density of the solvent used. Here density of toluene used is 0.866 g/cm^3.

The toluene swelling method defined in ASTMD-0471-16a was used to determine the crosslink densities of the samples. Circular-shaped samples are weighed and allowed to swell in toluene until equilibrium. Then after weighing, swelled samples are air-dried for 72 h to measure the de-swollen weight. The apparent crosslink density value is given by $1/Q$ where Q is the swell ratio and is given by Equation (4) [20]:

$$Q = \frac{W_1 - W_0}{W_0} \quad (4)$$

The actual crosslink density of the samples is calculated using the Flory-Rehner equation (Equation (5)) [20–23]:

$$\nu = \frac{\ln(1 - V_{rf}) + V_{rf} + \chi V_{rf}^2}{-2\rho_r V_s V_{rf}^{1/3}} \quad (5)$$

where V_{rf} is the volume fraction of rubber in the solvent-swollen filled sample, χ is the interaction parameter given by Equation (6) [24], ρ_r is the density of the polymer and V_s is the molar volume of solvent. Here molar volume of toluene is 106.3 cm^3/mol:

$$\chi = \beta + \frac{V_s}{RT}(\delta_p - \delta_s)^2 \quad (6)$$

where β is the lattice constant (0.34), R is the universal gas constant, T is the temperature, δ_p and δ_s are the solubility parameters of the polymer and solvent, respectively.

3. Results and discussion

3.1. Kinetic studies of transport properties

Transport properties of NR/CCB and NR-CCB/CNT systems are analyzed in toluene. The effect of filler on the solvent uptake of NR is depicted in Figures 1

and 2. Solvent absorption initially increases rapidly due to the solvent molecules' high concentration gradient in the NR matrix. Then the sorption approaches equilibrium, as indicated by the plateau region of the sorption curve. From Figure 1, it is clear that the solvent uptake of NR/CCB systems decreases significantly as a function of weight percentage of filler. This can be described in terms of the formation of filler-filler and matrix-filler networks, which hinder the diffusion of solvent molecules. The incorporation of hybrid filler further decreases the solvent uptake due to the increase in tortuosity of the diffusing path in the presence of CNT. Similar observations were found in the solvent transport behavior of the halloysite nanotubes-filled NR system [13]. A schematic illustration of the proposed hybrid filler network of CCB and CNT is given in Figure 3.

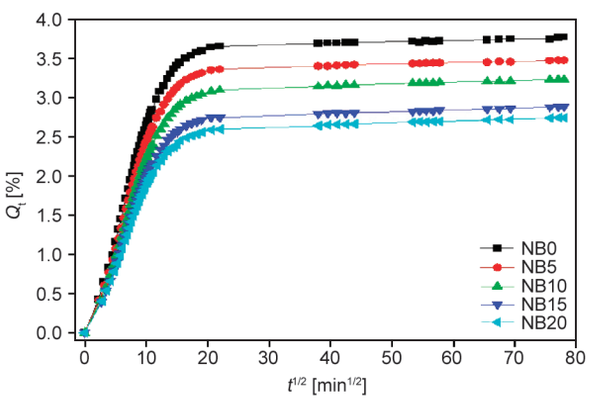

Figure 1. Sorption curves of NR/CCB systems.

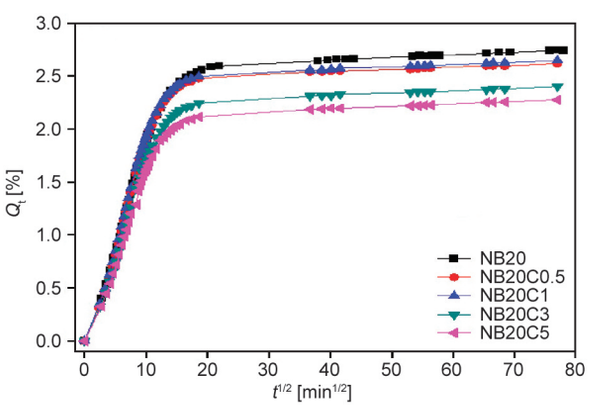

Figure 2. Sorption curves of NR/CCB/CNT systems.

The diffusion coefficient and permeability coefficient values of the CCB and CCB/CNT loaded systems are given in Table 1. The diffusion coefficient is calculated from the equation derived from the second Fickian law (Equation (7)) [25–28]:

$$D = \pi\left(\frac{h\theta}{4Q_\infty}\right)^2 \tag{7}$$

where h is the thickness of the sample, θ is the slope of the initial linear portion of the plot of Q_t [%] against $t^{1/2}$, and Q_∞ the equilibrium absorption. The diffusion coefficient gives the diffusion rate of solvent molecules into the polymer matrix. The diffusion coefficient value decreases linearly with filler loading. Polymer-filler interaction has decreased the availability of free voids, thereby restricting solvent diffusion through the matrix.

The permeability coefficient (P) of toluene in the NR/CCB and NR/CCB/CNT composites is given by Equation (8) [29]:

$$P = D \cdot S \tag{8}$$

where D is the diffusion coefficient and S is the sorption coefficient. The sorption coefficient is calculated from the Equation (9) [24]:

$$S = \frac{m_\infty}{m_0} \tag{9}$$

where m_∞ is the mass of the solvent absorbed at equilibrium and m_0 is the mass of the sample before immersion in the solvent. Sorption involves the initial penetration of solvent molecules and their dispersion across the rubber matrix [30] So, the sorption coefficient depends on the solvent-rubber interaction. The permeability coefficient has both contributions from diffusion and sorption. Decreasing the permeation coefficient with filler loading also suggests improved

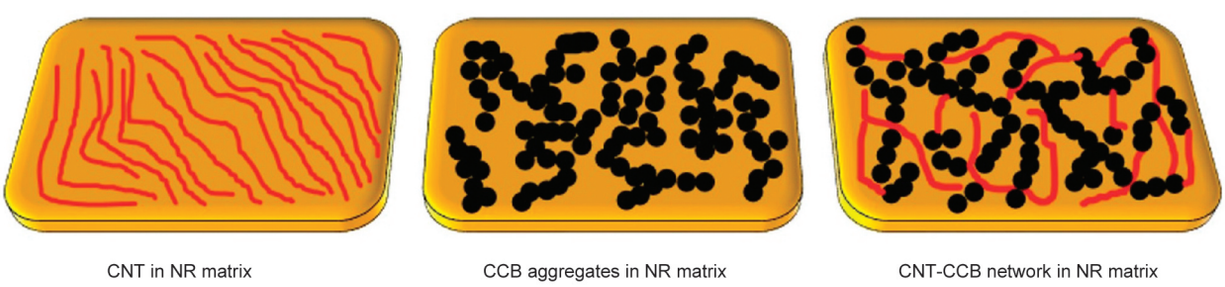

Figure 3. Schematic illustration of hybrid filler network of CCB and CNT.

Table 1. Diffusion coefficient and permeability coefficient.

Sample	$D \cdot 10^{-6}$ [cm^2/s]	$P \cdot 10^{-6}$ [cm^2/s]
NB0	2.14	7.45
NB5	1.96	6.29
NB10	1.74	5.18
NB15	1.45	3.86
NB20	1.22	3.08
NB20C0.5	1.16	2.79
NB20C1	1.10	2.66
NB20C3	1.01	2.23
NB20C5	0.90	1.88

filler-matrix interaction with increasing CCB and hybrid filler content. The permeation coefficient is decreased further upon the introduction of CNT to the single filler system. The interaction of filler and rubber restricts solvent swelling by the formation of crosslinks, which in turn, reduces the segmental mobility of rubber chains. Decreased flexibility of the chains as well as the reduction in the number of voids in the matrix, provides a hindrance to the diffusion of solvent molecules.

The mode of transport is analyzed using Equation (10):

$$\log \frac{Q_t}{Q_\infty} = \log k + n \log t \tag{10}$$

where Q_t is the solvent uptake at time t and Q_∞ is the equilibrium solvent uptake. The constants n and k are determined from the linear portion of the plot Q_t *versus* $t^{1/2}$ (Figures 1 and 2) through power regression analysis. The value of k depends upon the structural characteristics of polymer and polymer-solvent interaction, and n indicates the transport mechanism. The n values are computed (Table 2) and are in between 0.5 and 1 for all composites indicating the non-Fickian mode of transport [20, 27, 31, 32]. For the non-Fickian mode, the chain relaxation is much slower than the solvent penetration. A high degree of restriction produced by the filler particles reduces the segmental mobility of the rubber matrix [33]. Thus, the polymer matrix requires more time for rubber chain rearrangement in response to swelling stress to accommodate solvent molecules. Moreover, incorporated CCB particles diffuse into the cross-linked polymer chains and restrict the chain relaxation.

Table 2. Constant n indicating transport mechanism.

Sample	n
NB0	0.62
NB5	0.62
NB10	0.63
NB15	0.64
NB20	0.61
NB20C0.5	0.62
NB20C1	0.62
NB20C3	0.62
NB20C5	0.62

Theoretical computation is performed on the experimental solvent uptake properties of NR-filler system to attain a better understanding of the mode of transport in composites. We have employed first-order kinetics, Higuchi, Korsemayer-Peppas, and Peppas-Sahlin models to evaluate the transport properties. The first-order kinetic equation is given as (Equation (11) [27]:

$$\log Q_t = \log Q_\infty - \frac{kt}{2.303} \tag{11}$$

where Q_t is the solvent uptake at time t, Q_∞ is the equilibrium solvent uptake, k is the first-order rate constant. The correlation coefficient (R^2) obtained suggests that solvent diffusion in NR/CCB and NR/CCB/CNT composites does not follow first-order kinetics. Higuchi's model proposed that diffusion is based on Fick's law and also it depends on the square root of time. This model is based on the following hypothesis: (a) diffusion is one dimensional, (b) the diffusing particles are much smaller than matrix systems, (c) diffusivity is a constant and (d) matrix swelling and diffusion are constant [34] Higuchi model is simplified as Equation (12):

$$\frac{Q_t}{Q_\infty} = k_h t^{1/2} \tag{12}$$

where k_h is the Higuchi dissolution constant, t is the time and Q_t is the solvent uptake. Higuchi dissolution constant decreased linearly with an increase in filler loadings. Korsemeyer-Peppas [35] model helps to analyze the transport mechanism by the exponential Equation (13):

$$\frac{Q_t}{Q_\infty} = kt^n \tag{13}$$

where k is the kinetic constant, n is the diffusional exponent that indicates the transport mechanism.

Peppas-Sahlin model is based on the theory that the transport mechanism has diffusional and relaxational

contributions, which are additive in nature [36]. Peppas-Sahlin equation is given by Equation (14) [37]:

$$\frac{M_t}{M_\infty} = k_1 t^m + k_2 t^{2m} \quad (14)$$

where first term of the right-hand side is the Fickian contribution, the second term is the case-II relaxational contribution and m is the purely Fickian diffusion exponent for a device of any geometrical shape that exhibits controlled release. Previous works on transport mechanisms of polymeric systems have shown that $k_1 > k_2$ implies a diffusion-controlled mechanism, $k_1 < k_2$ implies a matrix-controlled mechanism, and $k_1 = k_2$ implies a combination of diffusion-controlled and matrix-controlled mechanisms [19]. Constants of various kinetic models are given in Table 3. Peppas-Sahlin model fits well for the solvent diffusion of NR/CCB and NR/CCB/CNT composites. In Peppas-Sahlin theoretical prediction, the k_1 values of all compositions are greater than k_2. The constant k_1 decreases with CB addition up to 15 phr. NB20 has k_1 value higher than NB0. CNT-incorporated composites have almost similar k_1 values. The constant values obtained suggest diffusion controlled transport mechanism in all samples. Fickian diffusion of solvent molecules in the composites is driven by the chemical potential gradient. Theoretical predictions of solvent permeation of NB20 using Higuchi, Korsemayer-Peppas and Peppas-Sahlin are depicted in Figure 4.

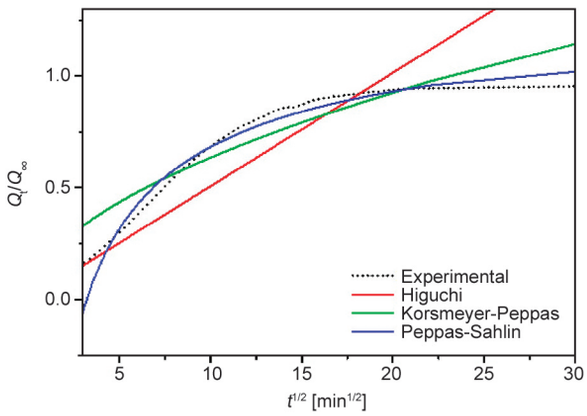

Figure 4. Model fitting of solvent permeation of NB20 using Higuchi, Korsmeyer-Peppas and Peppas-Sahlin equations.

3.2. Theoretical prediction of rubber-filler interaction from swelling studies

The extent of interaction between rubber and CCB and CCB/CNT can be analyzed using Kraus [38], Cunneen and Russel [39] and Lorenz and Park [40] equations. Kraus equation is (Equation (15)):

$$\frac{V_{r0}}{V_{rf}} = 1 - m\frac{f}{1-f} \quad (15)$$

where V_{r0} is the volume fraction of rubber in the solvent-swollen gum vulcanizate, m is the polymer-filler interaction parameter, f is the volume fraction of filler, and V_{rf} is the volume fraction of rubber in the solvent-swollen filled vulcanizate and is given by the Ellis and Welding equation (Equation (16)) [41]:

$$V_{rf} = \frac{\frac{d - f\cdot W}{\rho_p}}{\frac{d - f\cdot W}{\rho_p} + \frac{A_S}{\rho_S}} \quad (16)$$

where d is the non-swollen weight of the sample, f is the weight fraction of filler, W is the initial weight of sample, ρ_p is the density of polymer, ρ_S is the density of solvent and A_S is the amount of solvent absorbed. Plot of V_{r0}/V_{rf} against $f/(1-f)$ gives a straight line whose slope m gives the direct measure of reinforcement by CCB and CCB/CNT. According to Kraus model, reinforcing fillers will have a negative slope [42–44]. V_{r0}/V_{rf} represents the extent of swelling

Table 3. Correlation coefficients and constants of various kinetic models.

Sample		NB0	NB5	NB10	NB15	NB20	NB20C0.5	NB20C1	NB20C3	NB20C5
First order kinetics	k	0.0136	0.0134	0.0132	0.0163	0.0155	0.0156	0.0151	0.0148	0.0146
	R^2	0.8287	0.8390	0.8814	0.8861	0.8907	0.8595	0.8621	0.8766	0.8727
Higuchi model	k_h	0.0519	0.0518	0.0511	0.0512	0.0508	0.0293	0.0293	0.0290	0.0291
	R^2	0.8236	0.8226	0.8255	0.8201	0.8216	0.9595	0.9656	0.9691	0.9523
Korsemayer-Peppas model	k	0.1824	0.1814	0.1759	0.1807	0.1820	0.2189	0.2240	0.1544	0.1546
	n	0.2753	0.2760	0.2790	0.2745	0.2716	0.2379	0.2341	0.2716	0.2716
	R^2	0.9741	0.9878	0.9879	0.9864	0.9714	0.9846	0.9833	0.9863	0.9808
Peppas-Sahlin model	k_1	19.7668	13.3063	12.6867	11.5134	19.8209	19.7565	19.7498	19.7363	19.9999
	k_2	–20.2244	–13.8480	–13.1724	–12.0388	–20.3471	–20.2367	–20.2425	–20.2549	–20.0001
	m	–0.0131	–0.0214	–0.0211	–0.0242	–0.0137	–0.0136	–0.0138	–0.0139	–0.0046
	R^2	0.9821	0.9816	0.9829	0.9847	0.9891	0.9844	0.9868	0.9872	0.9864

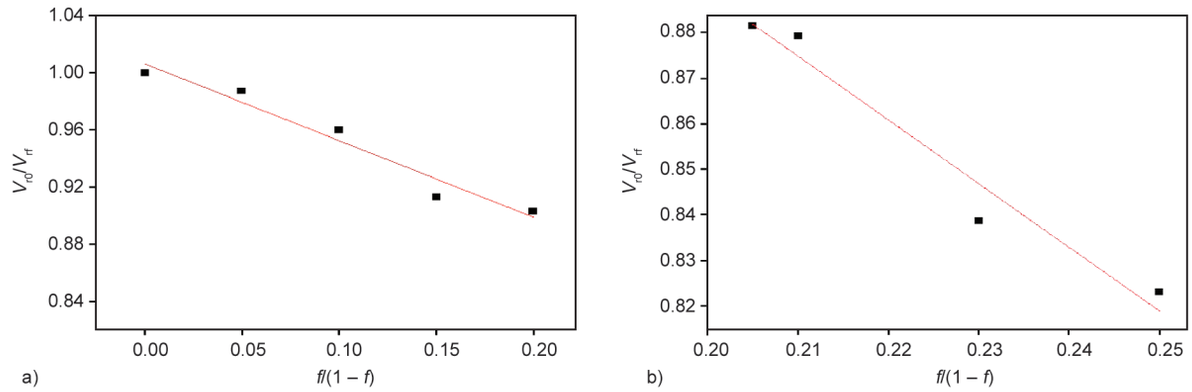

Figure 5. Kraus plots: a) NR/CCB systems b) NR/CCB/CNT systems.

restriction of the rubber matrix owing to the presence of incorporated filler. Kraus plots are given in Figures 5. Here, as the CCB loading increases the solvent uptake of the samples decreases (Figure 5a). Consequently, the V_{rf} values increase, leading to decreases in V_{r0}/V_{rf} values with the filler loading of CCB. Kraus plot gives a negative slope signifying the reinforcement effect of CCB on the rubber matrix. Kraus plot of NR/CCB/CNT systems also gives a negative slope suggesting the synergistic effect of the hybrid filler system on NR matrix. Well-dispersed CCB aggregates and hybrid filler networks of CCB and CNT create stronger interfaces in NR matrix. This leads to the restriction of solvent absorption in the NR.

Cunneen-Russel equation is Equation (17) [22]:

$$\frac{V_{r0}}{V_{rf}} = a\,e^{-z} + b \tag{17}$$

Plot of V_{r0}/V_{rf} against e^{-z}, where z is the weight fraction of filler, gives a straight line with slope a and intercept b. The cunneen-Russel plot of NR/CCB and NR/CCB/CNT composites is given in Figure 6. A positive slope indicates the reinforcement effect of filler on the rubber matrix. Incorporating CCB and hybrid fillers renders a positive slope of the Cunneen-Russel plot, which again supports the fact that the filler effectively interacts with the rubber matrix [22]. Lorenz and Parks equation is Equation (18) [45]:

$$\frac{Q_f}{Q_g} = a\,e^{-z} + b \tag{18}$$

where Q is the amount of solvent imbibed per unit weight, f and g refer to filled and gum rubber vulcanizates, a and b are the constants that depend on the filler activity and z is the weight fraction of filler in the rubber composites. The Q_f/Q_g values indicate the rubber-filler interaction. Decrease in Q_f/Q_g with filler loading signifies a greater extent of filler-matrix interaction. Lorenz and Parks plot of NR/CCB and NR/CCB/CNT composites is given in Figure 7. Plot of Q_f/Q_g against e^{-z} gives a straight line with a positive slope of 1.9267 and y-intercept of –0.9116 for NR/CCB composites. NR/CCB/CNT composites yield a positive slope of 3.6423 and y-intercept of –2.3649. A higher value of constant a and lower

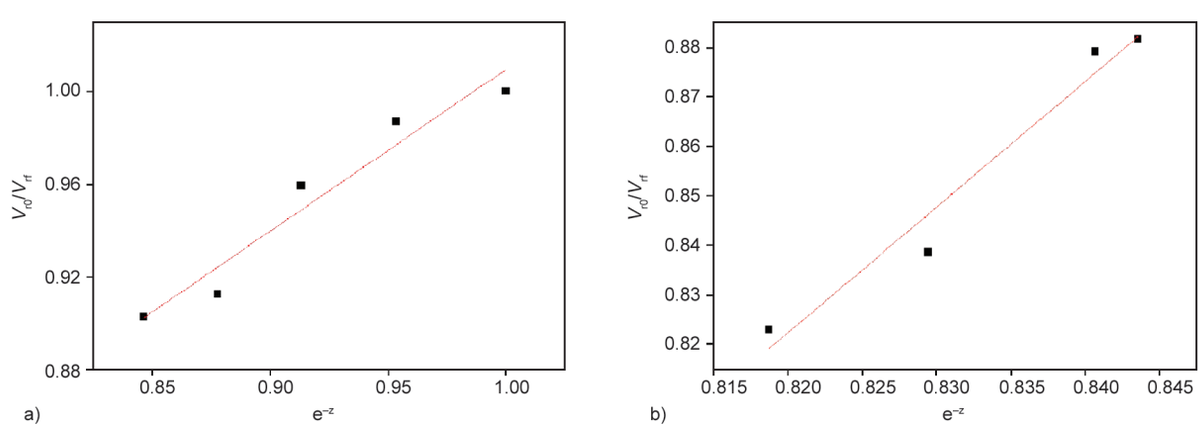

Figure 6. Cunneen-Russel plots; a) NR/CCB systems b) NR/CCB/CNT systems.

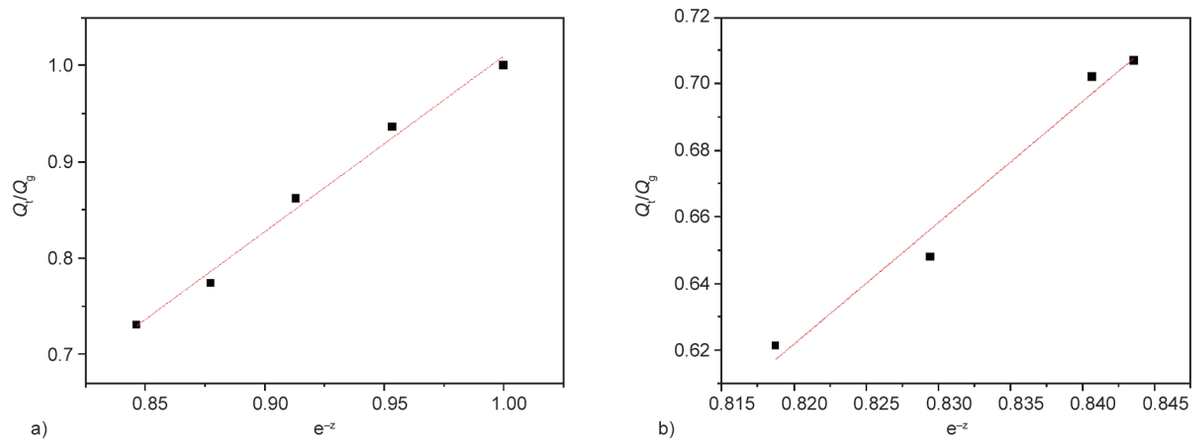

Figure 7. Lorenz-Park plots; a) NR/CCB systems b) NR/CCB/CNT systems.

value of constant b indicates the extent of polymer-filler interaction [45]. The value of constant '*a*' increased for hybrid filler incorporated NR than single filler system, suggesting the enhanced polymer-filler interaction for hybrid system. Higher difference between constant values '*a*' and '*b*' point towards the distinguished filler- rubber interaction.

The morphology of the hybrid filler system is evaluated using TEM. TEM images of the NB20, NB20C3 and NB20C5 is given in Figure 8. CCB aggregates in the matrix are linked together to form a filler network across the matrix in NB20 and some voids can also be present in the matrix (Figure 8a). Extensive filler network formation of CNT and spherical CCB particles are seen when 3 phr of CNT is added to 20 phr CCB (Figure 8b). CNT and CCB particles are uniformly dispersed in the rubber matrix. A similar morphology is observed for NB20C5 also, but voids observed are less when compared to NB20C3 (Figure 8c). Effective filler network formation and uniform dispersion of fillers can be explained in terms of the combination of two processing techniques employed for compounding. Morphological data support the previous results of Kraus, Cunnen-Russel and Lorenz-Park analysis of swelling studies.

3.3. Swelling index and crosslink density

The swelling index and swelling coefficient of NR/CCB and NR/CCB/CNT composites are presented in Table 4. Both swelling index [%] and swelling coefficient decrease linearly with filler loading increase, indicating the restriction of swelling in the filled composites. Hybrid filler network formation restricts the movement of solvent particles through

Table 4. Swelling index [%] and swelling coefficient.

Sample	Swelling index [%]	Swelling coefficient
NB0	339.6	3.92
NB5	317.9	3.67
NB10	292.8	3.38
NB15	262.8	3.03
NB20	248.2	2.86
NB20C0.5	240.1	2.77
NB20C1	238.4	2.75
NB20C3	220.0	2.54
NB20C5	211.0	2.43

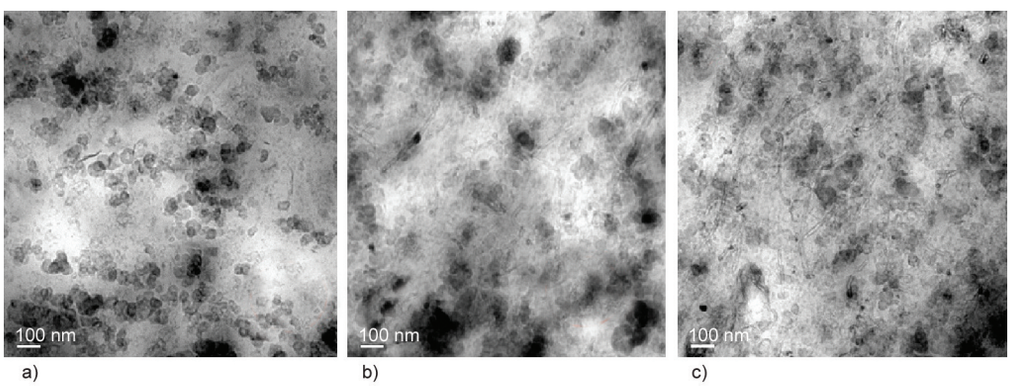

Figure 8. TEM images; a) CCB aggregates in NB20; CNT/CCB network in b) NB20C3 and c) NB20C5.

the polymer matrix. Swelling values gives an insight into the crosslink density of samples. CCB and CNT fillers occupy the free volume of NR matrix resulting in a decrease in the voids in the rubber matrix. The incorporation of fillers offers a tortuous path for diffusing solvent molecules. Thus, the solvent uptake of the filled composites decreases.

The extent of crosslinking can be deducted from the V_{rf} values of the composites. Table 5 shows the V_{rf} values of the NR/CCB and NR/CCB/CNT composites. V_{rf} values are gradually increasing with the filler loading, pointing towards the better interaction of rubber-filler and the formation of crosslinks. Apparent crosslink density values given by $1/Q$ in Table 5 also support the same.

The crosslink density of the NR/CCB and NR/CCB/CNT composites is constantly increasing with filler loading (Table 5). It further supports the reinforcement effect of CCB on NR matrix and the synergistic effect of hybrid filler as well. The values of crosslink density indicate the physical and chemical crosslinks in the system, such as sulfidic linkages, filler-filler and filler-rubber interactions [46].

4. Conclusions

Incorporating hybrid filler consisting of CCB and CNT in NR composites leads to forming a filler network that enhances the transport properties of the composites. The hybrid filler system exhibits increased crosslink density and reduced diffusion coefficient compared to composites containing a single filler. Crosslink density of NR increased significantly upon the addition of 20 phr of CCB. Moreover, the addition of 5 phr CNT along with 20 phr CCB further enhanced the crosslink density, thereby reducing the diffusion coefficient by around 42% when compared to neat NR. Theoretical models were applied to the diffusion data for a better understanding of the transport mechanism. The morphological characterization and theoretical analysis confirm the rubber-filler network formation in NR/hybrid filler systems. Hybrid filler NR composites demonstrate superior transport characteristics compared to composites with single fillers.

Table 5. Volume fraction of rubber (V_{rf}), apparent crosslink density ($1/Q$) and crosslinkdensity (ν) of materials.

Sample	V_{rf}	$1/Q$	ν [g/mol/cm^3]
NB0	0.2119	0.29	$7.28 \cdot 10^{-5}$
NB5	0.2147	0.31	$7.49 \cdot 10^{-5}$
NB10	0.2208	0.34	$7.98 \cdot 10^{-5}$
NB15	0.2322	0.38	$8.91 \cdot 10^{-5}$
NB20	0.2347	0.40	$9.14 \cdot 10^{-5}$
NB20C0.5	0.2404	0.42	$9.64 \cdot 10^{-5}$
NB20C1	0.2410	0.42	$9.70 \cdot 10^{-5}$
NB20C3	0.2527	0.45	$1.08 \cdot 10^{-4}$

Acknowledgements

One of the authors, V. S. Abhisha is thankful to University Grants Commission (UGC), New Delhi for the UGC-JRF fellowship. Also, the first and corresponding authors are thankful to Rashtriya Uchchatar Shiksha Abhiyan (RUSA), New Delhi, India for the financial support.

References

[1] Zhang M., Biesold G. M., Choi W., Yu J., Deng Y., Silvestre C., Lin Z.: Recent advances in polymers and polymer composites for food packaging. Materials Today, **53**, 134–161 (2022). https://doi.org/10.1016/j.mattod.2022.01.022

[2] Swapna V. P., Jose T., George S. C., Thomas S., Stephen R.: Pervaporation separation of an azeotropic mixture of a tetrahydrofuran–water system with nanostructured polyhedral oligomeric silsesquioxane embedded poly (vinyl alcohol). Journal of Applied Polymer Science, **136**, 47060 (2019). https://doi.org/10.1002/app.47060

[3] Swapna V. P., Thomas S. P., Jose T., Moni G., George S. C., Thomas S., Stephen R.: Mechanical properties and pervaporation separation performance of CTAB-modified cage-structured POSS-incorporated PVA membrane. Journal of Materials Science, **54**, 8319–8331 (2019). https://doi.org/10.1007/s10853-019-03479-8

[4] Swapna V. P., Nambissan P. M. G., Thomas S. P., Vayyaprontavida Kaliyathan A., Jose T., George S. C., Thomas S., Stephen R.: Free volume defects and transport properties of mechanically stable polyhedral oligomeric silsesquioxane embedded poly(vinyl alcohol)-poly(ethylene oxide) blend membranes. Polymer International, **68**, 1280–1291 (2019). https://doi.org/10.1002/pi.5815

[5] Swapna V. P., Kaliyathan A. V., Abhisha V. S., Maria H. J., Nambissan P. M. G., Thomas S., Stephen R.: Changes in free volume and gas permeation properties of poly(vinyl alcohol) nanocomposite membranes modified using cage-structured polyhedral oligomeric silsesquioxane. Journal of Applied Polymer Science, **138**, 49953 (2021). https://doi.org/10.1002/app.49953

[6] Stephen R., Joseph K., Oommen Z., Thomas S.: Molecular transport of aromatic solvents through microcomposites of natural rubber (NR), carboxylated styrene butadiene rubber (XSBR) and their blends. Composites Science and Technology, **67**, 1187–1194 (2007). https://doi.org/10.1016/j.compscitech.2006.05.009

[7] Thomas S., George S. C., Jose T.: Polymer nanocomposite membranes for pervaporation. Elsevier, Amsterdam (2020).

[8] Li D., Yan Y., Wang H.: Recent advances in polymer and polymer composite membranes for reverse and forward osmosis processes. Topical Volume on Polymer Hybrid Materials, **61**, 104–155 (2016). https://doi.org/10.1016/j.progpolymsci.2016.03.003

[9] Thomas S., Wilson R., Anil Kumar S., George S. C.: Transport properties of polymeric membranes. Elsevier, Amsterdam (2017).

[10] Rogers C. E., Semancik J. R., Kapur S.: Transport processes in polymers. in 'Structure and properties of polymer films: Based upon the borden award symposium in honor of Richard S. Stein' (eds.: Lenz R. W., Stein R. S.) Springer, Boston, 297–319 (1973).

[11] Liu M., Cataldi P., Young R. J., Papageorgiou D. G., Kinloch I. A.: High-performance fluoroelastomer-graphene nanocomposites for advanced sealing applications. Composites Science and Technology, **202**, 108592 (2021). https://doi.org/10.1016/j.compscitech.2020.108592

[12] Ekebafe L., Nworie E. C., Mahmud H.: Mechanical and sorption indices of ZnO-rGO hybrid filled natural rubber nanocomposites. Journal of Scientific Research and Development, **20**, 209–224 (2021).

[13] Abhisha V. S., Augustine A., Joseph J., Thomas S. P., Stephen R.: Effect of halloysite nanotubes and organically modified bentonite clay hybrid filler system on the properties of natural rubber. Journal of Elastomers and Plastics, **52**, 432–452 (2020). https://doi.org/10.1177/0095244319865573

[14] Thomas S., Abraham J., George S. C., Thomas S.: Role of CNT/clay hybrid on the mechanical, electrical and transport properties of NBR/NR blends. Polymer Bulletin, **77**, 1–16 (2020). https://doi.org/10.1007/s00289-019-02693-3

[15] Cheng H., Cao C., Zhang Q., Wang Y., Liu Y., Huang B., Sun X-L., Guo Y., Xiao L., Chen Q.: Enhancement of electromagnetic interference shielding performance and wear resistance of the UHMWPE/PP blend by constructing a segregated hybrid conductive carbon black–polymer network. ACS Omega, **6**, 15078–15088 (2021). https://doi.org/10.1021/acsomega.1c01240

[16] Jia L. J., Phule A. D., Geng Y., Wen S., Li L., Zhang Z. X.: Microcellular conductive carbon black or graphene/PVDF composite foam with 3D conductive channel: A promising lightweight, heat-insulating, and EMI-shielding material. Macromolecular Materials and Engineering, **306**, 2000759 (2021). https://doi.org/10.1002/mame.202000759

[17] da Silva T. F., Menezes F., Montagna L. S., Lemes A. P., Passador F. R.: Preparation and characterization of antistatic packaging for electronic components based on poly(lactic acid)/carbon black composites. Journal of Applied Polymer Science, **136**, 47273 (2019). https://doi.org/10.1002/app.47273

[18] Abhisha V. S., Sisanth K. S., Parameswaranpillai J., Pulikkalparambil H., Siengchin S., Thomas S., Stephen R.: Comprehensive experimental investigations and theoretical predictions on the physical properties of natural rubber composites. Journal of Applied Polymer Science, **139**, e53197 (2022). https://doi.org/10.1002/app.53197

[19] Zachariah A. K., Kumar Chandra A., Mohamed P. K., Parameswaranpillai J., Thomas S.: Mixed mode morphology in elastomeric blend nanocomposites: Effect on vulcanization, thermal stability and solvent permeability. Polymer Composites, **39**, E1659–E1668 (2018). https://doi.org/10.1002/pc.24624

[20] Kaliyathan A. V., Rane A. V., Jackson S., Thomas S.: Analysis of diffusion characteristics for aromatic solvents through carbon black filled natural rubber/butadiene rubber blends. Polymer Composites, **42**, 375–396 (2021). https://doi.org/10.1002/pc.25832

[21] Flory P. J., Rehner J.: Statistical mechanics of cross-linked polymer networks II. Swelling. Journal of Chemical Physics, **11**, 521–525 (1943). https://doi.org/10.1063/1.1723792

[22] Swapna V. P., Stephen R., Greeshma T., Sharan Dev C., Sreekala M. S.: Mechanical and swelling behavior of green nanocomposites of natural rubber latex and tubular shaped halloysite nano clay. Polymer Composites, **37**, 602–611 (2016). https://doi.org/10.1002/pc.23217

[23] Abraham J., Sidhardhan Sisanth K., Zachariah A. K., Mariya H. J., George S. C., Kalarikkal N., Thomas S.: Transport and solvent sensing characteristics of styrene butadiene rubber nanocomposites containing imidazolium ionic liquid modified carbon nanotubes. Journal of Applied Polymer Science, **137**, 49429 (2020). https://doi.org/10.1002/app.49429

[24] James J., Thomas G. V., Pramoda K. P., Thomas S.: Transport behaviour of aromatic solvents through styrene butadiene rubber/poly[methyl methacrylate] (SBR/PMMMA) interpenetrating polymer network (IPN) membranes. Polymer, **116**, 76–88 (2017). https://doi.org/10.1016/j.polymer.2017.03.063

[25] Stephen R., Thomas S., Raju K. V. S. N., Varghese S., Joseph K., Oommen Z.: Dynamic mechanical and dielectric properties of nanocomposites of natural rubber (NR), carboxylated styrene butadiene rubber (XSBR) latices and their blends. Rubber Chemistry and Technology, **80**, 672–689 (2007). https://doi.org/10.5254/1.3548187

[26] Stephen R., Varghese S., Joseph K., Oommen Z., Thomas S.: Diffusion and transport through nanocomposites of natural rubber (NR), carboxylated styrene butadiene rubber (XSBR) and their blends. Journal of Membrane Science, **282**, 162–170 (2006). https://doi.org/10.1016/j.memsci.2006.05.019

[27] Maria H. J., Lyczko N., Nzihou A., Mathew C., George S. C., Joseph K., Thomas S.: Transport of organic solvents through natural rubber/nitrile rubber/organically modified montmorillonite nanocomposites. Journal of Materials Science, **48**, 5373–5386 (2013). https://doi.org/10.1007/s10853-013-7332-7

[28] Abraham J., Maria H. J., George S. C., Kalarikkal N., Thomas S.: Transport characteristics of organic solvents through carbon nanotube filled styrene butadiene rubber nanocomposites: The influence of rubber-filler interaction, the degree of reinforcement and morphology. Physical Chemistry Chemical Physics, **17**, 11217–11228 (2015). https://doi.org/10.1039/c5cp00719d

[29] Arani A. G., Jafari G. S., Kolahchi R.: Vibration analysis of nanocomposite microplates integrated with sensor and actuator layers using surface SSDPT. Polymer Composites, **39**, 1936–1949 (2016). https://doi.org/10.1002/pc.24150

[30] Danwanichakul P., Jaroenkarn S., Jumpathi P., Dechojarassri D.: Sorption and desorption of toluene, *m*-xylene, *p*-cresol and water by natural rubber chips. Songklanakarin Journal of Science and Technology, **28**, 1071–1082 (2006).

[31] Igwe I. O., Ezeani O. E.: Studies on the transport of aromatic solvents through filled natural rubber. International Journal of Polymer Science, **2012**, 212507 (2012). https://doi.org/10.1155/2012/212507

[32] Thimmaiah S. R., Siddaramaiah: Diffusion and transport behaviors of aliphatic probe molecules through untreated and treated metakaolin filled natural rubber composites. Applied Polymer Composites, **1**, 247 (2013).

[33] Therattil J., Anil Kumar S.: Transport of organic solvents through ionic liquid modified natural rubber/MWCNT composites. International Journal of Scientific and Technology Research, **9**, 3055–3064 (2020).

[34] Sambhudevan S., Shankar B., Appukuttan S., Joseph K.: Evaluation of kinetics and transport mechanism of solvents through natural rubber composites containing organically modified gadolinium oxide. Plastics, Rubber and Composites, **45**, 216–223 (2016). https://doi.org/10.1080/14658011.2016.1165904

[35] Korsmeyer R. W., Gurny R., Doelker E., Buri P., Peppas N. A.: Mechanisms of solute release from porous hydrophilic polymers. International Journal of Pharmaceutics, **15**, 25–35 (1983). https://doi.org/10.1016/0378-5173(83)90064-9

[36] Jose J. P., Thomas S.: XLPE based Al_2O_3–clay binary and ternary hybrid nanocomposites: Self-assembly of nanoscale hybrid fillers, polymer chain confinement and transport characteristics. Physical Chemistry Chemical Physics, **16**, 20190–20201 (2014). https://doi.org/10.1039/C4CP03403A

[37] Peppas N. A., Sahlim J. J.: A simple equation for the description of solute release. III. Coupling of diffusion and relaxation. International Journal of Pharmaceutics, **57**, 169–172 (1989). https://doi.org/10.1016/0378-5173(89)90306-2

[38] Kraus G.: Swelling of filler-reinforced vulcanizates. Journal of Applied Polymer Science, **7**, 861–871 (1963). https://doi.org/10.1002/app.1963.070070306

[39] Cunneen J. I., Russell R. M.: Occurrence and prevention of changes in the chemical structure of natural rubber tire tread vulcanizates during service. Rubber Chemistry and Technology, **43**, 1215–1224 (1970). https://doi.org/10.5254/1.3547319

[40] Lorenz O., Parks C. R.: The crosslinking efficiency of some vulcanizing agents in natural rubber. Journal of Polymer Science, **50**, 299–312 (1961). https://doi.org/10.1002/pol.1961.1205015404

[41] Ellis B., Welding G. N.: Estimation, from swelling, of the structural contribution of chemical reactions to the vulcanization of natural rubber. Part II. Estimation of equilibrium degree of swelling. Rubber Chemistry and Technology, **37**, 571–575 (1964). https://doi.org/10.5254/1.3540349

[42] Stephen R., Alex R., Cherian T., Varghese S., Joseph K., Thomas S.: Rheological behavior of nanocomposites of natural rubber and carboxylated styrene butadiene rubber latices and their blends. Journal of Applied Polymer Science, **101**, 2355–2362 (2006). https://doi.org/10.1002/app.23852

[43] Thomas S., George S., Thomas S.: Rigid amorphous phase: Mechanical and transport properties of nitrile rubber/clay nanocomposites. Progress in Rubber, Plastics and Recycling Technology, **33**, 103–126 (2017). https://doi.org/10.1177/147776061703300204

[44] Gobetti A., Cornacchia G., la Monica M., Zacco A., Depero L. E., Ramorino G.: Assessment of the influence of electric arc furnace slag as a non-conventional filler for nitrile butadiene rubber. Results in Engineering, **17**, 100987 (2023). https://doi.org/10.1016/j.rineng.2023.100987

[45] Zachariah A. K., Chandra A. K., Mohammed P. K., Parameswaranpillai J., Thomas S.: Experiments and modeling of non-linear viscoelastic responses in natural rubber and chlorobutyl rubber nanocomposites. Applied Clay Science, **123**, 1–10 (2016). https://doi.org/10.1016/j.clay.2016.01.004

[46] Fu W., Wang L., Huang J., Liu C., Peng W., Xiao H., Li S.: Mechanical properties and mullins effect in natural rubber reinforced by grafted carbon black. Advances in Polymer Technology, **2019**, 4523696 (2019). https://doi.org/10.1155/2019/4523696